

3.176 43  
p. 75

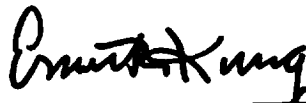
FINAL REPORT TO  
NATIONAL AERONAUTICS AND SPACE ADMINISTRATION  
GODDARD SPACE FLIGHT CENTER  
LABORATORY FOR ATMOSPHERES  
CONTRACT NAS5-30128

Title: Energetics Diagnosis of Numerical Simulation of  
Atmospheric Blocking

Period Covered: September 2, 1987 - December 1, 1990

December 1, 1990

Principal Investigator and Contractor:



Ernest C. Kung  
ECK Research Consulting, Inc.  
1719 Ridgemont  
Columbia, Missouri 65203  
(314) 874-1496

(NACA-CR-193503) ENERGETICS DIAGNOSIS OF  
NUMERICAL SIMULATION OF ATMOSPHERIC BLOCKING  
Final Report, 2 Sep. 1987 - 1 Dec. 1990  
(ECK Research Co.) 75 p

492-11501

CSCL 04A

Unclass

63/46 0317643



## 1. COMPREHENSIVE ASSESSMENT OF RESEARCH RESULTS

During the contract period, a series of systematic comprehensive diagnoses of Goddard Laboratory for Atmospheres (GLA) General Circulation Model (GCM) simulation experiments have been performed in reference to predictability and energetics of the Northern Hemisphere blocking circulation. The simulation experiments performed at GLA in collaboration with GLA scientists are as following:

No.	GCM (latitude x longitude)	Sea Surface Temperature	Initial Data	Simulation Periods
1	4°x5°	Jan. Climatology	GLA	1/1/79-1/31/79
2	4°x5°	Jan. Climatology	GFDL	1/1/79-1/31/79
3	2°x2.5°	Jan. Climatology	GLA	1/1/79-1/31/79
4	2°x2.5°	Jan. Climatology	GFDL	1/1/79-1/31/79
5	4°x5°	Daily updating	GLA	1/1/79-1/31/79
6	2°x2.5°	Daily updating	GLA	1/1/79-1/31/79
7	2°x2.5°	Daily updating	GFDL	1/1/79-1/31/79
8	2°x2.5°	Daily updating	GLA	7/1/79-8/15/79
9	2°x2.5°	July Climatology	GLA	7/1/79-8/15/79

The comprehensive energetics study of Experiments 1-4 indicates that formation of realistic winter blockings should be associated with the barotropic wave-wave energy interaction with the upscale energy input at the zonal wavenumber  $n=1$ . In the 3-dimensional normal mode expansion, the energy transformations from the zonal baroclinic component, via the synoptic-scale baroclinic component, to the planetary-scale barotropic component should also be involved in developing the winter blocking. These in turn are influenced by a number of factors, including model characteristics, boundary forcing, grid resolutions, initial data, and others. These are reported in Kung, Tanaka, and Baker (1989).

The difficulty in simulating a realistic blocking due to inadequate wave-wave interaction is attributed in part to inadequate grid resolution, and to the imbalance of the model and initial data. Among the four simulations analyzed, the simulations by the high resolution GCM produce

realistically strong blockings with compatible energetics as in the observations. In Tanaka, Kung, and Baker (1989), the increase of model resolution is also found to reduce the prediction error in planetary waves  $n=1$  and 2 of the barotropic component and in synoptic waves of the baroclinic component.

In Kung, DaCamara, Baker, Susskind and Park (1990—KDBSP hereafter), three additional numerical simulations, Experiments 5-7, were analyzed to investigate the response of blocking development to the realistic sea surface temperature (SST) distribution, which was continuously updated daily with observed SSTs during the period of simulation. A significant improvement in the blocking formation and forecast skill is apparent in the simulations by the high resolution GCM with daily updating SSTs during the simulation.

As it is clearly illustrated that the updating of SSTs improves the formation of winter blocking, it is particularly noteworthy that following the Pacific blocking, toward the end of January 1979, another strong blocking is formed over the Atlantic Ocean in Exp-6, resembling the observation. This is consistent with the considerable forecast skill in the Atlantic sector in late January. The high skill score later in the month is obtained when the ultralong waves dominate the Northern Hemisphere circulation during the Atlantic blocking. In KDBSP (1989) it is shown that the observed blockings in the Pacific and Atlantic can be described as the composite of wavenumbers 1 and 2. The high pressures embedded in  $n=1$  show a relatively steady pattern, but those in  $n=2$  undergo latitudinal migration, although their longitudinal position does not appreciably change. Superimposition of the migrating  $n=2$  on a steady  $n=1$  creates manifestations observed as blocking, further suggesting the extended forecast skill of blocking development is in fact that of ultralong waves.

The high resolution GCM is able to realistically produce the first (Pacific) blocking episode through the upscale kinetic energy input into the ultralong waves by the wave-wave interaction (Kung, Tanaka, and Baker 1989). Since the development of blocking immediately follows the initialization of the GCM, we may assume the existence of an adequate amount of spatial distribution of baroclinic energy within initial data. For the second (Atlantic) blocking event toward the end of the simulation period, however, the required source of baroclinic energy must be provided by some other

means. This suggests that the realistic ocean surface heating may provide an adequate baroclinic energy source during the simulation. Thus the GCM is able to produce a realistic second blocking even after the effects of initialization are presumably lost.

In the continuing study of long-range simulations of the atmosphere (Kung, DaCamara, Susskind, and Park 1991), the high resolution GLA GCM was integrated with daily updating SSTs for a 45-day period from 1 July to 14 August 1979. With the updating SSTs, the forecast skill is high throughout the simulation period when waves of  $n=4$ , 5 and 6 intensify. The results of this simulation and previous winter simulations with the daily updating SSTs could indicate the upper limit of what would be possible with a coupled ocean-atmosphere model, since the observed SSTs during the atmospheric model integration may imply a correct ocean model prediction of SSTs. The comparison of summer experiments with winter experiments indicate that during the summer the simulation of  $n=4$ , 5 and 6, rather than that of ultralong waves, is critical. The importance of the baroclinic process also increases its importance as synoptic waves respond more directly to the ocean-atmosphere boundary heating without input to the planetary-scale waves. This should be a fundamental difference between the winter and summer seasons in the development of long-range GCM integration.

The progress of research and development has been reported periodically on the semi-annual basis. The details of these are described in Section 4 of this report.

## 2. PUBLICATIONS UNDER THE CONTRACT (Refereed Publications)

- Kung, E.C., H.L. Tanaka, and W.E. Baker, 1989: Energetics examinations of winter blocking simulations in the Northern Hemisphere. Mon. Wea. Rev. 117, 2019-2040.
- Tanaka, H.L., E.C. Kung, and W.E. Baker, 1989: Normal mode energetics and error analysis of GLA GCM simulations with the different horizontal resolutions during a winter month. Beit. Phys. Atmosph., 62, 99-111.
- Kung, E.C., C.C. DaCamara, W.E. Baker, J. Susskind, and C.-K. Park, 1990: Simulations of winter blocking episodes using observed sea surface temperatures. Quart. J. Roy. Meteor. Soc. (In Press).

Kung, E.C., W. Min, J. Susskind, and C.-K. Park, 1991: An analysis of simulated summer blocking episodes. (To be submitted to Quart. J. Roy. Meteor. Soc.).

The following paper is in preparation, and is expected to be submitted for publication under the continued contract which is pending.

Kung, E.C., W. Min, and J. Susskind, 1991: Composite energetics of Asian cold air outbreaks in GLA simulation experiments.

### 3. CONCLUSIONS AND RECOMMENDATIONS

The systematic diagnoses of the series of GLA GCM simulations indicate a considerable predictability of winter and summer blocking phenomena in the Northern Hemisphere if the numerical integrations of GCM are performed under proper given conditions. A high resolution GCM is needed to have adequate wave-wave interaction in case of winter blocking simulations to amplify the planetary waves, particularly that of  $n=1$ . The daily updating of SSTs during the simulation is shown to be critical in producing the second major winter blocking during a one-month simulation period. This may be interpreted to mean that the SST updating provides a necessary updating of the initial data at least for the boundary forcing. This may also be seen as an indication of a possible extension of forecast skill with future coupled ocean-atmosphere GCMs through correct ocean model SST prediction.

The obvious success in a 45-day summer simulation with updating SSTs may well suggest the much longer predictability in GCM integration than we currently assume. As the key to future development of forecast skill is to have proper SST prediction or updating during the simulation, it is also noteworthy that the winter and summer blockings are different in nature, the former being barotropic and the latter baroclinic. This suggests that the winter and summer simulation may be developed separately with proper conditions of simulations for barotropic and baroclinic processes.

Throughout our diagnosis, it is apparent that the blocking phenomena are ideal targets to be attained in the development of long-range forecast. Blockings are quasi-stationary phenomena in the general circulation, and thus well defined synoptically. They possess longer predictability than other transient phenomena. Continued research is recommended to systematically investigate the utilities of SSTs in long-range forecasting both with the GCM

simulation and with the empirical multiple-regression scheme.

In the next phase of study at least three cases of regression forecasting shall be selected for comparison with the GCM simulations, in which the SST dependency of regression forecasting is most apparent. Parallel numerical simulations of these cases shall be conducted using the 2°x2.5° GLA Phoenix GCM, during which SSTs will be updated daily with the observation data. The GCM integration will be extended beyond one month to a season until the forecast skill of ultralong waves significantly deteriorates. The circulation patterns and dynamics-energetics of numerical simulations will be analyzed to relate the predictors and predictands in regression forecast through the evolution of the general circulation. Using the analysis of simulation experiments the possibility of eventual long-range forecasting by coupled ocean-atmosphere models will be studied.

#### 4. TECHNICAL DETAILS OF ACCOMPLISHED RESULTS

Technical details of accomplished results are presented in the form of publication as following: 4.1 and 4.2 copies of reprints, and 4.3 in a prepublication form.

#### 4.1 Energetics examination of winter blocking simulations in the Northern Hemisphere

Ernest C. Kung, H.L.Tanaka and Wayman E.Baker



## Energetics Examination of Winter Blocking Simulations in the Northern Hemisphere

ERNEST C. KUNG AND H. L. TANAKA\*

*Department of Atmospheric Science, University of Missouri—Columbia, Columbia, Missouri*

WAYMAN E. BAKER

*Development Division, National Meteorological Center, NWS/NOAA, Washington, D.C.*

(Manuscript received 16 August 1988, in final form 30 March 1989)

### ABSTRACT

Four numerical simulations of the global atmosphere for January 1979 are analyzed to study the formation of blocking in terms of Northern Hemisphere energetics. The Goddard Laboratory for Atmospheres (GLA)  $4^\circ \times 5^\circ$  latitude-longitude grid general circulation model (GCM) and  $2^\circ \times 2.5^\circ$  grid GCM are employed with the GLA and Geophysical Fluid Dynamics Laboratory (GFDL) initial datasets.

The difficulty in simulating a realistic blocking due to inadequate wave-wave interaction can be attributed in part to inadequate grid resolution. Among four simulations, the simulations by the high resolution GCM produce realistically strong blockings with compatible spectral energetics as in the observed blocking episodes. The latitude-height cross sections of the energy variables of wavenumber 1 is presented to describe the dipole structure of blockings. Blocking development is also examined in time series of barotropic and baroclinic components of energy and associated conversions.

### 1. Introduction

The winter in the Northern Hemisphere is often dominated by a sequence of blocking events, and the ability of general circulation models (GCMs) to simulate blocking is a major concern in producing reasonably accurate short to medium-range forecasts (e.g., Bengtsson 1981; Miyakoda et al. 1983). In Kung and Baker (1986) we compared energetics features associated with observed and simulated blocking situations in the Northern Hemisphere winter. The observed blockings are developed and maintained by the nonlinear transfer of kinetic energy through the wave-wave interaction  $L(n)$  from cyclone-scale waves to ultralong waves. The cyclone-scale energy source is provided by baroclinic conversion  $C(n)$  from available potential energy to kinetic energy. The simulation, which fails to produce pronounced blocking, converts available potential energy to kinetic energy at all wave ranges. However, the converted energy is either cascaded down to short waves through  $L(n)$  or fed to the zonal mean component through wave-mean interaction  $M(n)$  without building up the kinetic energy of ultralong waves.

Our finding on the importance of wave-wave interaction in blocking development agrees with Saltzman's (1959) earlier proposal that the large-scale quasi-stationary flow systems are maintained by a nonlinear barotropic transfer of kinetic energy from smaller cyclone-scale disturbances which have baroclinic energy sources. It is also consistent with Hansen and Sutera's (1984) report on the necessity of nonlinear wave-wave interaction in supporting the kinetic energy of blockings, and also with Holopainen and Fortelius' (1987) study which demonstrated that the barotropic energy transfer, from the high-frequency eddies to the time-mean flow, is very strong during the blocking episode. In our recent energetics diagnosis of the observed general circulation in three-dimensional normal mode expansions (Tanaka and Kung 1988), it is shown that an upscale energy cascade during the development of winter blocking in the Northern Hemisphere is accompanied by energy transformation from baroclinic to barotropic components. Since blocking is often characterized by its barotropic structure, the barotropic and baroclinic decomposition of normal mode energetics provides additional means for the diagnosis in the zonal wavenumber domain.

It is noted that the separation of energy variables into the standard zonal mean and eddy components does not always permit the simple interpretation of the energetics mechanisms, particularly for a local synoptic system. During the blocking period a distinct local manifestation of the hemispherical circulation is apparent in and around the blocked region. However,

\* Present affiliation: Geophysical Institute, University of Alaska—Fairbanks.

Corresponding author address: Dr. Ernest C. Kung, Dept. of Atmospheric Science, University of Missouri—Columbia, Columbia, MO 65211.

from the viewpoint of the general circulation, the major blocking such as the Atlantic or Pacific blocking during the winter is not a local system. As shown in Kung and Baker (1986) the development of the Atlantic or Pacific blocking is manifested in  $n = 1$ , and that of the concurrent two blockings in the Atlantic or Pacific in  $n = 2$ . During January 1979, the month for which the simulations are analyzed, a typical Pacific blocking was formed in the early part of the month, and a typical Atlantic blocking followed toward the end of the month. Such a large blocking would permit the spectral diagnosis to reveal essential mechanisms of blocking even though it is a case analysis. The hemispherical nature and scale of the major winter blockings will also be demonstrated throughout this paper. The main objective of this paper is to diagnose the blocking simulation in the context of the energetics of the general circulation. A diagnosis of the local energy budget would be desirable; however, this approach will be left for a future study.

Since the simulation failure of winter blocking is attributable to the improper nonlinear wave-wave interaction of kinetic energy in building up the barotropic energy of ultralong waves, it is interesting to see how various simulation conditions affect this part of the energy process. In this study, four numerical simulations of the global atmosphere for January 1979 are analyzed in terms of their Northern Hemisphere energetics. The Goddard Laboratory for Atmospheres (GLA) standard  $4^\circ \times 5^\circ$  latitude-longitude grid GCM and high resolution  $2^\circ \times 2.5^\circ$  grid GCM are employed for blocking simulation, each with the GLA and Geophysical Fluid Dynamics Laboratory (GFDL) initial datasets for 0000 UTC 1 January 1979. The development of blocking is identified, and its extent and pattern examined, for each simulation. Through intercomparison among simulations and comparison with observations by Kung and Baker (1986) and Tanaka and Kung (1988), an energetics assessment is performed for these simulations. The standard spectral energetics in the zonal wavenumber domain and three-dimensional normal mode energetics are both used in this study to supplement each other.

## 2. Simulation experiments and datasets

Four simulation experiments (Expts. 1, 2, 3 and 4) were conducted for the period of 1–31 January 1979 with the GLA standard and high resolution GCMs (see Table 1). The GLA and GFDL gridded analyses of the First GARP (Global Atmospheric Research Program) Global Experiment (FGGE) at 0000 UTC 1 January were used as the initial data (see Daley et al. 1985; Kung and Baker 1986). The mean January climatology of the sea surface temperature was used in all four simulations.

The standard coarse resolution GLA GCM used in simulation experiments is the fourth-order global at-

TABLE 1. Four simulation experiments of the January 1979 global atmosphere with GLA GCMs, and blocking episodes identified in the observed and simulated Northern Hemisphere circulation. The observed periods are after Kung and Baker (1986).

	GCM grid (latitude $\times$ longitude)	1/1/79 0000 UTC initial data	Blocking period (day/mo/yr)
Observation	—	—	5/1–14/1/79 15/1–29/1/79
Expt. 1	$4^\circ \times 5^\circ$	GLA	10/1–14/1/79
Expt. 2	$4^\circ \times 5^\circ$	GFDL	9/1–13/1/79
Expt. 3	$2^\circ \times 2.5^\circ$	GLA	4/1–13/1/79 22/1–26/1/79 29/1–31/1/79
Expt. 4	$2^\circ \times 2.5^\circ$	GFDL	8/1–11/1/79

mospheric model described by Kalnay-Rivas et al. (1977) and by Kalnay et al. (1983). There are nine vertical layers equal in sigma with a uniform nonstaggered horizontal grid of  $4^\circ$  latitude by  $5^\circ$  longitude. It is based on an energy conserving scheme in which all horizontal differences are computed with fourth-order accuracy. A 16th-order Shapiro (1970) filter is applied every 2 hours on the sea level pressure, potential temperature, and wind fields. In this scheme, wavelengths longer than four grid lengths are resolved accurately without damping. Wavelengths shorter than four grid lengths, which would otherwise be grossly misrepresented by the finite differences, are filtered out while they are still infinitesimal. The  $2^\circ$  latitude by  $2.5^\circ$  longitude version (high resolution version) of the GLA GCM is identical to the coarse resolution version with respect to the physical parameterizations. The timestep of the hydrodynamics is 3.75 min in the high resolution version compared to 7.5 min in the coarse resolution version and an eighth-order Shapiro (1970) filter is used rather than the 16th-order filter used in the coarse resolution model.

The GLA analysis scheme (Baker 1983) used to produce initial conditions for Expts. 1 and 3, as summarized in Daley et al. (1985), employs a univariate successive correlation method for the height, horizontal wind components, and relative humidity on pressure surfaces. All of the analyses are smoothed and then analysis-minus-first-guess differences are interpolated to the model sigma levels. The assimilation procedure involves the intermittent analysis of batches of data grouped in a  $\pm 3$  h window about each synoptic time. The wind and height fields are updated independently without any explicit coupling or balancing. In contrast to the GLA approach, the GFDL assimilation procedure employs a spectral, rhomboidal 30, 18 level, general circulation model with continuous data insertion at every time step. The objective analysis scheme used to provide the initial conditions for Expts. 2 and 4, (see Daley et al. 1985), utilizes a univariate optimum interpolation procedure on pressure surfaces. Nonlin-

ear normal mode initialization is applied every 6 hours during the assimilation.

The four simulation datasets and GLA gridded data of the FGGE observations analyzed in this study include twice-daily values of geopotential height, temperature, humidity, horizontal wind and vertical velocity at 0000 and 1200 UTC, which are given on the  $4^\circ \times 5^\circ$  latitude-longitude grid at 1000, 850, 700, 500, 400, 300, 250, 200, 150, 100, 70, and 50 mb at 0000 and 1200 UTC.

### 3. Scheme of analysis

Table 2 lists symbols, definitions, and variables used in this paper. The computational analysis of the standard spectral energetics in the zonal wavenumber domain is based on Saltzman's (1957, 1970) formulation of equations of kinetic energy:

$$\frac{\partial K(0)}{\partial t} = \sum_{n=1}^N M(n) + C(0) - D(0) \quad (1)$$

$$\frac{\partial K(n)}{\partial t} = -M(n) + L(n) + C(n) - D(n), \quad n \neq 0. \quad (2)$$

Equations (1) and (2) state the balance requirement over the total mass of the atmosphere in a closed domain. In this study, transformation terms are obtained so that the energy equations also hold at each point in the meridional-height cross section. This is done by the use of the advective form instead of the convergence form in computing the nonlinear interaction terms  $M(n)$  and  $L(n)$ , and also by replacing  $C(n)$  with  $-\mathbf{V} \cdot \nabla \Phi$  at  $n$ . For the discussion of baroclinic conversion,  $C(n)$  is computed explicitly with the vertical motion and specific volume. In computing spectral energetics over the Northern Hemisphere, the energetics variables evaluated in the meridional-height cross section are integrated over the Northern Hemisphere. The dissipation terms  $D(n)$  of kinetic energy in Eqs. (1) and (2) are obtained as residual terms to balance the respective equations. The maximum wavenumber computed for energy variables is  $n = 36$ .

The analysis scheme of normal mode energetics is based on Tanaka (1985) and Tanaka and Kung (1988). The equation of total energy,  $E = K + P$  for a component of three-dimensional normal mode expansion may be written as

$$\partial E_{nlm} / \partial t = A_{nlm} + B_{nlm} + F_{nlm}. \quad (3)$$

The total energy pertaining to  $m = 0$  is defined as barotropic energy, whereas the sum of the energy for  $m \neq 0$  is baroclinic energy. The maximum vertical index computed is  $m = 10$ . The construction of basis functions for very small equivalent height beyond  $m = 10$  is very difficult and quite unpredictable. A total

TABLE 2. Symbols, definitions, and variables.

$t$	time
$p$	pressure
$p_s$	constant surface pressure
$\mathbf{V}$	horizontal wind vector
$u$	zonal wind speed
$v$	meridional wind speed
$\Phi$	geopotential
$n$	zonal wavenumber
$l$	meridional index
$m$	vertical index
$h_m$	equivalent height for $m$ th vertical index
$w_{nlm}$	three-dimensional spectral expansion coefficient
$\nabla$	horizontal del operator along an isobaric surface
$\sigma$	sigma ( $p/p_s$ )
$g$	acceleration of gravity
$\rho_0$	basic density
$H$	scale height of the isothermal atmosphere
$\lambda$	longitude
$I$	blocking index as defined in Eq. (4)
$Z$	geopotential height of the 500 mb surface
$z(n)$	geopotential height at wavenumber $n$ normalized by the factor $\sigma^{1/2}$
$K(n)$	kinetic energy at wavenumber $n$
$M(n)$	transfer of $K(n)$ to $K(0)$ where $n \neq 0$
$L(n)$	transfer of eddy kinetic energy from all other wavenumbers to $K(n)$ where $n \neq 0$
$C(n)$	conversion of $P(n)$ to $K(n)$
$D(n)$	dissipation of $K(n)$
$-\mathbf{V} \cdot \nabla \Phi$	production of kinetic energy by cross-isobaric motion
$K$	kinetic energy over the total mass of the atmosphere
$P$	available potential energy over the total mass of the atmosphere
$E$	total energy, $K + P$
$B$	nonlinear interaction of $K$
$A$	nonlinear interaction of $P$
$F$	net energy source and sink due to diabatic processes over the total mass of the atmosphere
ERR	error variance for simulations

of 50 meridional indices are used in this study, including 26 Rossby modes, 12 eastward gravity modes, and 12 westward gravity modes, which are sufficient to describe the large-scale energy characteristics (see Tanaka 1985). The zonal wavenumber  $n$  is truncated at  $n = 15$ . Surface wind at  $p = p_s$  has been assumed to vanish as in Tanaka and Kung (1988).

Using the method of normal mode expansion, we can assess the forecast error in the simulated atmosphere by the distance between the spectral expansion coefficients of observation  $w_{nlm}$  and simulation  $\hat{w}_{nlm}$ , where the caret designates variables for simulations. The error variance ERR in simulations may be given as a sum of the following quantities of the normal mode expansion:

$$\text{ERR}_{nlm} = \frac{1}{2} p_s h_m |\hat{w}_{nlm} - w_{nlm}|^2. \quad (4)$$

A dimensional factor  $p_s h_m$  is used so that the error variance has physical units of  $\text{J m}^{-2}$ . By means of the inverse transforms of vertical and Fourier-Hough transforms, it may be shown that the sum of  $\text{ERR}_{nlm}$

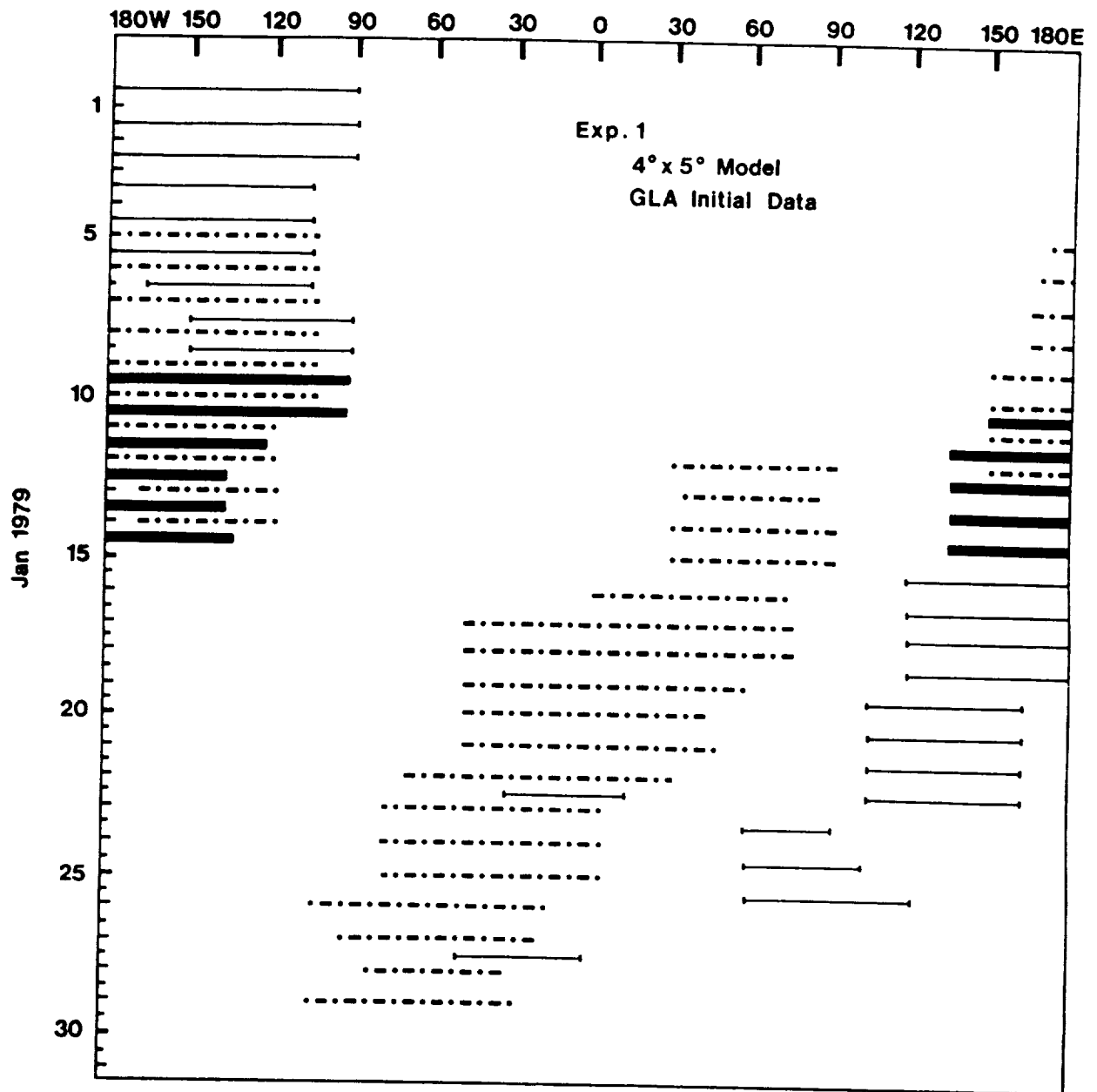


FIG. 1. Longitude-time diagram of significant ridges as noted by horizontal bars during January 1979 in Expt. 1 as identified in the daily 0000 UTC 500 mb charts. Bold lines are for blocking. Dot-dashed lines are for observed blockings after Kung and Baker (1986).

has the same form as total energy  $E = K + P$ , in which the dependent variables  $u$ ,  $v$ , and  $\Phi$  have been replaced by  $\hat{u} - u$ ,  $\hat{v} - v$ , and  $\hat{\Phi} - \Phi$ .

For energetics analysis over the Northern Hemisphere, the basic variables are expanded in the vertical normal modes and zonal harmonics without further expansion in Hough functions. The energetics variables of barotropic and baroclinic components are then integrated over the hemisphere. In this case spectral components of cross-equatorial flux are involved in the energy balance. However, it has been confirmed

(Kung 1988) that contributions from such cross-equatorial flux are negligibly small in the observed atmosphere except for  $n = 0$ . This situation is also the same for all simulations in this study. Unless stated otherwise, the results of  $E_{nlm}$ ,  $A_{nlm}$  and  $B_{nlm}$  in this study are computed based on the Northern Hemisphere data.

Standard spectral energetics for the observed blocking situation as compared with simulations in this study are adopted from Kung and Baker (1986), and the normal model energetics from Tanaka and Kung (1988). Additional energetics computations for the

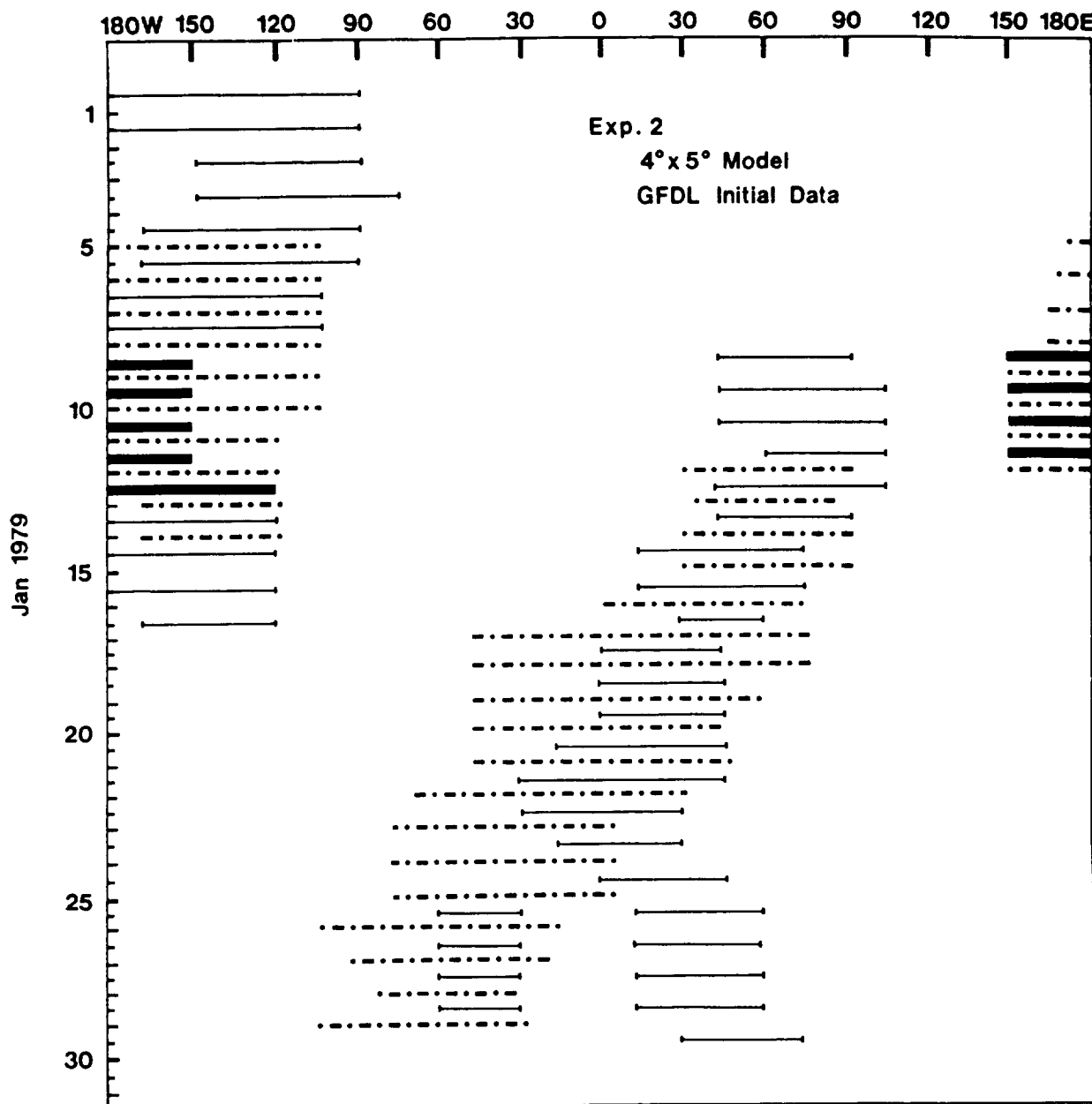


FIG. 2. As in Fig. 1, but for Expt. 2.

observed circulation as needed is performed with the GLA gridded analysis of the FGGE observations.

#### 4. Simulated blockings and spectral energetics

Following the procedures of Kung and Baker (1986), the longitudinal width of significant ridges in the  $46^{\circ}$ – $66^{\circ}$ N belt are identified with the daily 500 mb charts of the simulated circulation in Figs. 1–4 for the four simulations. The horizontal segments in the longitude–time diagrams represent the longitudinal sector, in which the westerly flow is interrupted because of the

presence of ridges. The blocking cases are further identified as bold lines for these longitudinal sectors. A blocking is recognized when the following index  $I$  at longitude  $\lambda$  is greater than 50 m along the longitudinal sector in the figures:

$$I(\lambda) = Z(\lambda, 66^{\circ}\text{N}) - Z(\lambda, 46^{\circ}\text{N}) \quad (5)$$

where  $Z$  is the geopotential height at 500 mb. This criterion is based on the common characteristic of diffluent and meridional types of blocking. In both types of blocking, a quasi-meridional dipole is formed by a

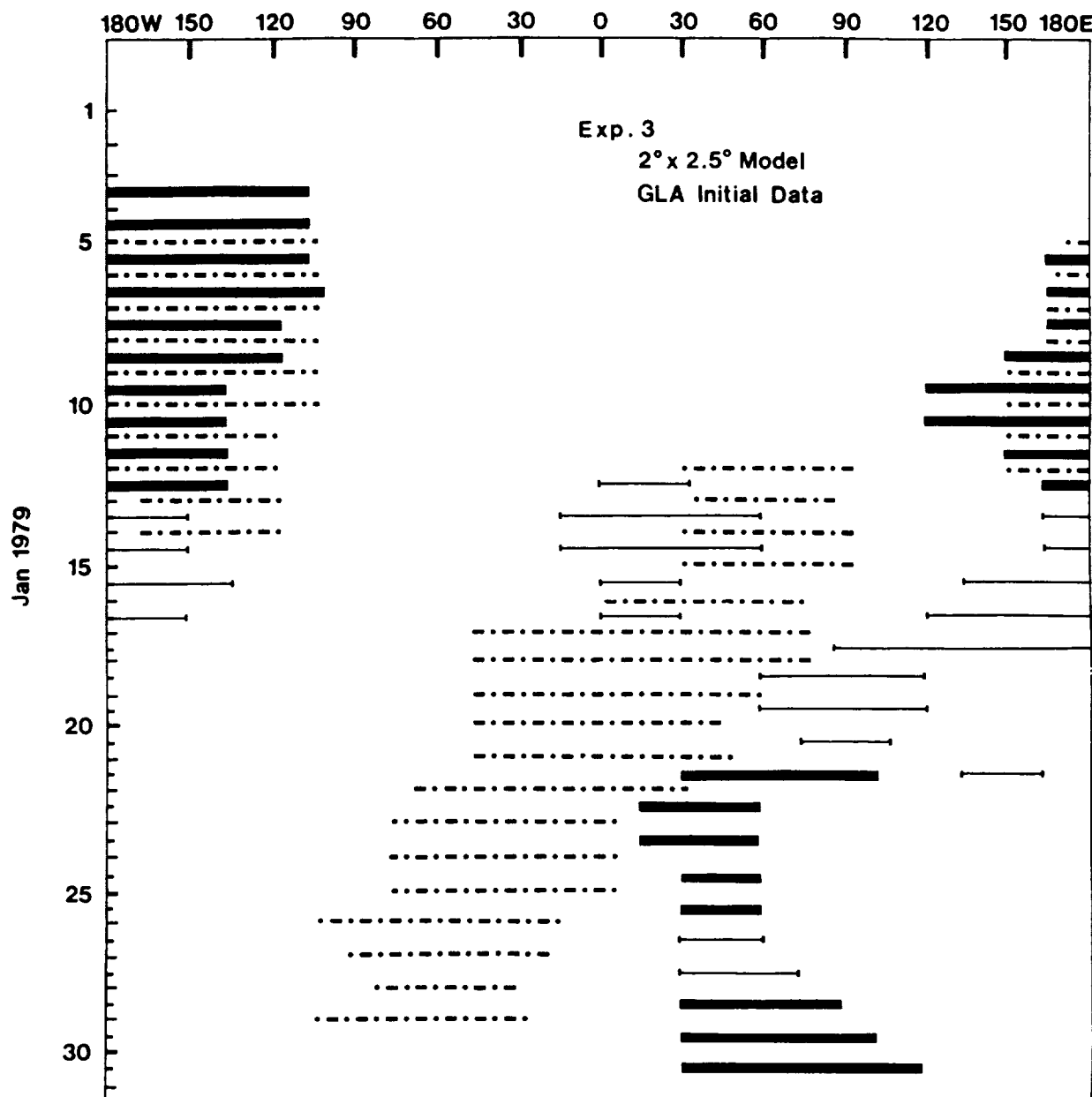


FIG. 3. As in Fig. 1, but for Expt. 3.

high pressure cell poleward and a low pressure area equatorward (see Lejenäs and Økland 1983). For the cases of tilted orientation of meridional dipole, and cases of blocking which are partially out of the chosen latitudinal band,  $Z(\lambda \pm 5^\circ, 66^\circ\text{N})$  is substituted for  $Z(\lambda, 66^\circ\text{N})$  in Eq. (5) in the additional scan of the circulation pattern. The blocking identification in this method is verified to be consistent with the results of careful manual inspection of the flow pattern (see Kung and Baker 1986). Figures 1–4 also contrast the simulated blockings with the observed blockings by Kung and Baker which are shown with dot–dashed lines.

The periods of identified blocking episodes in the Northern Hemisphere are listed for the four simulations and compared with those of the observed episodes in Table 1. Comparing the simulated blockings with those observed for their latitudinal locations (Figs. 1–4) and periods (Figs. 1–4 and Table 1), it is apparent that there is a considerable difference between the simulation and observation and among the four simulations. The simulations in Expts. 1 and 2 have much shorter blocking periods than the observation. The longitudinal extents of the simulated blockings are more limited than the observation, and some dislocation of blocks

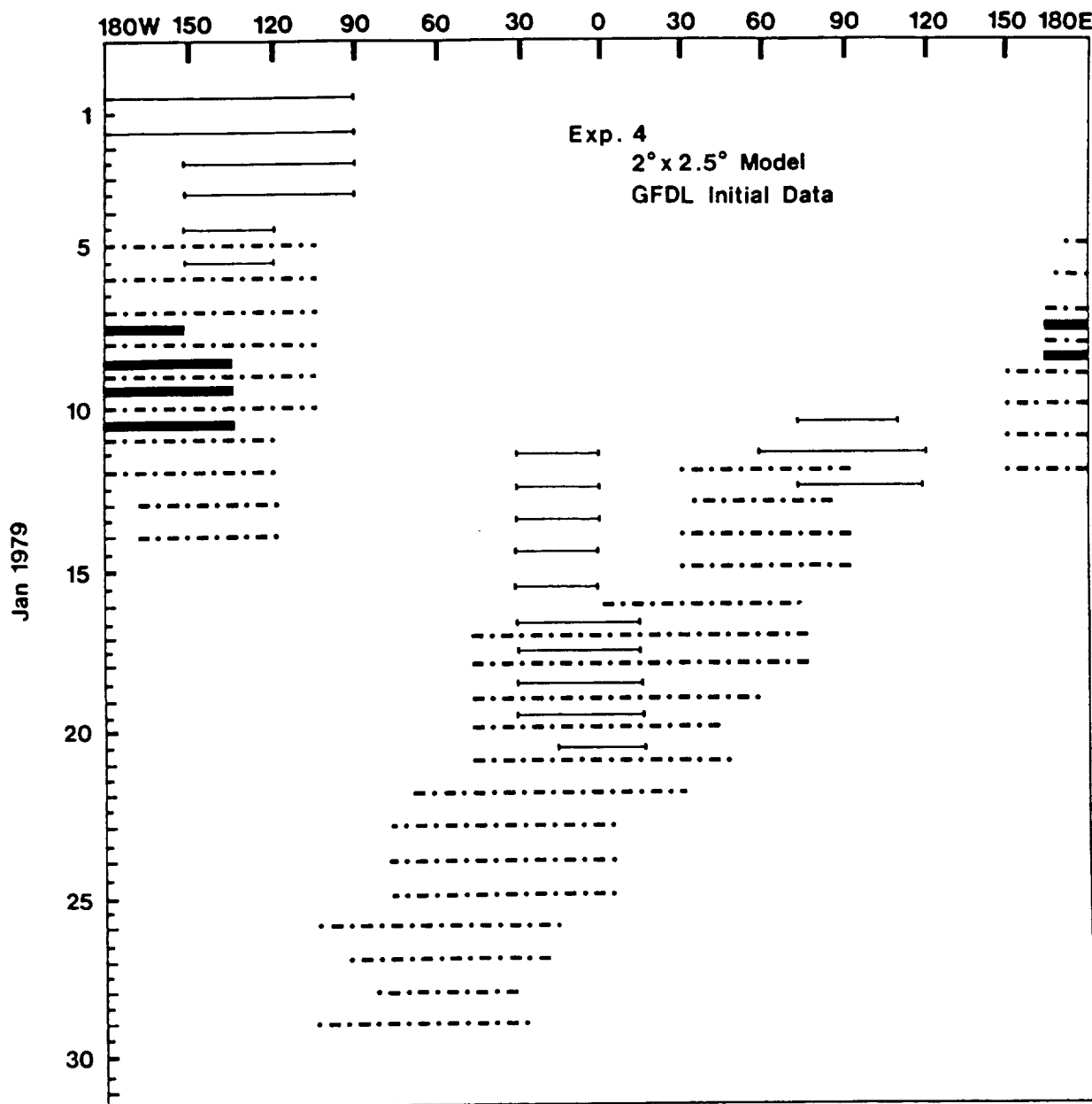


FIG. 4. As in Fig. 1, but for Expt. 4.

is apparent. Figures 5 and 6 verify that the Pacific blocking episodes in Expts. 1 and 2 are much weaker than those of the observation and Expts. 3 and 4. The circulation patterns in Figs. 5 and 6 are for a 5-day period synchronized at 9–13 January. Among the simulations, Expts. 3 and 4 by the high resolution GCM were able to generate realistically strong blocking. Expt. 3 is noted for its large amplitude of blocking, and Expt. 4 for its close resemblance of the phase of the block to that of the observation. Figure 3 also indicates that Expt. 3 produced another blocking episode toward the end of the simulation period although the block is dis-

located to the east of the observed block. This is a distinct contrast to the other three simulations in that it was able to amplify the ultralong waves through the entire 1-month period of simulation.

Figure 7 illustrates the error variance growth of the simulations for zonal eddies ( $n = 1-15$ ) starting from the initial data of 0000 UTC 1 January. The GFDL analyses of the FGGE are used to represent the observed atmosphere for evaluating the prediction error in model simulations. For comparison, the persistence error is presented starting from the same date. The persistence error reaches its saturation level around

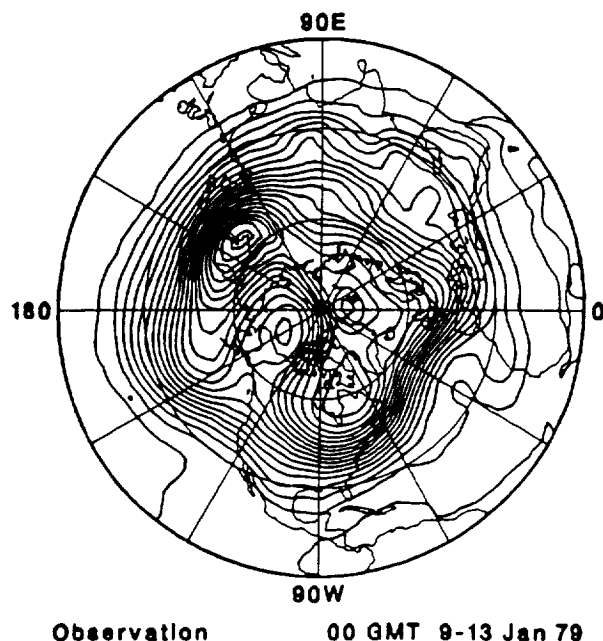


FIG. 5. Observed 5-day mean 500 mb circulation during the Pacific blocking.

days 4 to 6. In contrast, the simulation error energies reach their saturation levels around 8 to 10. Evidently, the high resolution models (solid line) perform better compared to the low resolution models (dotted line). According to Dalcher and Kalnay (1987), the dynamical predictability of a model is determined by the day when the error energy reaches 95 percent of the saturated level. Growing prediction errors show the predictability limits of GLA model simulations at about 7 to 10 days for Expts. 1 to 4.

The circulation patterns of simulations, as shown in Fig. 6, indicate certain predictability of GCMs in blocking formation during the period of 9–13 January. In particular, Expts. 3 and 4 by the high resolution GCM formed a clear, major blocking in the Pacific which is comparable with the observation. This seeming inconsistency with the forecast skill, as shown in Fig. 7, may be explained by a scale dependency of predictability in the atmospheric circulation. Bengtsson (1981) found that the atmospheric predictability increases in a blocking situation. Shukla's (1981) study indicated that ultralong waves possess considerable extended predictability (up to 30–45 days) when compared to shorter waves. This is confirmed collectively by contributors in Holloway and West (1984). Since the prediction error variance in Fig. 7 is for the summation of zonal eddies  $n = 1-15$ , it indicates the predictability of the total field of motion rather than that of ultralong waves which are responsible for blocking formation. From Fig. 7 it is apparent that Expt. 4 was the best of the four simulations of the Northern Hemi-

sphere circulation after the error energy reached a saturation level. Presumably, however, due to extended predictability of ultralong waves, Expt. 3 was also able to form a distinct blocking pattern over the Pacific.

The baroclinic conversion  $C(n)$ , wave-wave interaction  $L(n)$ , wave-mean interaction  $M(n)$ , and dissipation  $D(n)$  over the Northern Hemisphere for the observed circulation and four simulations are listed in Table 3 for  $n = 1-36$  for the period 5–9 January 1979 when the blocking is in the developmental stage. These four transformation variables determine the eddy kinetic energy balance of individual wavenumbers. Kung and Baker (1986) showed that the change in the available potential energy occurs following the blocking development rather than preceding the blocking. This is consistent with the basically barotropic nature of blocking development, and the budget of available potential energy needs not be examined in this study in connection with blocking development.

It is apparent that the resemblance between energetics is stronger for the two high resolution simulations than for the two low resolution cases. Both Expts. 3 and 4 show large  $L(1)$  as in the observed blocking. In contrast, Expts. 1 and 2 have significantly weak  $L(1)$  and large energy input at the shortwave range  $L(11-36)$ . It is also apparent that in the high resolution simulations, Expts. 3 and 4, an upscale input to  $n = 1$  is provided through the wave-wave interaction  $L(1)$  from the source at the synoptic-scale range, including the contribution from  $L(3)$  and  $L(4)$ . Although  $L(1)$  in Expts. 3 and 4 is large, it is still smaller than that in the observation, whereas  $L(2)$  is noticeably larger. In comparing Expts. 3 and 4, Expt. 3, with the GLA initial data, seems to provide better energy input at  $n = 1$ . As in the observation, Expts. 3 and 4 show positive values of  $L(5)$ , but they are smaller than that in the observation. In the computation of  $L(n)$  no adjustment is made to ensure the balance among wavenumbers. It is seen that the values of  $L(1-36)$  in the observation and Expt. 3 are reasonably small, whereas those in Expts. 1 and 2 are very large. The large residual values of  $L(1-36)$  are attributable to the fact that the integration is only for the Northern Hemisphere, and also to the application of Shapiro (1970) filtering in the model integration, which will result in an inconsistency of simulation data with diagnostic equations. These effects are apparently minimized in Expt. 3.

The wave-mean interaction  $M(n)$  as shown in Table 3 seems to indicate that its spectral distribution is affected by the initial data. For Expts. 1 and 3 with the GLA initial data a comparable wave-mean interaction with the observation at the synoptic and shortwave range  $n = 5-36$  is indicated. When the GFDL data are used to initialize the high resolution GLA GCM in Expt. 4, a very large flow of kinetic energy from eddies to the zonal mean motion is observed at  $n = 3$  and 6–10, an obvious distortion of energy flow in view of the observed values. This may have prevented a stronger



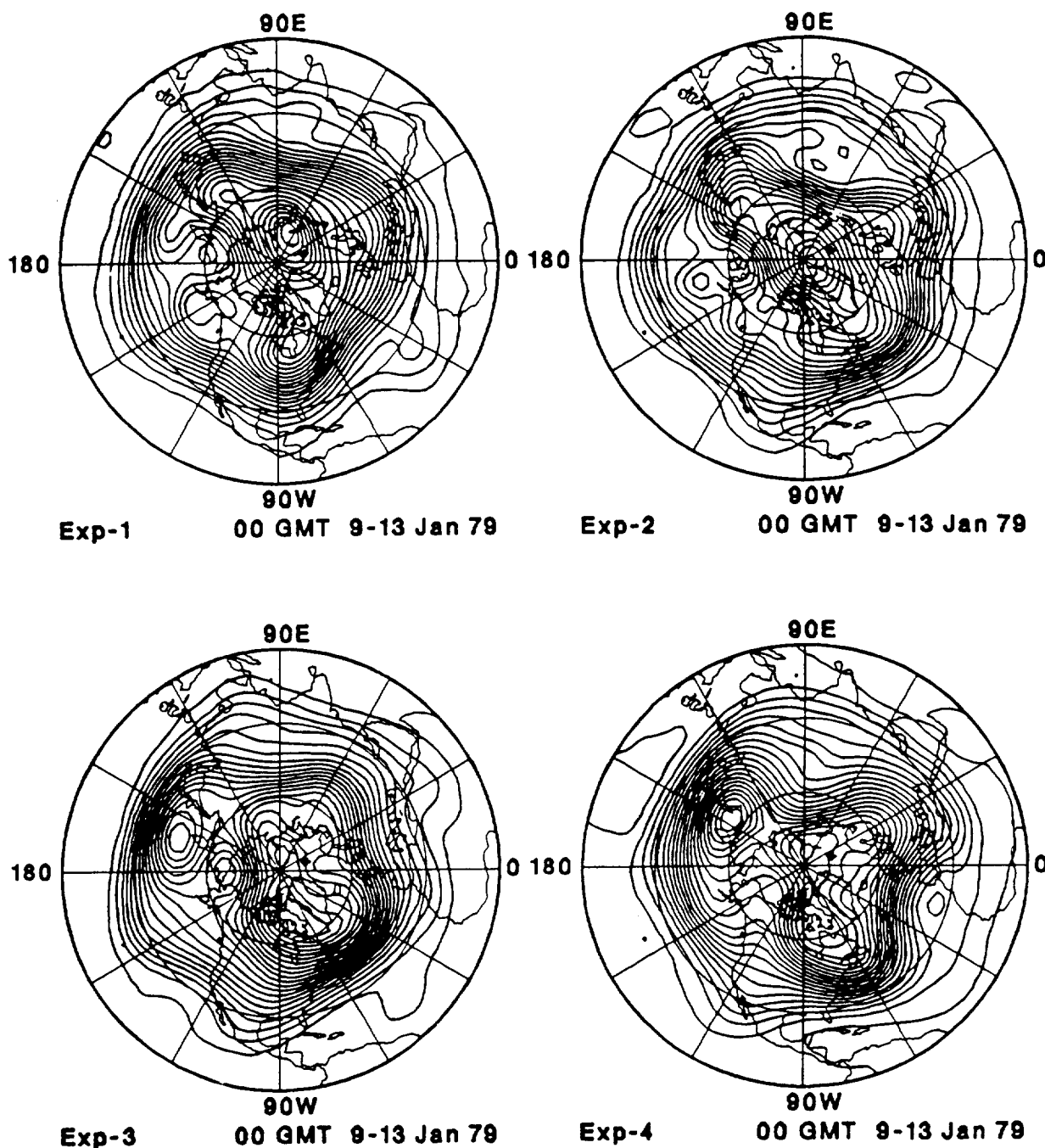


FIG. 6. As in Fig. 5, but for the four simulations.

input in Expt. 4 at  $n = 1$  as shown in a relatively weak  $L(1)$  in comparison with that in Expt. 3. It appears that the model influence contained in the initial data may amplify in a GCM integration, particularly when the high resolution GCM is used in simulation.

There is a sufficient baroclinic conversion  $C(n)$  in all simulations to provide the energy source for barotropic processes of  $L(n)$  and  $M(n)$ . The simulations

actually generate more kinetic energy than the observations, which is enhanced in the high resolution simulation. The  $C(1-36)$  in Expts. 3 and 4 is more than 30% higher than in the observation. There are some notable differences in  $C(n)$  at the ultralong-wave range among simulations. However, the patterns in this are not identified with any specified differences among experiments. All simulations have more than enough

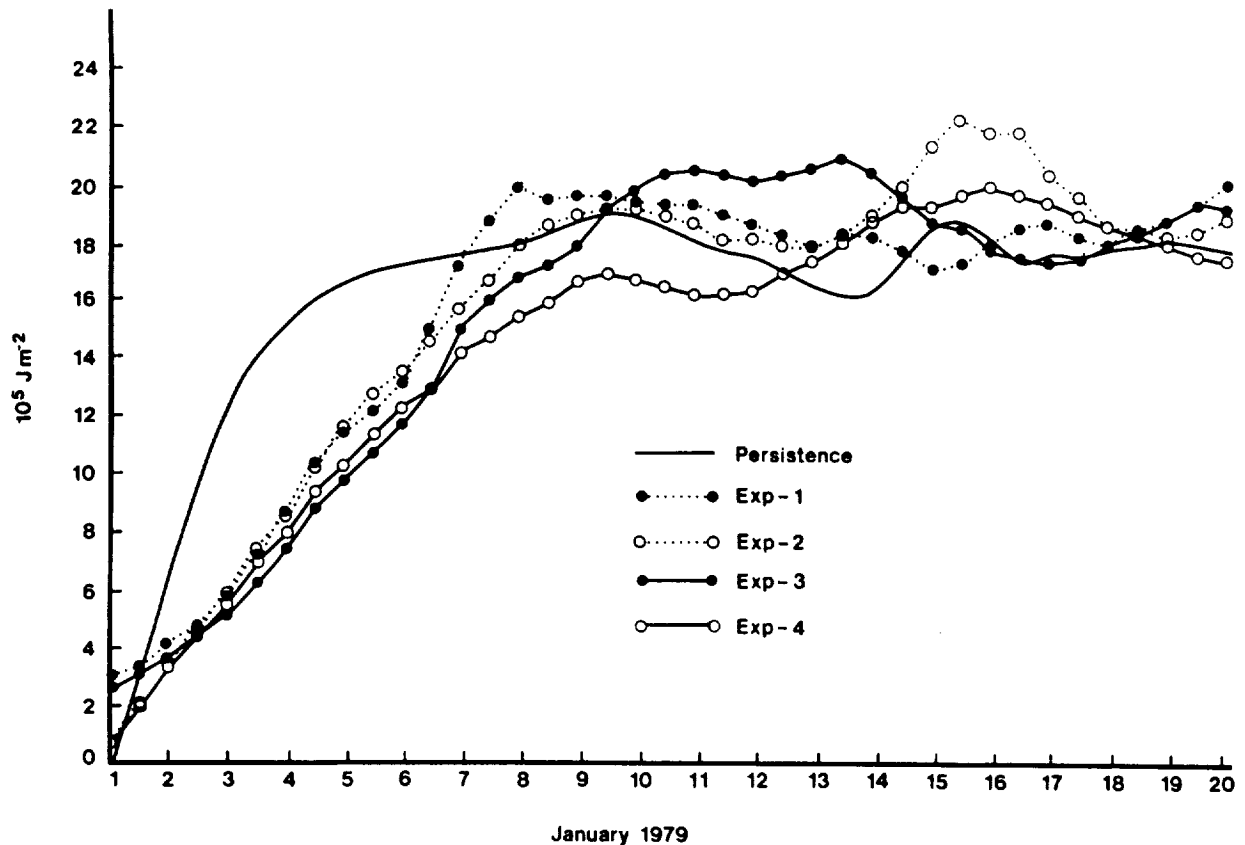


FIG. 7. Growth of prediction error variance for  $n = 1-15$  in Expts. 1 to 4. Persistence error starting from 1 January is indicated by solid line without a dot.

baroclinic energy sources, but the barotropic part of transformations tend to fail to provide as much kinetic energy input at  $n = 1$  as in the observation.

The value  $D(n)$  obtained as the residual term of Eq. (2), which is customarily referred to as dissipation, represents the sink of kinetic energy from the specified scale  $n$ . Thus  $D(n)$  can be any process of energy cascade by the scales of motion that cannot be observed with the given grid resolution. All four simulations differ from the observation in their respective spectral distribution of  $D(n)$ . While the observation shows its maximum dissipation at  $n = 2$  and 3, the simulations have their large dissipation in the shorter wave range  $n = 6-36$ . It is particularly noteworthy that the simulations with the coarse grid GCM, Expts. 1 and 2, have a very high dissipation at the shortwave range of  $n = 11-36$ . This is consistent with the fact that these simulations generate unduly intense circulation at shortwave range (see Baker and Brin 1985), which shows a marked improvement with the high resolution GCM.

From the listing of eddy kinetic energy transformations, it is apparent that the failure in simulating the realistic blocking can be attributed in part to in-

adequate grid resolution. The coarse  $4^\circ \times 5^\circ$  grid of the standard GLA GCM results in the downscale energy cascade, preventing a proper upscale input at  $n = 1$ . It is also shown that the differences in initial datasets obviously result in differences in the spectral energetics. The high resolution GLA GCM with the GFDL initial data produced excessively strong wave-mean interaction, which may have prevented the wave-wave interaction  $L(1)$  from reaching a level close to that of the observation. It is relevant to point out that the spectral energetics obtained in this study are for the entire Northern Hemisphere. Our ongoing study indicates that the energetics budget acquired for a limited latitudinal belt of blocking formation, is comparable to that of the Northern Hemisphere, and the energetics characteristics, as discussed above, will be seen more clearly.

### 5. Dipole structure

The widely recognized common characteristic of the blocking situation is the quasi-meridional dipole structure, as shown in Fig. 5 in connection with the fully developed Pacific blocking. In the zonal spectral analy-

TABLE 3. Transfer of eddy kinetic energy by eddy conversion  $C(n)$ , wave-wave interaction  $L(n)$ , wave-mean interaction  $M(n)$ , and dissipation  $D(n)$  over the Northern Hemisphere in the observed and simulated circulation for the period 5–9 January 1979. The observed values are taken from Kung and Baker (1986). Units are  $10^{-2} \text{ W m}^{-2}$ .

Datasets	$C(1)$	$C(2)$	$C(3)$	$C(4)$	$C(5)$	$C(6-10)$	$C(11-36)$	$C(1-36)$
Observation	2	50	64	30	41	99	30	316
Expt. 1	-5	20	20	44	80	153	73	385
Expt. 2	27	8	56	37	34	155	74	391
Expt. 3	18	29	30	59	64	151	70	421
Expt. 4	6	50	75	50	45	149	57	432
Datasets	$L(1)$	$L(2)$	$L(3)$	$L(4)$	$L(5)$	$L(6-10)$	$L(11-36)$	$L(1-36)$
Observation	67	2	-25	-22	26	-56	7	-1
Expt. 1	24	-1	-30	-13	-16	-50	17	-69
Expt. 2	16	29	-48	-18	-11	-68	23	-77
Expt. 3	52	10	-33	-18	10	-25	9	5
Expt. 4	42	6	-22	-22	8	-11	16	17
Datasets	$M(1)$	$M(2)$	$M(3)$	$M(4)$	$M(5)$	$M(6-10)$	$M(11-36)$	$M(1-36)$
Observation	19	-5	2	0	16	15	-2	45
Expt. 1	-3	-4	8	4	25	15	-3	42
Expt. 2	8	-6	9	2	5	8	-2	24
Expt. 3	8	-6	1	12	21	19	1	56
Expt. 4	10	-4	40	13	2	41	3	105
Datasets	$D(1)$	$D(2)$	$D(3)$	$D(4)$	$D(5)$	$D(6-10)$	$D(11-36)$	$D(1-36)$
Observation	31	73	69	26	28	44	38	309
Expt. 1	22	17	25	21	20	69	140	314
Expt. 2	20	22	31	24	15	84	132	328
Expt. 3	34	35	30	31	40	86	89	345
Expt. 4	28	41	28	18	30	76	76	297

sis of the isobaric height field of the observed circulation, this dipole structure is apparent as the amplitude maxima for  $n = 1$  at  $45^\circ$  and  $75^\circ\text{N}$ , as shown in the latitude-height cross section of Fig. 8, but not for other wavenumbers. The cross section is for the period 7–11 January when the Pacific blocking is in its full development. The hemispherical scale of this blocking episode is confirmed by the fact that its structure is adequately described by  $n = 1$ , as shown in Fig. 8. To remove the effects of the density stratification at high altitudes, which results in the large amplitudes of the geopotential and wind fields, the vertical structure of geopotential height is multiplied by  $\sigma^{1/2}$  where  $\sigma = p/p_s$ , and those of energy and energy transformations with the basic density of  $\rho_0 = p(gH)^{-1}$  where  $H = 8000 \text{ m}$  (see Matsuno 1970) in the latitude-height cross sections shown in this paper. The vertical coordinate in Figs. 8–13 is calibrated by  $H \times \ln(p_s/p)$  in the unit of  $m$ .

The latitude-height distribution of kinetic energy for  $n = 1$ , as shown in Fig. 9, is consistent with that of  $Z(1)$  in Fig. 8. The two cores of maximum kinetic energy between  $50^\circ$  and  $60^\circ\text{N}$  and around  $80^\circ\text{N}$  are the projection of a fully developed blocking situation. The partition of  $K(1)$  into the  $u$  and  $v$  components in the same figure further indicates that, for the  $50^\circ$ – $60^\circ\text{N}$  core the zonal component is the sole contributor, whereas the core at the higher latitudes is supported by both meridional and zonal components. The sources of kinetic energy are examined in Fig. 10. The latitudinal distribution of kinetic energy production  $-\mathbf{V} \cdot \nabla \Phi$

for  $n = 1$  is consistent with that of  $K(1)$ . At these latitudes of maximum  $K(1)$ , the kinetic energy is produced in the lower and upper troposphere to support the circulation against the dissipation. In terms of nonlinear wave-wave interaction  $L(1)$ , the kinetic energy input at  $n = 1$  from the shorter waves has two clearly identified maxima where the two cores of maximum kinetic energy are observed. The wave-mean interaction  $M(1)$  shows that its latitude-height distribution does not appear to be related to the dipole structure of blocking.

As shown in Kung and Baker (1986), in the observed circulation the baroclinic energy conversion  $C(1)$  is not directly related to the blocking development. The baroclinic energy source always exists in a sufficient amount to support the circulation against the dissipation and to provide the kinetic energy source for nonlinear interactions. This is seen in the consistency of  $K(1)$  and  $-\mathbf{V} \cdot \nabla \Phi$  for  $n = 1$  in their latitudinal variations. The appearance of  $L(1)$  maxima at the core regions of kinetic energy maximum is a specific phenomenon in association with the development of blocking, and disappears once the blocking enters the decaying stage.

In comparing the latitude-height cross sections of simulations with those of the observed circulation, the differences in the dipole structure of blocking are striking. Except for Expt. 3, all other simulations show weak dipoles in terms of  $K(1)$  in Fig. 11 in comparison with the observation in Fig. 9. It is stronger in Expt. 3 but is still weaker than that in the observation. For Expt.

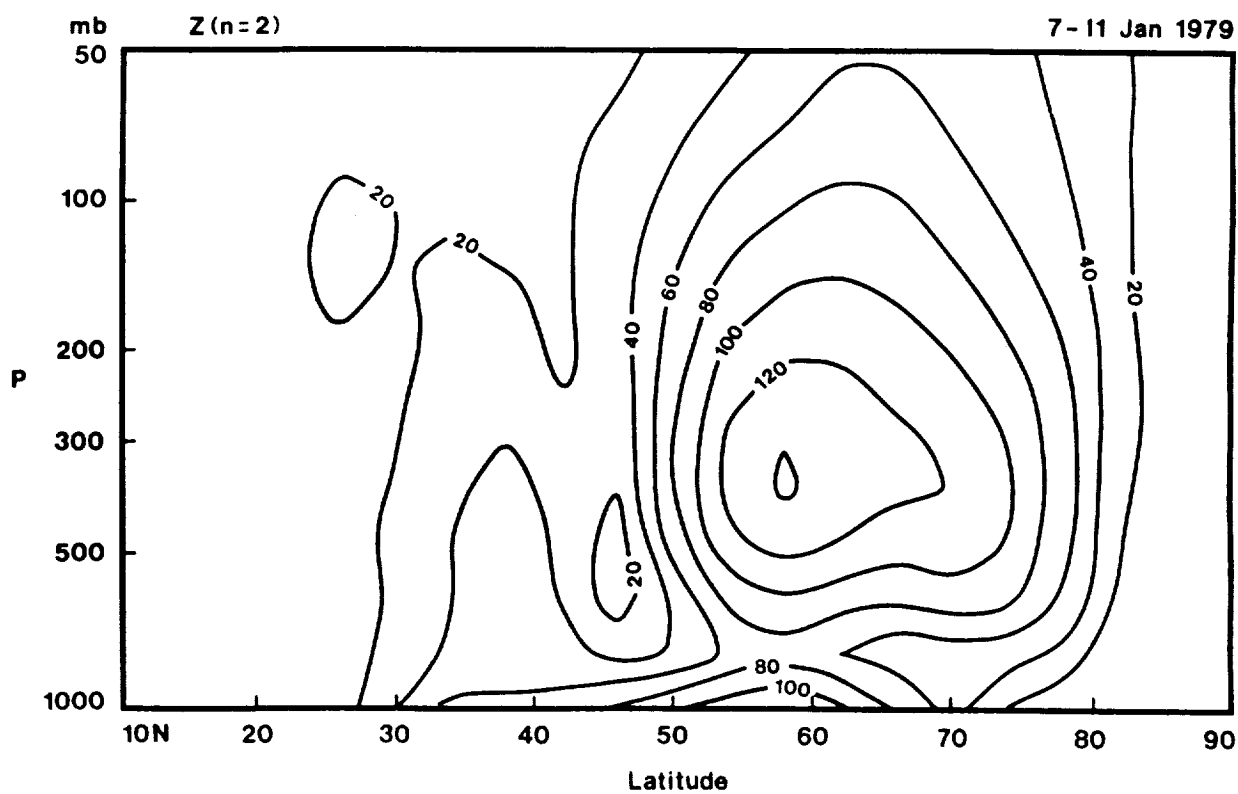
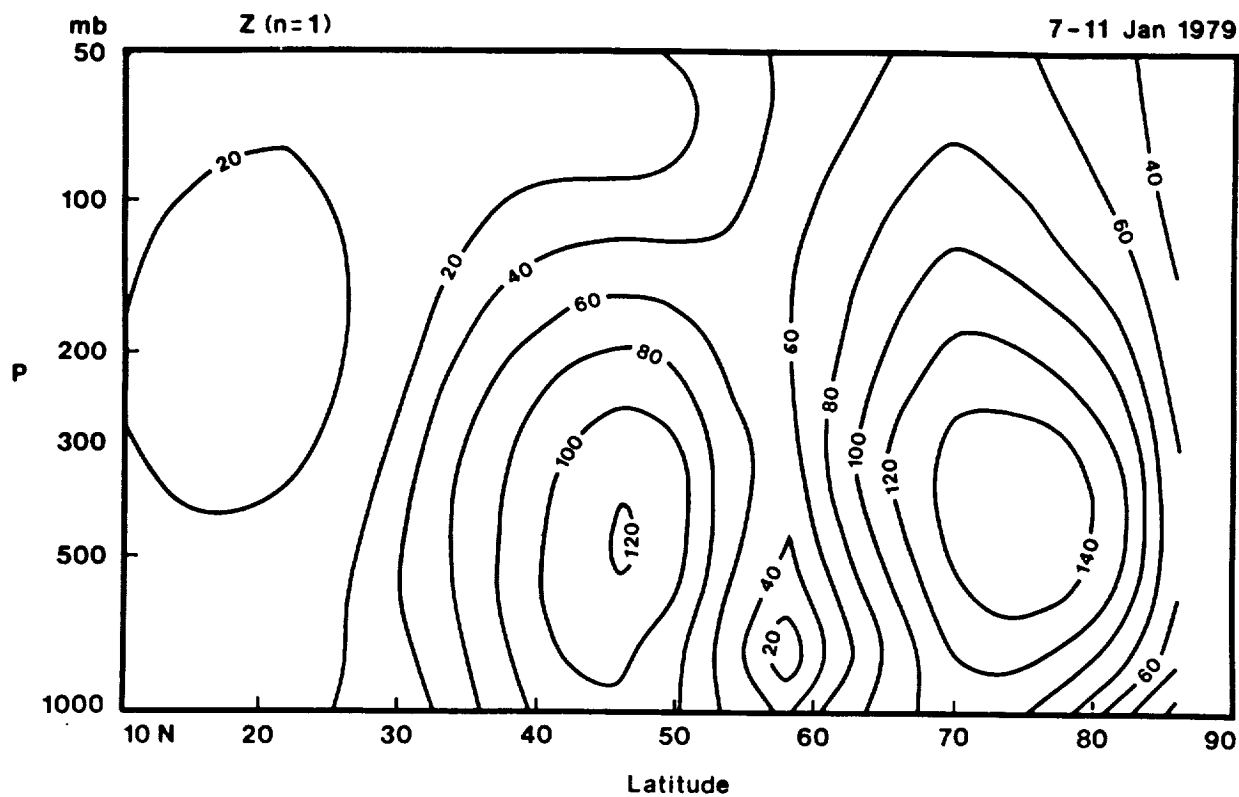


FIG. 8. Meridional-height cross sections of geopotential height amplitude  $z$  in the Northern Hemisphere for  $n = 1$  and 2. The values are observed 5-day means for 7-11 January 1979, multiplied by  $(p/p_s)^{1/2}$ , and expressed in the unit of  $m$ .

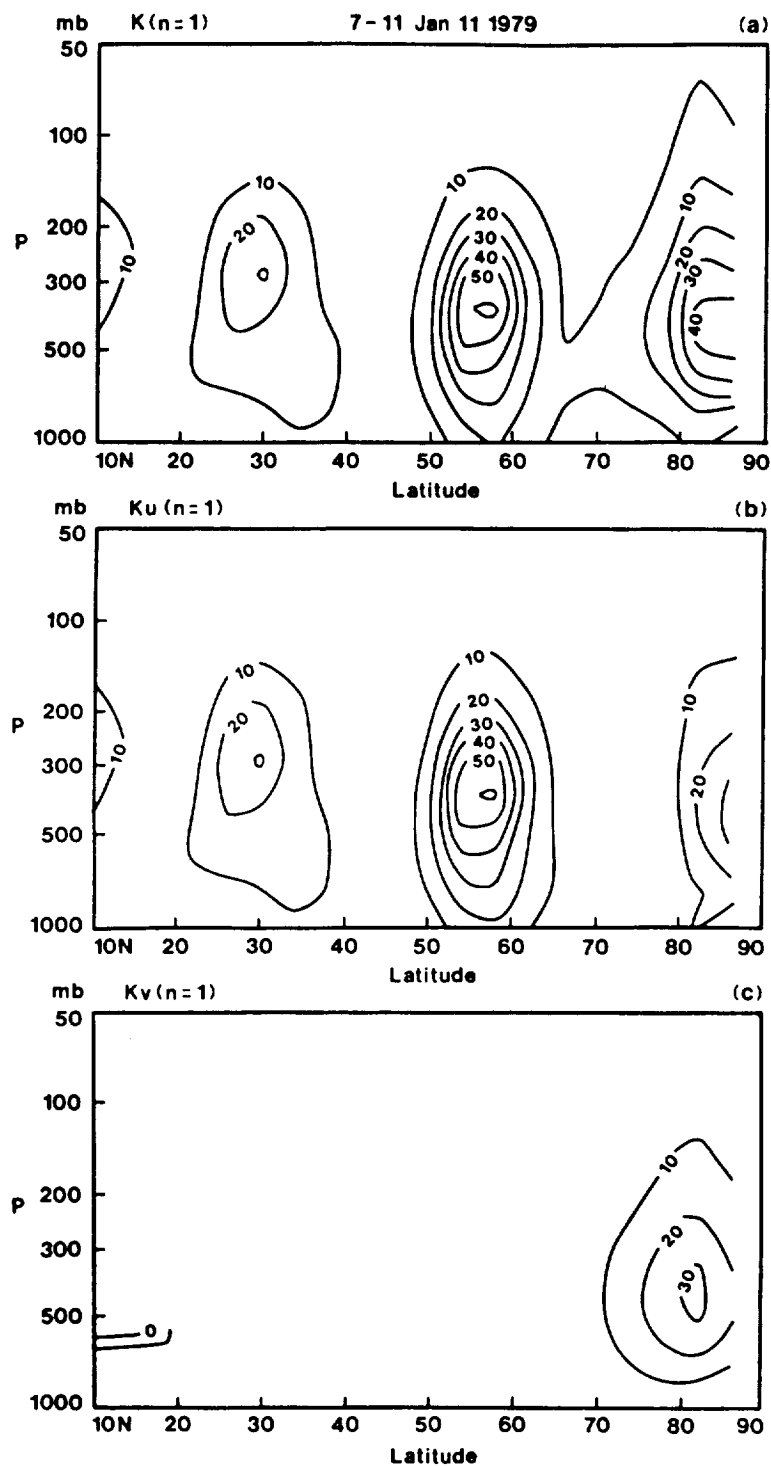


FIG. 9. Meridional-height cross sections of kinetic energy  $K$ , zonal component  $K_u$  and meridional component  $K_v$  in the Northern Hemisphere for  $n=1$ . The values are 5-day means for 7–11 January 1979, multiplied by  $\rho_0$  and expressed in the units of  $\text{J m}^{-3}$ .

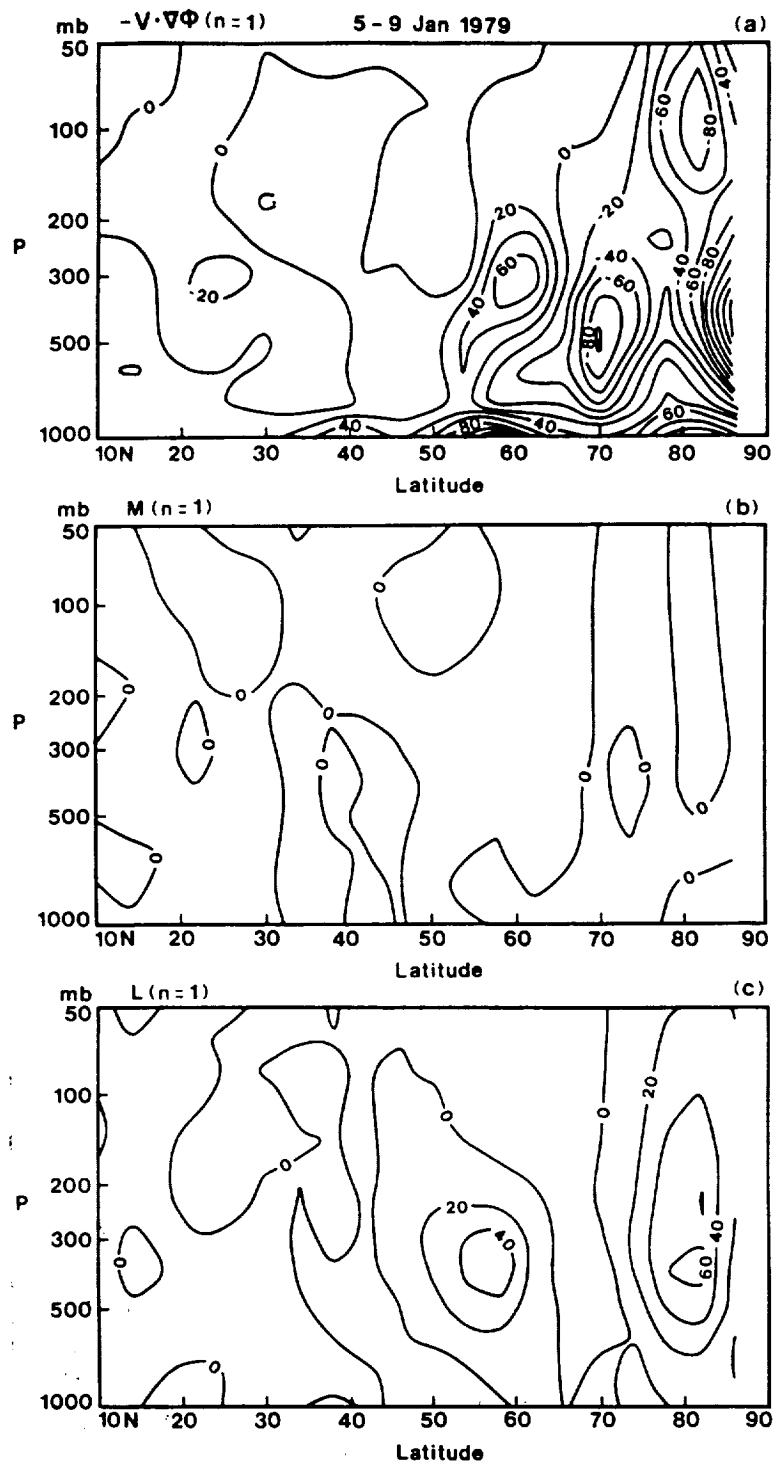


FIG. 10. As in Fig. 9, but for the kinetic energy production  $-V \cdot \nabla \phi$ , wave-mean interaction  $M$ , and wave-wave interaction  $L$  for  $n = 1$ . The values are observed 5-day means for 5-9 January 1979, multiplied by  $\rho_0$ , and expressed in the units of  $10^{-3} \text{ W m}^{-3}$ .

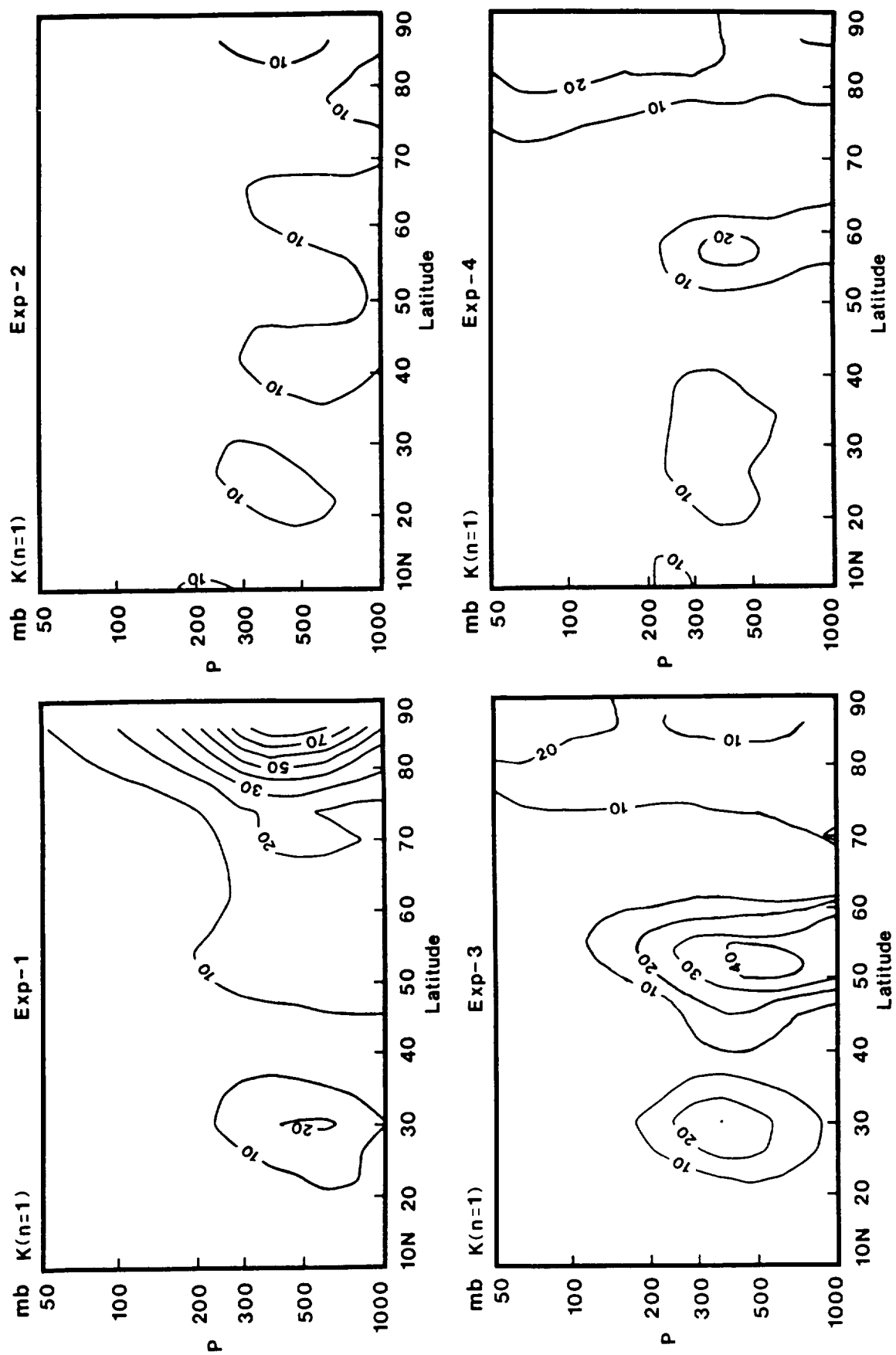


FIG. 11. Meridional-height cross sections of kinetic energy for four simulations during 7–11 January 1987 for  $n = 1$  in units of  $J m^{-3}$ .

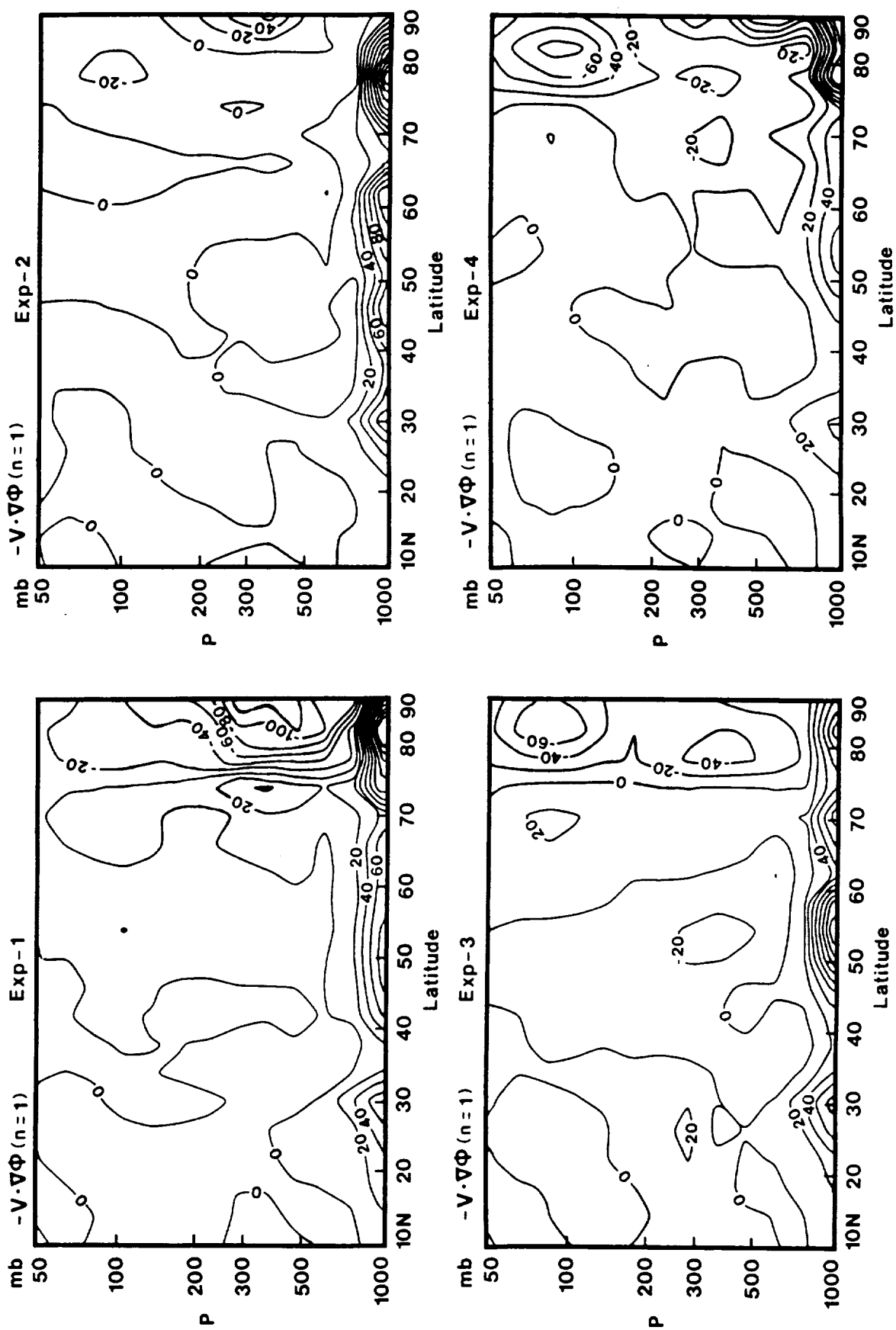


FIG. 12. As in Fig. 11, but for the kinetic energy production in units of  $10^{-5} \text{ W m}^{-3}$ .



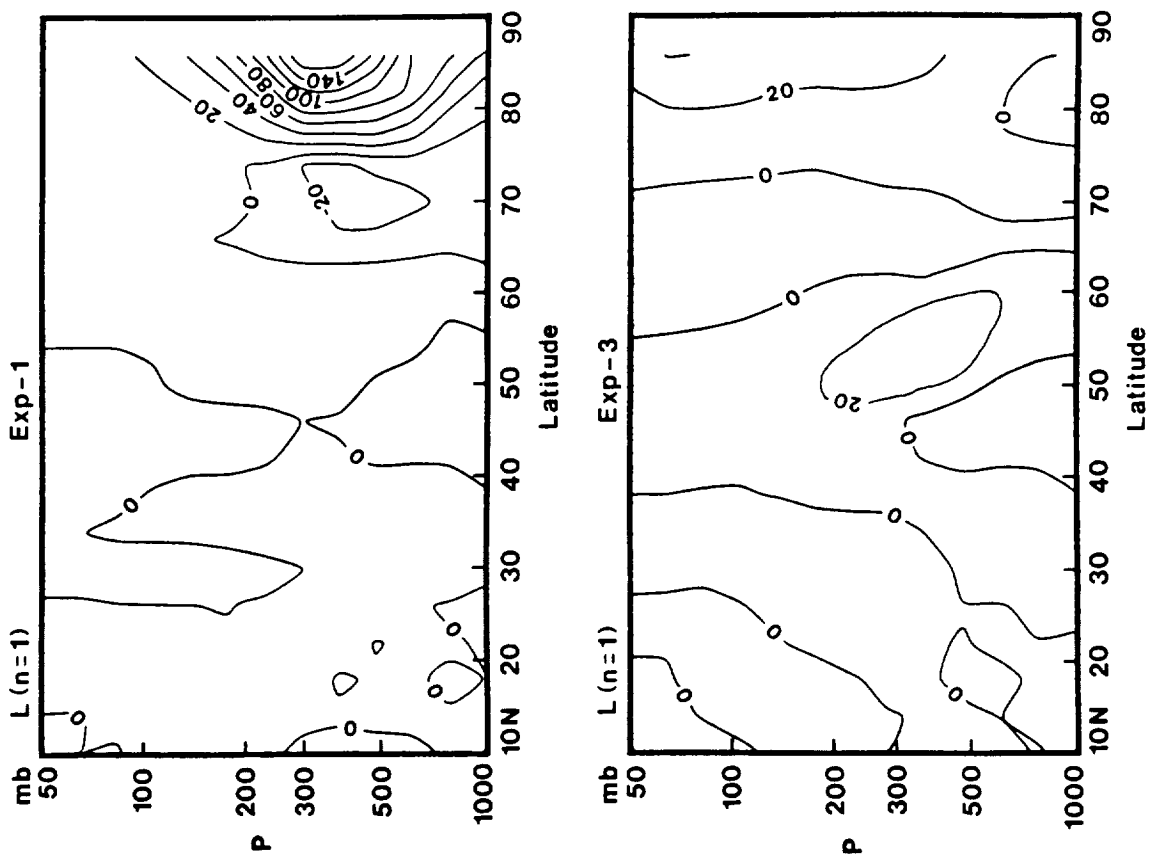


FIG. 13. As in Fig. 12, but for the wave-wave interaction.

4, which is also a simulation with the high resolution GCM, a weaker dipole of  $K(1)$  than Expt. 3 is noted, but the pattern of existing dipole is clearer than Expts. 1 and 2 of the coarse grid GCM simulations. As is seen in Fig. 12, the distributions of  $-V \cdot \nabla \Phi$  for  $n = 1$  in the simulations show the concentrated production of kinetic energy in the lower boundary of latitudes where  $K(1)$  is large. However,  $-V \cdot \nabla \Phi$  in the upper troposphere is weak and the distribution is erroneous, reflecting the weak ageostrophic component of circulation in the simulation due to time integration by the Matsuno scheme (see Daley et al. 1985). The distributions of  $L(1)$  of the simulations in Fig. 13 indicate  $L(1)$  is generally much weaker than in the observation

in Fig. 10. What are shown in cross sections of the simulations are consistent with the circulation patterns and spectral energy budgets (Table 3) in indicating that the high resolution of the model is needed to produce the proper wave-wave interaction to provide kinetic energy input at  $n = 1$ .

## 6. Barotropic-baroclinic conversions of energy

Temporal variations of barotropic ( $m = 0$ ) and baroclinic ( $m = 3-10$ ) energies in the zonal mean motion ( $n = 0$ ), ultralong waves ( $n = 1-2$ ) and synoptic waves ( $n = 3-15$ ) over the Northern Hemisphere are illustrated in Fig. 14 after Tanaka and Kung (1988).

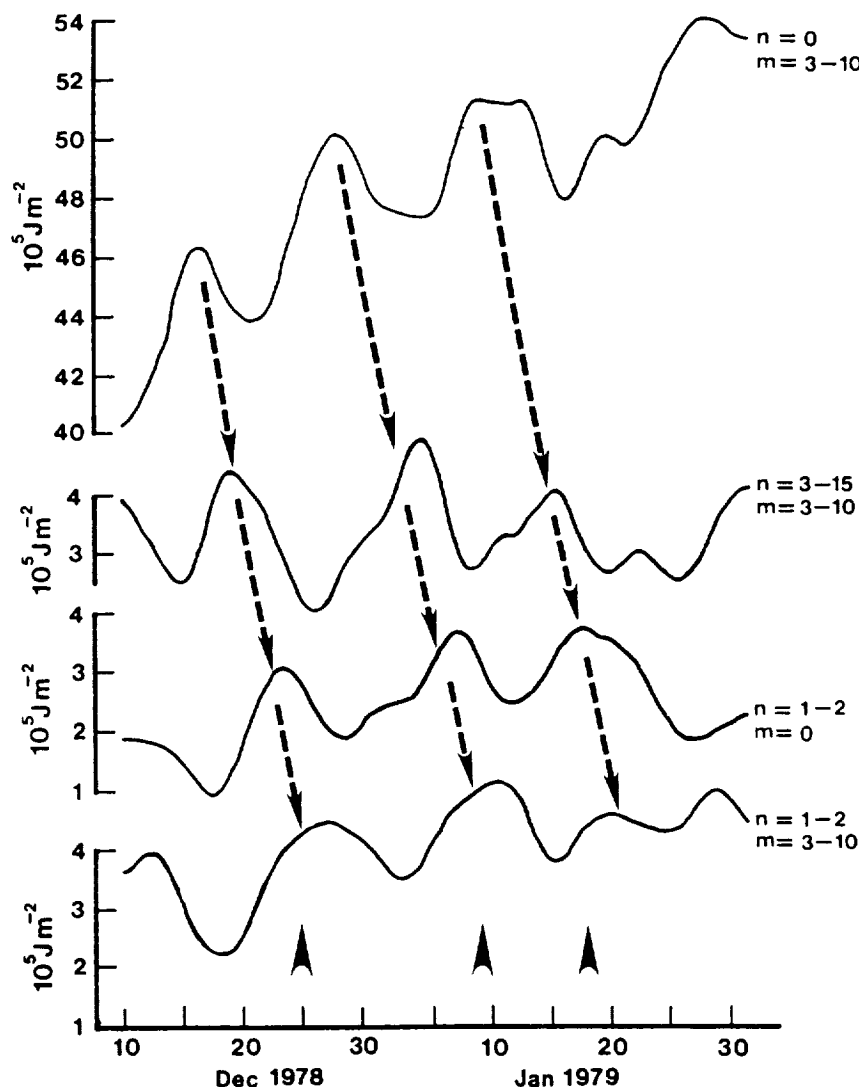


FIG. 14. Time series of barotropic ( $m = 0$ ) and baroclinic ( $m = 3-10$ ) energies for zonal mean motion ( $n = 0$ ), ultralong waves ( $n = 1-2$ ), and synoptic waves ( $n = 3-15$ ) over the Northern Hemisphere from 10 December 1978 through 31 January 1979 after Tanaka and Kung (1988). Appearance for typical Rex blockings are marked by arrows over the time axis.

The time variation of the zonal baroclinic energy ( $n = 0$ ,  $m = 3-10$ ) indicates clear energy peaks at 16 and 28 December and 9 January superimposed on the seasonal trend. There are subsequent increases of baroclinic energy of synoptic waves in the time series ( $n = 3-15$ ,  $m = 3-10$ ) through a process of baroclinic instability. The time lag is about 5 days. The time variation of synoptic-scale barotropic energy ( $n = 3-15$ ,  $m = 0$ ) is not shown in the figure but it is almost in phase with the baroclinic energy. The barotropic energy of ultralong waves ( $n = 1-2$ ,  $m = 0$ ) increases three days later through the wave-wave interaction of kinetic energy, the process required for amplification of ultralong waves to form the blocking. The peaks of ( $n = 1-2$ ,  $m = 0$ ) are identified with the most intensified pattern of blockings as marked in the figure. After the full development of the blocking (i.e., after reaching the mature stage of the blocking), the baroclinic energy of ultralong waves peaks.

The orderly transfer of energy from the zonal baroclinic component to the barotropic component of ultralong waves in the normal mode expansion may be identified with processes observed in the standard zonal wavenumber domain. The zonal available potential energy is transferred into the synoptic-scale disturbances, converted to kinetic energy and then used to build up the barotropic energy of blocking in the ultralong waves during the blocking development. Based on time mean spectral energetics (Table 3), it is seen that synoptic-scale waves support the energy of planetary waves by means of wave-wave interaction. The time series in Fig. 14 further reveals evidence of the upscale energy cascade from synoptic-scale waves to planetary waves. The upscale energy cascade occurs when the energy supply is in a phase conducive to amplification of planetary waves. Also, as shown in Kung and Baker (1986), under the developed blocking situation the meridional heat transport increases dramatically, and this apparently leads to the peak of the baroclinic energy of ultralong waves in the mature blocking stage.

This orderly transfer of energy is not well simulated in the numerical experiments, as shown in Fig. 15. In simulations it is possible to follow the energy flow from the baroclinic component of the zonal motion to the baroclinic and barotropic components of the synoptic-scale waves. However, the buildup of the barotropic energy in the ultralong waves at the time of blocking development is difficult to follow in all simulations. This is consistent with the fact that in simulations, enough kinetic energy is available at the synoptic-scale range through baroclinic conversion, but the model tends to fail to provide adequate energy input at ultralong waves through the wave-wave interaction.

Despite the disturbed time series of energy components in simulations (Fig. 15), the parallel time series of the nonlinear interactions  $A$  and  $B$  in Fig. 16 indicate traceable transformations from the zonal baroclinic

energy to the barotropic energy of ultralong waves. Around 5 and 25 January in Expt. 3,  $\beta$  shows its maxima for ( $n = 1-2$ ,  $m = 0$ ), and as seen in Fig. 3 and Table 1, these are the periods when Expt. 3 generated the blockings. The first blocking is a reasonable simulation of the observed blocking, but the second blocking is dislocated in its longitudinal position. It may be noted, however, that Expt. 3 is the only simulation able to generate a second blocking after the first one. Expt. 2 also indicates a traceable energy transformation toward the barotropic energy of ultralong waves ( $n = 1$  and 2). However, as seen from Table 3 the kinetic energy gain is mostly in  $L(2)$  rather than  $L(1)$ .

As stated in Eq. (3) the effects of nonlinear interactions,  $A$  and  $B$ , are balanced with the diabatic process  $F$ . For the barotropic component of ultralong waves, the largest portion of this process is expected to be the dissipation. Since  $F$  is obtained as the residual term of Eq. (3), the dissipation is actually the energy sink or cascade from ( $n = 1-2$ ,  $m = 0$ ). The time series of energy components in Fig. 14 appear more disturbed than expected from time series of transformations in Fig. 15. It may indicate that, in addition to the weaker nonlinear wave-wave interaction at ultralong waves, the energy cascade process as implied by  $F$  may be an additional problem in the numerical simulation of blocking, even with the high resolution model.

## 7. Concluding remarks

This study of Northern Hemisphere winter blocking episodes reveals considerable energetics differences between the simulations and the observation, and among simulations. In the simulations enough kinetic energy is available at the synoptic-scale range through the baroclinic conversion, but the models provide insufficient kinetic energy input from this source to  $n = 1$  through the wave-wave interaction  $L(1)$ . The failure in simulating realistic blocking due to inadequate  $L(1)$  can be attributed in part to inadequate grid resolution. The  $4^\circ \times 5^\circ$  coarse resolution of the model results in a downscale energy cascade preventing a proper upscale input at  $n = 1$ .

Among the four simulations examined in this study, Expts. 3 and 4 by the high resolutions GCM data tended to generate realistically strong blockings with compatible energetics as in the observed blocking episode. It is also noted that Expt. 3 with the GLA initial data was able to amplify  $n = 1$  to produce the second blocking during late January 1979 following the first one, although there was an obvious longitudinal dislocation of the second blocking.

The latitude-height cross sections of energy variables confirm that the dipole structure of the observed blocking is clearly described by  $n = 1$ , and further  $L(1)$  maxima are located at the kinetic energy maxima of the dipole. However, in all simulations, such a dipole structure of energetics is either weak or nearly absent.

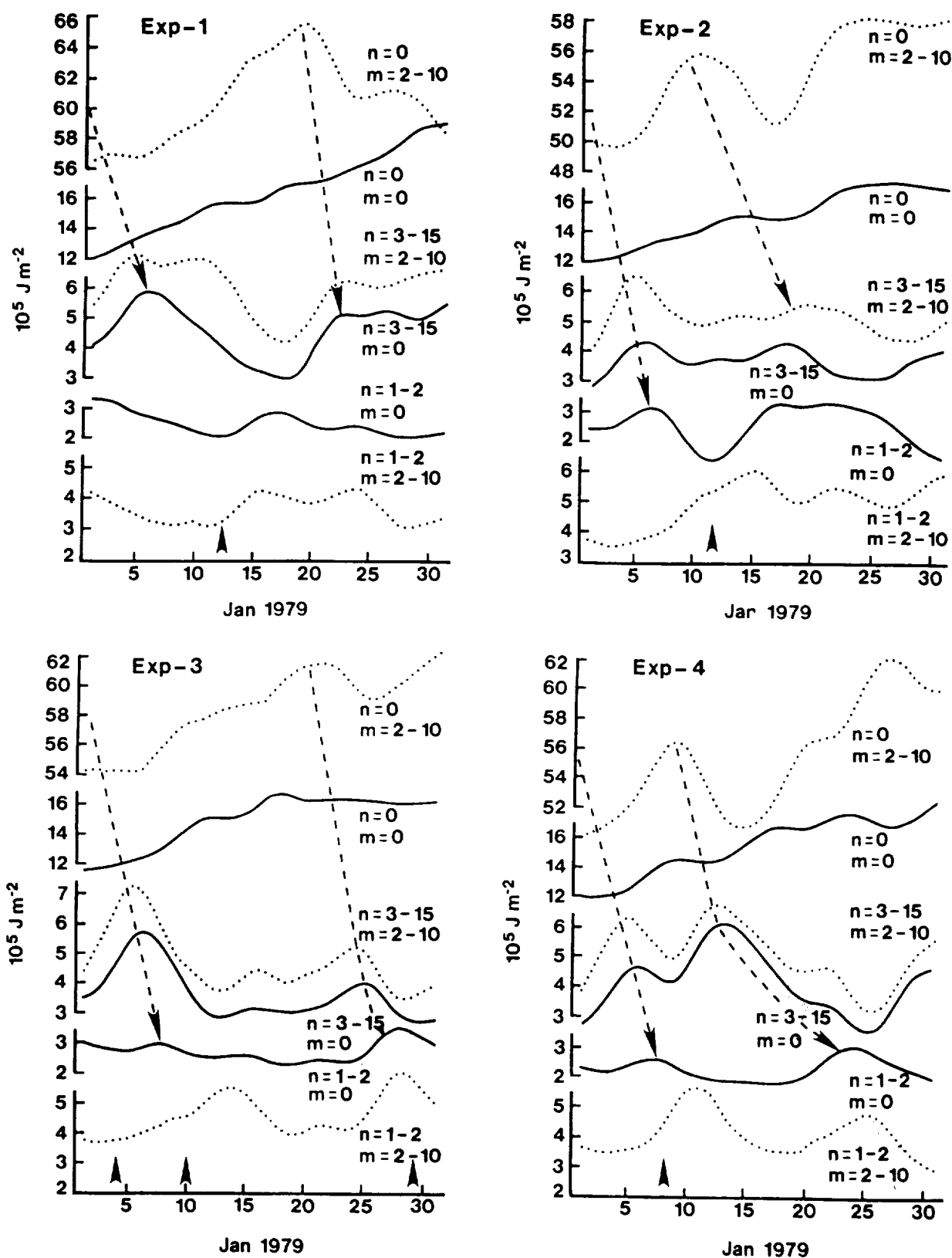


FIG. 15. As in Fig. 14, but for the four simulations. Baroclinic energy is the sum of baroclinic indices  $m = 2-10$ .

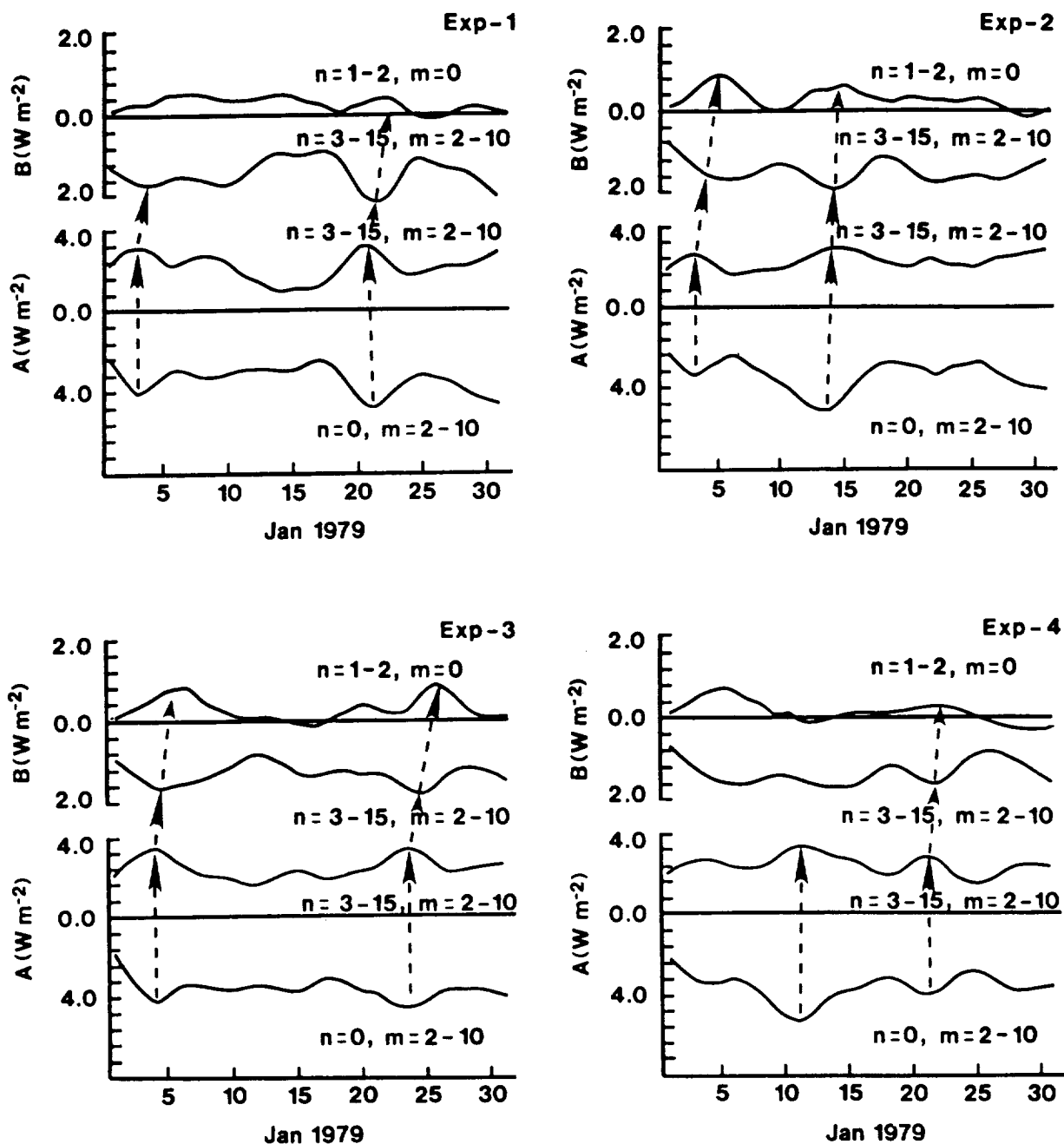


FIG. 16. Time series of kinetic energy interaction  $B$  and available potential energy interaction  $A$  for four simulations for the corresponding energy terms in Fig. 14.

Energetics of blocking development is further examined in a time series of barotropic and baroclinic components of energy and associated conversions. In the observed circulation an orderly transfer of energy is recognized from the zonal baroclinic component to the barotropic component of ultralong waves via synoptic-scale conversions. In the simulations, however, this orderly transfer of energy is not well simulated. The buildup of barotropic energy in ultralong waves

at the time of blocking development is either too weak or unrecognizable. This is consistent with the trend of the model failing to provide an adequate energy input at ultralong waves through the wave-wave interaction.

*Acknowledgments.* The authors gratefully acknowledge the courtesy of Drs. K. Miyakoda and J. J. Plushay of the Geophysical Fluid Dynamics Laboratory in providing the GFDL initial data, and the assistance of Y.

Brin and L. Takacs in the numerical experiments at the Goddard Space Flight Center. C. Da Camara of the University of Missouri—Columbia, provided valuable assistance in blocking identification. The authors are indebted to the anonymous reviewers, whose comments have led to a marked improvement of the paper. The authors are also thankful to S. Humphrey, G. Vickers, and D. Williams for their technical assistance. This research was performed at ECK Research Consulting Inc. under the National Aeronautics and Space Administration Contract NAS5-30128.

## REFERENCES

- Baker, W. E., 1983: Objective analysis and assimilation of observational data from FGGE. *Mon. Wea. Rev.*, **111**, 328–342.
- , and Y. Brin, 1985: A comparison of observed and forecast energetics over North America. *Quart. J. Roy. Meteor. Soc.*, **111**, 641–663.
- Bengtsson, L., 1981: Numerical prediction of atmospheric blocking—a case study. *Tellus*, **33**, 19–42.
- Dalcher, A., and E. Kalnay, 1987: Error growth and predictability in operational ECMWF forecast. *Tellus*, **39A**, 474–491.
- Daley, R., A. Hollingworth, J. Ploshay, K. Miyakoda, W. Baker, E. Kalnay, D. Dey, T. Krishnamurti and E. Barker, 1985: Objective analysis and assimilation techniques used for the production of FGGE IIb analysis. *Bull. Amer. Meteor. Soc.*, **77**, 532–540.
- Hansen, A. R., and A. Sutera, 1984: A comparison of the spectral energy and enstrophy budgets of blocking versus nonblocking periods. *Tellus*, **36A**, 52–63.
- Hollaway, G., and B. J. West, Eds., 1984: *Predictability of Fluid Motions*. American Institute of Physics, 612 pp.
- Holopainen, E., and C. Fortelius, 1987: High-frequency transient eddies and blocking. *J. Atmos. Sci.*, **44**, 1632–1645.
- Kalnay, E., R. Balgovind, W. Chao, D. Edelmann, J. Phaendner, L. Takacs and K. Takano, 1983: Documentation of the GLAS fourth order general circulation model. NASA Tech. Memo 86064. [NTIS N8424028.]
- Kalnay-Rivas, E., A. Bayliss and J. Storch, 1977: The fourth order GISS model of the global atmosphere. *Beitr. Phys. Atmos.*, **50**, 299–311.
- Kung, E. C., 1988: Spectral energetics of the general circulation and time spectra of transient waves during the FGGE year. *J. Climate*, **1**, 5–19.
- , and W. E. Baker, 1986: Spectral energetics of the observed and simulated Northern Hemisphere general circulation during blocking periods. *J. Atmos. Sci.*, **43**, 2792–2812.
- Lejenäs, H., and H. Økland, 1983: Characteristics of Northern Hemisphere blocking as determined from a long time series of observational data. *Tellus*, **35A**, 350–362.
- Matsuno, T., 1970: Vertical propagation of stationary planetary waves in the Northern Hemisphere. *J. Atmos. Sci.*, **27**, 871–883.
- Miyakoda, K., T. Gordon, R. Caverly, W. Stern and J. Sirutis, 1983: Simulation of blocking event in January 1977. *Mon. Wea. Rev.*, **111**, 846–869.
- Saltzman, B., 1957: Equation governing the energetics of the larger scales of atmospheric turbulence in the domain of wavenumber. *J. Meteor.*, **14**, 513–523.
- , 1959: On the maintenance of the large-scale quasi-permanent disturbances in the atmosphere. *Tellus*, **11**, 425–431.
- , 1970: Large-scale atmospheric energetics in the wavenumber domain. *Rev. Geophys. Space Phys.*, **8**, 289–302.
- Shapiro, R., 1970: Smoothing, filtering, and boundary effects. *Rev. Geophys. Space Phys.*, **8**, 359–387.
- Shukla, J., 1981: Dynamical predictability of monthly means. *J. Atmos. Sci.*, **38**, 2547–2572.
- Tanaka, H., 1985: Global energetics analysis by expansion into three-dimensional normal mode functions during the FGGE winter. *J. Meteor. Soc. Japan*, **63**, 180–200.
- , and E. C. Kung, 1988: Normal mode energetic of the general circulation during the FGGE year. *J. Atmos. Sci.*, **45**, 3723–3736.

4.2 Normal mode energetic and error analysis of  
GLA GCM simulations with the different horizontal  
resolutions during a winter month

H.L.Tanaka, E.C.Kung and W.E. Baker

## Normal Mode Energetics and Error Analysis of GLA GCM Simulations with Different Horizontal Resolutions during a Winter Month

H. L. Tanaka<sup>1,2</sup>, E. C. Kung<sup>1</sup> and W. E. Baker<sup>3</sup>

<sup>1</sup>Department of Atmospheric Science, University of Missouri-Columbia, Columbia, MO 65211, USA

<sup>2</sup>Current affiliation: Geophysical Institute, University of Alaska-Fairbanks Fairbanks, AK 99775, USA

<sup>3</sup>Development Division, National Meteorological Center, Washington, DC 20233, USA

(Manuscript received August 1988, in revised form February 1989)

### Abstract

Comparative energetics is presented for a series of four general circulation model simulations for January 1979 conducted by the Goddard Laboratory for Atmospheres. The simulations include cases of coarse and fine horizontal model resolutions with two slightly different initial conditions. Using a three-dimensional normal mode expansion, we find that the gravity mode energy levels are significantly reduced in the higher wavenumbers and in the higher order internal vertical modes by the increase of horizontal model resolution. The prediction error of the model experiments is measured by an error norm between the two spectral expansion coefficients of the observed and simulated atmospheres. The increase of the model resolution is found to reduce the prediction error in the planetary waves ( $n = 1$  and  $2$ ) of the barotropic component and in the synoptic waves of the baroclinic component. It is also found that the common bias in the predictions of the first internal vertical component of wavenumber 1 is related to the misrepresentation of the Pacific blocking occurring at the predictability limit of the model atmosphere.

### Zusammenfassung

**Energetik der Normalschwingungen und Fehleranalyse der GLA GCM Simulationen eines Wintermonats mit unterschiedlicher horizontaler Auflösung**

Eine vom Goddard Laboratory for Atmospheres durchgeführte vergleichende Energiestudie einer Reihe von vier Januarsimulationen des Jahres 1979 mit Modellen der allgemeinen Zirkulation wird vorgestellt. Die Simulationen umfassen Fälle grober und feiner horizontaler Auflösung unter zwei geringfügig verschiedenen Anfangsbedingungen. Durch Entwicklung nach dreidimensionalen Normalschwingungen finden wir, bei Vergrößerung der horizontalen Modellauflösung, daß die Schwerwellenenergie für die höheren Wellenzahlen und für die internen vertikalen Schwingungen höherer Ordnung bedeutend kleiner wird. Der Vorhersagefehler der Modellversuche wird durch eine Fehlernorm zwischen den beiden spektralen Entwicklungskoeffizienten der beobachteten und der nachgebildeten Atmosphäre gemessen. Es stellt sich heraus, daß die Erhöhung der Modellauflösung den Vorhersagefehler in den planetaren Wellen ( $n = 1$  und  $2$ ) der barotropen Komponente und in den synoptischen Wellen der baroklinen Komponente verringert. Ebenfalls zeigt sich, daß der systematische Fehler in den Vorhersagen der ersten vertikalen Komponente der Wellenzahl 1 mit der verzerrten Darstellung des an der Vorhersagbarkeitsgrenze der Modellatmosphäre auftretenden 'Pazifik-Blockings' zusammenhängt.

## 1 Introduction

One of the primary objectives of the First GARP (Global Atmospheric Research Program) Global Experiment (FGGE) was to improve extended-range weather prediction models. Through the analysis of the FGGE observations and parallel simulations by the Goddard Laboratory for Atmospheres (GLA) general circulation model (GCM), Kung and Baker (1986a) have shown that the energy processes in the short-wave range of the simulations are much more intense

than those in the observations for the FGGE winter. This is caused by the gain of kinetic energy in the short-wave range from the source of the synoptic-scale range through the nonlinear wave-wave interaction. The failure of the simulation to amplify ultra-long waves and produce a pronounced blocking is attributed to the lack of kinetic energy input by the wave-wave interaction to ultralong waves because of the excessive down-scale cascade. By means of a three-dimensional normal mode decomposition of atmospheric energetics variables, Tanaka et al. (1986)



have shown that the above-mentioned kinetic energy transformation is accompanied by the energy flow from baroclinic to barotropic components of atmospheric motion. The normal mode energetics have a specific advantage in separating energetics characteristics into Rossby and gravity modes. Tanaka et al. have reported a large reduction of high frequency gravity mode in the simulated atmosphere compared to the FGGE observation.

Based on the analysis results, four numerical simulations of January 1979 are conducted to investigate the energetics effects of grid resolutions and initial datasets. The four simulations include those of two different grid resolutions, each with two different initial datasets. Both the standard  $4^\circ \times 5^\circ$  latitude-longitude GLA GCM and fine resolution  $2^\circ \times 2.5^\circ$  GLA GCM are integrated for a one-month period using the 0000 GMT 1 January 1979 initial datasets during the FGGE as analyzed by the GLA and the Geophysical Fluid Dynamics Laboratory (GFDL).

The computational effects of increased horizontal resolution were extensively investigated by many researchers (e.g., Manabe et al., 1970; Welck et al., 1971; Miyakoda et al., 1971; Puri and Bourke, 1974). Manabe et al. (1970) compared the results of coarse (about 500 km grid size) and fine (about 250 km) resolution models and showed that the spectral distribution of eddy kinetic energy becomes closer to that of the observed atmosphere in the fine resolution model partly due to the shift of energy dissipation toward a smaller scale. Welck et al. (1971) compared the simulated energy spectra for  $10^\circ$ ,  $5^\circ$ , and  $2.5^\circ$  grid models in longitude and latitude to show a noticeable improvement of the long wave spectrum at wavenumbers 1 to 4 in the  $2.5^\circ$  grid model. Puri and Bourke (1974) investigated the effect of a truncation on energy and enstrophy spectra in barotropic spectral models and showed that the unrealistic energy accumulation at short waves in a coarse resolution model is released in a fine resolution model. The increase in the model resolution resulted in a reduction in short wave energy.

The effect of slightly different initial data on predictive skill was documented by Charney et al. (1986), Smagorinsky (1969), Williamson and Kasahara (1971), and Lorenz (1982) in the context of atmospheric predictability. Unavoidable initial error grows rapidly as the time integration proceeds. The predictions by the identical twin models, starting from the slightly different initial data, level off with each other to indicate that the deterministic atmospheric predictability is of the order of two weeks. The error growth is induced essentially by a nonlinear cascade of error energy from small to large scales. Yee and Shapiro (1981) and

Straus (1988), on the other hand, proposed that numerical errors can be amplified as a part of the dynamics of a physically unstable system in the atmosphere. Recently, Miyakoda et al. (1986) conducted a series of one-month forecasts using three different initial conditions. They showed that the circulation patterns starting from these three initial conditions tend to be similar to each other on a one-month time scale, indicating some recognizable skill in the last ten days of the month. They suggested that extended-range forecast errors are largely due to the systematic bias which is known as climatic drift. Their study indicates a possibility of extended-range forecasting by investigating the mechanism of error growth of our dynamical-statistical forecasting models.

The effect of the increased horizontal resolution and the effect of the different initial conditions upon the climatic drift are examined in this study using a recently developed normal mode energetics scheme (see Tanaka, 1985; Tanaka et al., 1986; Tanaka and Kung, 1988). The scheme allows the diagnosis of not only the three-dimensional spectral distributions of energy and energy transformations but also the examination of the energetics characteristics of Rossby waves, gravity waves, barotropic components, and baroclinic components of the atmospheric general circulation. Prediction errors in previous studies have been assessed using conventional specific fields such as the root-mean-square error of 500 mb height or sea-level pressure (e.g., Shukla, 1985). In the normal mode expansion method, it is possible to evaluate the prediction errors for barotropic and baroclinic components or Rossby and gravity modes, using global atmospheric data. The examination of error energy spectra of predictions in terms of the normal mode expansion should provide meaningful information in order to improve the forecasting skill of the model. The characteristics of error energy spectra are presented in the present study for the wavenumber and vertical index domain with a barotropic-baroclinic decomposition.

## 2 Simulation Experiments and Datasets

As listed in Table 1, four simulation experiments (Exps-1, 2, 3 and 4) were conducted for the period 1–31 January 1979 with the GLA standard and high resolution GCMs. The GLA and GFDL gridded analyses of the FGGE at 0000 GMT 1 January were used as the initial data (see Daley et al., 1985; Kung and Baker, 1986a). The mean January climatology of the sea surface temperature was used in all four simulations.

The standard coarse resolution version of the GLA GCM used in the simulation is the fourth-order global

**Table 1** Four simulation experiments of the January 1979 global atmosphere with GLA GCMs

Experiment	1/1/79 0000 GMT (initial data)	GCM grid size (latitude × longitude)
Exp-1	GLA	4° × 5°
Exp-2	GFDL	4° × 5°
Exp-3	GLA	2° × 2.5°
Exp-4	GFDL	2° × 2.5°

atmospheric model described by Kalnay-Rivas et al. (1977) and Kalnay et al. (1983). There are nine vertical layers equal in sigma with a uniform nonstaggered horizontal grid of 4° latitude by 5° longitude. The model is based on an energy conserving scheme in which all horizontal differences are computed with fourth-order accuracy. A 16th-order Shapiro (1970) filter is applied every two hours on the sea-level pressure, potential temperature, and wind fields. In this scheme, wavelengths longer than four grid lengths are resolved accurately without damping. Wavelengths shorter than four grid lengths, which would otherwise be grossly misrepresented by the finite differences, are filtered out while they are still infinitesimal. The energy spectrum of high-frequency gravity modes is controlled by the Matsuno (Euler-backward) time integration scheme. Poleward of 60°N the time tendency of the full model fields are filtered for unstable zonal wavenumbers as determined by a Matsuno time scheme, the fourth order spatial differencing, and a 7.5 min time step (see Takacs and Balgovind, 1983).

The 2° latitude by 2.5° longitude high resolution version of the GLA GCM is identical to the coarse resolution version with respect to the physical parameterizations. The time step of the hydrodynamics is 3.75 minutes in the high resolution version compared to 7.5 minutes in the coarse resolution version. An 8th-order Shapiro (1970) filter is used rather than the 16th-order filter in coarse resolution model.

The four simulation datasets analyzed in this study include twice-daily grid-point values of geopotential height, temperature, humidity, horizontal wind and vertical velocity at 1000, 850, 700, 500, 400, 300, 250, 200, 150, 100, 70, and 50 mb at 0000 and 1200 GMT. The FGGE analysis data by the GFDL are utilized in this study to represent the observed atmosphere for evaluating the prediction errors in the simulations.

### 3 Scheme of Analysis

The analysis scheme of normal mode energetics is based on Tanaka (1985) and Tanaka and Kung (1988).

Total energy  $E = K + P$  (the sum of kinetic energy and available potential energy) for a component of three-dimensional normal mode expansion may be written as

$$E_{nlm} = \frac{1}{2} p_s h_m |w_{nlm}|^2, \quad (1)$$

where  $w_{nlm}$  is a dimensionless complex expansion coefficient of dependent variables  $u, v, \phi$ . The dimensional factors of surface pressure of the basic state  $p_s$  and equivalent height  $h_m$  are multiplied to  $|w_{nlm}|^2$  so that the energy is expressed in units of  $Jm^{-2}$ . The triple subscripts are the wavenumber  $n$ , meridional index  $l$ , and vertical index  $m$ , respectively.

The vertical modes  $m = 0$  and  $m \neq 0$  are regarded respectively as the barotropic (external) and baroclinic (internal) modes. Figure 1 illustrates the first six vertical structure functions as the expansion basis in the vertical (after Tanaka et al., 1986). Total energy pertaining to  $m = 0$  is defined as barotropic energy and that for  $m \neq 0$  baroclinic energy. There are 12 vertical analysis levels to generate the vertical modes of  $m = 0-11$ . A construction of vertical structure functions for very small equivalent height, particularly for  $m = 11$ , is extremely difficult and contains a large extent of uncertainty. For this reason, the maximum vertical index utilized in this study is  $m = 10$ . Global atmospheric field of each vertical index is then projected onto orthonormal Hough functions which have been computed from Laplace's tidal equation for a motionless basic state. A total of 50 meridional indices are used, including 26 Rossby modes, and 12 eastward and 12 westward gravity modes. These meridional modes retrieve a sufficient amount of atmospheric energy of large scale motions as demonstrated in Tanaka (1985). The zonal wavenumbers  $n = 0-15$  are examined in this study. Unrealistic reduction of short waves was analyzed for the coarse resolution model output beyond  $n = 18$ . The reduction may be explained by the Shapiro filter which filters out the wavelengths shorter than 4 grid lengths (i.e., 20° longitude). The definition of energy in (1) involves a contribution from vertical geopotential flux across the lower boundary; however, this contribution is negligibly small.

The spectral energy balance equation for a component of normal mode expansion may be written as

$$\frac{dE_{nlm}}{dt} = B_{nlm} + C_{nlm} + D_{nlm}, \quad (2)$$

where  $B_{nlm}$  is the nonlinear interaction of kinetic energy,  $C_{nlm}$  that of available potential energy, and  $D_{nlm}$  the combined energy source and sink by the diabatic processes, including dissipation. The spectral

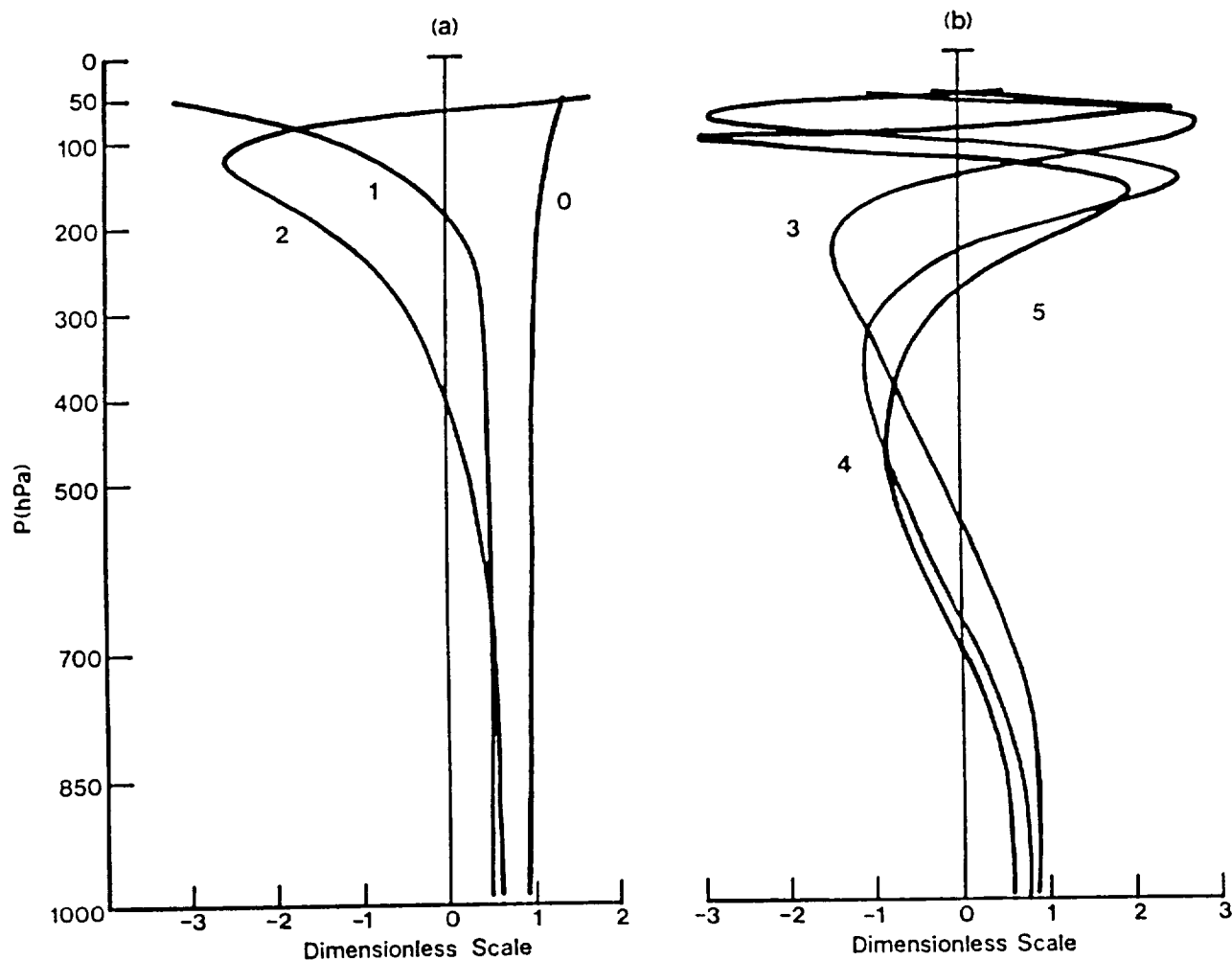


Figure 1 The first six vertical structure functions for the vertical indices  $m = 0-5$  (after Tanaka et al., 1986).

sums of  $B_{nlm}$  and  $C_{nlm}$  are zero because they represent the global integral of the flux convergence of kinetic energy and available potential energy. The nonlinear interaction of kinetic energy  $B$  is equivalent to a sum of wave-mean and wave-wave interactions of kinetic energy in the standard spectral energetics, and so is the nonlinear interaction of available energy  $C$  (see Saltzman, 1957; Kung and Tanaka, 1983). Surface wind at  $p = p_s$  has been assumed to vanish as set in Tanaka and Kung (1988).

Using the method of normal mode expansion, we can assess the forecast error in the simulated atmosphere by an error norm between the spectral expansion coefficients of observation  $w_{nlm}$  and simulation  $\hat{w}_{nlm}$ , where the hat designates variables for simulations. A similar evaluation of forecast error is seen using the error norm of spherical harmonic expansions coefficients at a certain vertical level (e.g., Boer, 1984). The

present error analysis is based on the information of whole atmospheric field. According to the definition of energy in (1), the error variance  $ERR$  in the simulation (actually the apparent error because the observed variables will involve observational errors) may be given as a sum of the following quantities of the normal mode expansion:

$$ERR_{nlm} = \frac{1}{2} p_s h_m |\hat{w}_{nlm} - w_{nlm}|^2. \quad (3)$$

The same dimensional factor with (1) is used so that the error variance has physical units of  $Jm^{-2}$ . It should be remarked that errors in amplitude and in phase are mixed together in this expression. By means of the inverse of the vertical and Fourier-Hough transforms, it may be shown that the sum of  $ERR_{nlm}$  has the same form as total energy  $E = K + P$ , in which the dependent variables  $u$ ,  $v$ , and  $\phi$  have been replaced by  $\hat{u} - u$ ,  $\hat{v} - v$ , and  $\hat{\phi} - \phi$ .

#### 4 Gross Energy Budget for Simulations

One-month average energy spectra and energy interactions are examined in this section. The spectral distributions of total energy  $E(n)$  for Rossby modes and gravity modes are illustrated in Figure 2 as functions of wavenumber  $n$  for the four simulations. The results of the four simulation experiments, Exp-1 through Exp-4, are distinguished in the figure by a combination of the dashed line ( $4^\circ \times 5^\circ$  coarse resolution model), solid line ( $2^\circ \times 2.5^\circ$  fine resolution model), black dot (GLA initial condition), and white circle (GFDL initial condition). The difference of energy spectra at higher wavenumbers between the coarse and fine resolution models is apparent. Both the Rossby modes and gravity modes indicate lower energy levels in the fine resolution models at higher wavenumbers. The gravity modes show a larger reduction than the Rossby modes.

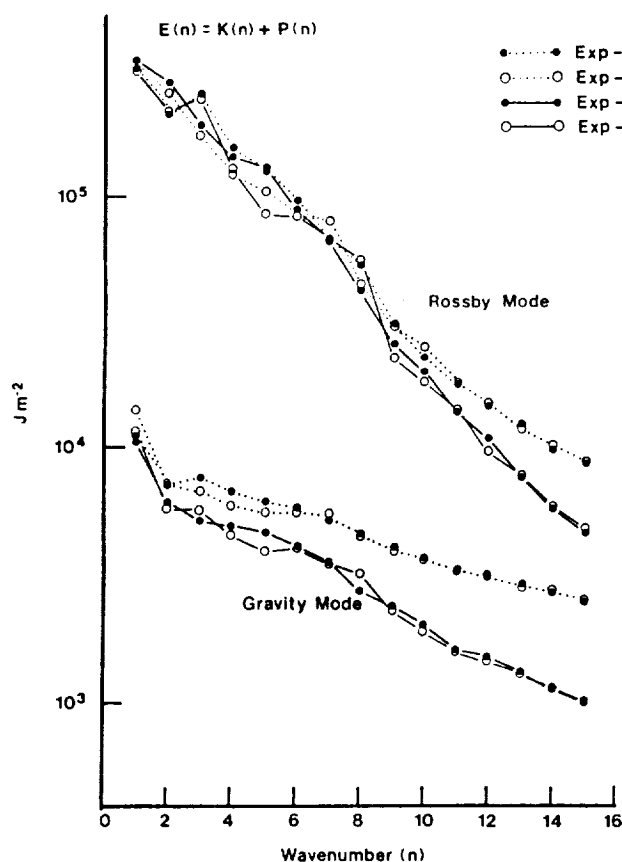


Figure 2 Monthly mean total energy spectra  $E(n) = K(n) + P(n)$  of Rossby modes and gravity modes in the zonal wavenumber domain for the four simulations. The simulations are distinguished by coarse (dashed line) and fine (solid line) model resolutions with a combination of GLA (black dot) and GFDL (white dot) initial datasets.

Figure 3 illustrates the total energy spectra  $E(m)$  of zonal eddy ( $n = 1-15$ ) for Rossby modes and gravity modes as functions of vertical indices  $m$ . The Rossby modes indicate bimodal energy peaks at the barotropic index  $m = 0$  and baroclinic index  $m = 3$ . The bimodal energy peaks were explained by Tanaka and Kung (1989) as the characteristics of atmospheric baroclinic instability for a January basic flow. The gravity modes show the largest energy levels at  $m = 2-3$ . Different energy levels between the coarse and fine resolution models at the higher vertical indices of gravity modes are apparent. The increase of horizontal resolution results in a reduction of gravity mode energy levels in the higher order vertical indices. Rossby modes have the same tendency of diminishing energy levels for the higher vertical indices. Vertical energy spectra are not influenced by the different initial conditions provided by the GLA and the GFDL.

It is well-known that the effect of an increased horizontal model resolution appears as an improved eddy energy spectrum. Manabe et al. (1970) found that the increase in the horizontal model resolution improves the general magnitude and the spectral distribution of eddy kinetic energy to be closer to those of the observation due not only to the increase in the accuracy of the

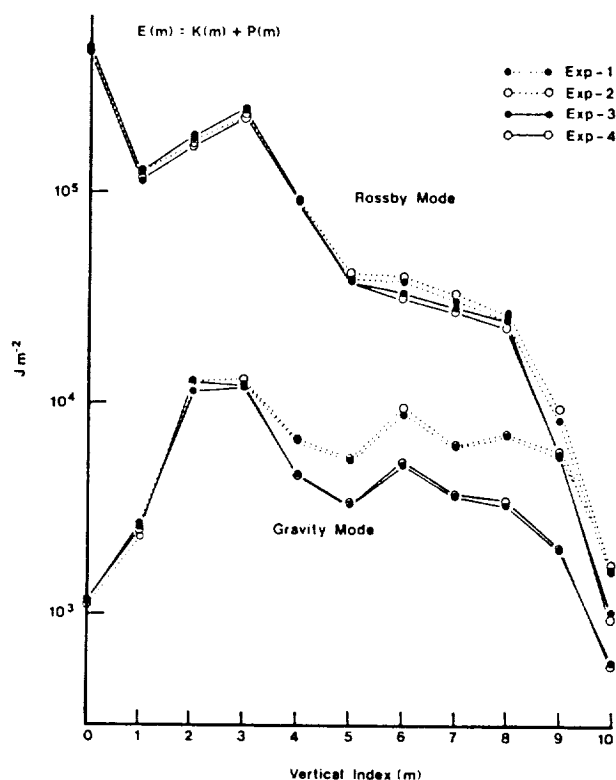


Figure 3 As in Figure 2, but in the vertical index domain  $m = 0-10$ .

differences but also to the shift in the scale of dissipation toward smaller scales. Welck et al. (1971) compared  $10^\circ$ ,  $5^\circ$ , and  $2.5^\circ$  mesh model simulations and showed an increase of kinetic energy at the planetary waves in the finer resolution model. Modified up-scale energy cascade from synoptic waves to planetary waves are discussed as the main reason for the improvement. Puri and Bourke (1974) showed an unrealistic accumulation of eddy energy at the shortest resolvable waves in a coarse resolution model. They demonstrated that the accumulation is released in a finer resolution model to reduce the short wave energy. The spectra with the GLA initial conditions and the GFDL initial conditions are indistinguishable. Miyakoda et al. (1986) showed that the circulation patterns of the models tend to be similar to each other on the one-month time scale for three stochastic predictions which start from observed initial conditions derived from three different meteorological centers. The results of their studies agree with the energetics analysis using the normal mode expansion.

The normal mode energetics are summarized in Table 2 in the barotropic ( $m = 0$ ) and baroclinic ( $m = 1-10$ ) decomposition of zonal ( $n = 0$ ) and eddy ( $n = 1-15$ ) components. The results for the FGGE observations

for the winter period from December to February after Tanaka and Kung (1988) are also listed. Compared to the observations, there is a consistent bias of larger zonal barotropic energy in all simulations. Zonal baroclinic energy is closer to the observations. The term B shows large negative values in the eddy baroclinic component ( $n = 1-15$ ,  $m = 1-10$ ) and positive values in the eddy barotropic ( $n = 1-15$ ,  $m = 0$ ) and zonal barotropic ( $n = 0$ ,  $m = 0$ ) components. This indicates kinetic energy transformations from eddy baroclinic to eddy and zonal barotropic components as the net during the period. It is noted that this kinetic energy interaction is significantly larger in simulations than in the observation corresponding to the larger available potential energy interaction C from the zonal baroclinic ( $n = 0$ ,  $m = 1-10$ ) to eddy baroclinic  $n = 1-15$ ,  $m = 1-10$ ) components. The model biases of large energy level in the zonal field and intense energy transformations were documented in Kung and Baker (1986a) and Tanaka et al. (1986). These deficiencies of the model are not improved by the increase of horizontal resolution and the use of different initial datasets. Kinetic energy supply into the zonal barotropic component ( $m = 0$ ,  $n = 0$ ) rather increases with the increase of horizontal resolution. The net diabatic

**Table 2** Monthly mean normal mode energy budget for the four simulations. Energy (K, P, and E) in units of  $10^5 \text{ Jm}^{-2}$  and energy transformations (B, C, D, and  $dE/dt$ ) in  $\text{Wm}^{-2}$  are listed for the zonal ( $n = 0$ ) and eddy ( $n = 1-15$ ) components in the barotropic ( $m = 0$ ) and baroclinic ( $m = 1-10$ ) decomposition. The same energy variables for the FGGE observations during three winter months are after Tanaka and Kung (1988)

n	m	K	P	E	B	C	D	dE/dt
Exp-1								
0	0	9.5	2.9	12.4	0.49	-0.26	0.00	0.23
0	1-10	4.2	46.7	50.9	-0.03	-2.37	2.42	0.02
1-15	0	5.0	0.3	5.3	0.41	0.16	-0.51	0.06
1-15	1-10	4.9	3.8	8.7	-1.72	2.30	-0.54	0.04
Exp-2								
0	0	8.6	2.6	11.2	0.46	-0.25	-0.07	0.14
0	1-10	3.6	42.8	46.3	0.00	-2.30	2.66	0.35
1-15	0	4.3	0.2	4.5	0.39	0.15	-0.49	0.04
1-15	1-10	4.9	3.8	8.7	-1.68	2.34	-0.52	0.13
Exp-3								
0	0	8.7	2.6	11.3	0.64	-0.28	-0.22	0.14
0	1-10	3.7	44.4	48.2	0.13	-2.52	2.59	0.20
1-15	0	4.9	0.3	5.1	0.51	0.17	-0.65	0.03
1-15	1-10	4.7	3.8	8.4	-1.43	2.42	-0.95	0.04
Exp-4								
0	0	9.0	2.7	11.7	0.73	-0.29	-0.23	0.20
0	1-10	3.7	43.3	47.0	0.15	-2.46	2.69	0.37
1-15	0	4.4	0.3	4.7	0.45	0.19	-0.58	0.06
1-15	1-10	4.3	3.5	7.8	-1.47	2.51	-0.98	0.06
FGGE								
0	0	6.5	1.9	8.4	0.47	-0.20	-0.27	0.00
0	1-10	4.1	44.2	48.3	-0.06	-1.85	1.97	0.06
1-15	0	3.6	0.2	3.8	0.33	0.10	-0.44	0.00
1-15	1-10	4.3	3.3	7.6	-0.82	1.63	-0.86	-0.04

process D of the zonal baroclinic component ( $n = 0$ ,  $m = 1-10$ ) is larger in the simulations than in the observations. It is also noted that the net diabatic sink D of the eddy baroclinic components ( $n = 1-15$ ,  $m = 1-10$ ) is larger in the fine resolution model than in the coarse resolution model.

## 5 Error Analysis

Error analysis can be used to measure the difference of a model property and that of the forecast skill for different simulations. In the normal mode energetics scheme, the prediction errors are evaluated using the global integrations of the atmospheric fields. We use

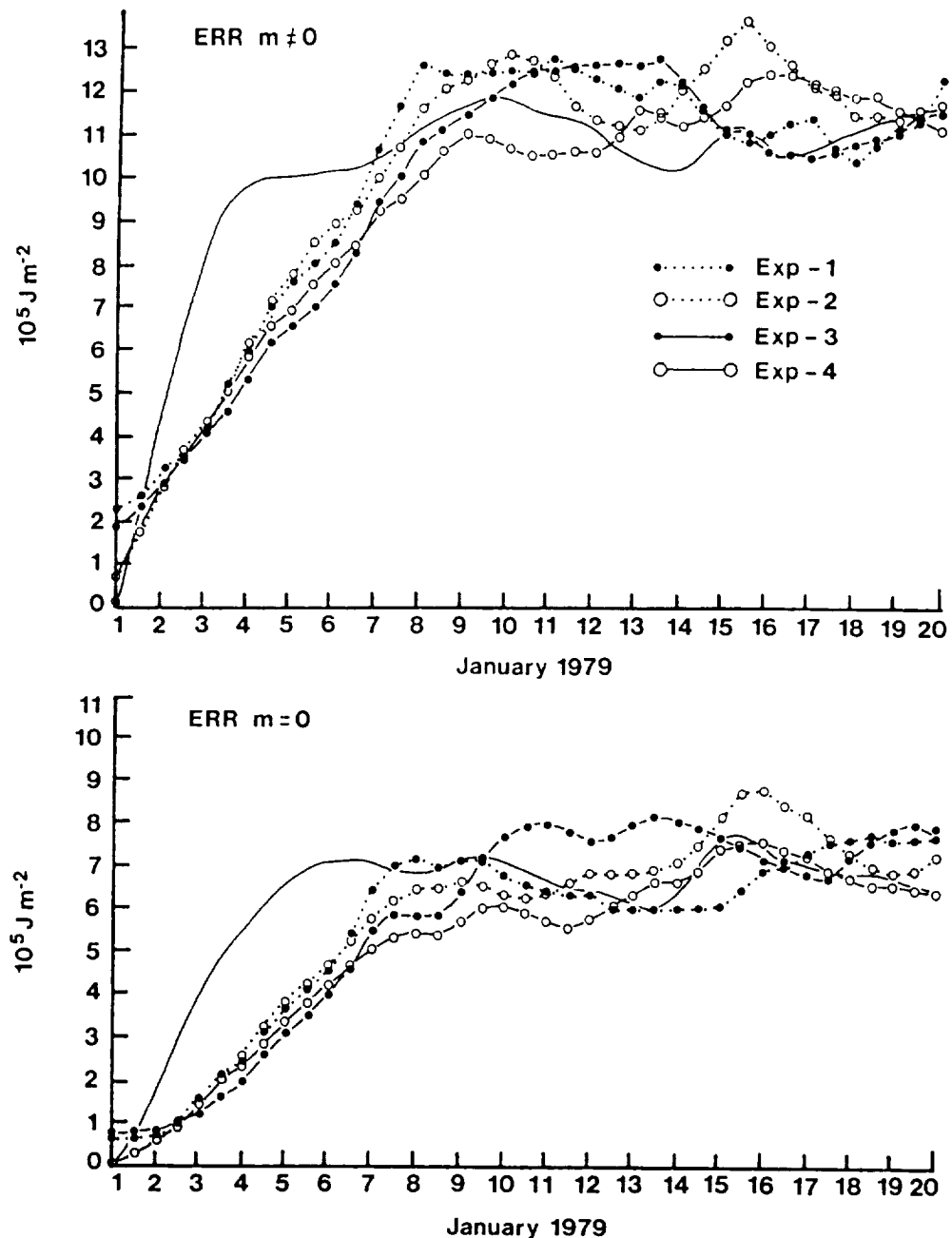


**Figure 4** Growth of prediction errors in the four simulations:  $ERR_{m \neq 0}$  is eddy baroclinic ( $n = 1-15$ ,  $m = 1-10$ ) components, and  $ERR_{m=0}$  eddy barotropic ( $n = 1-15$ ,  $m = 0$ ) components. The simulations are distinguished by coarse (dashed line) and fine (solid line) model resolutions with a combination of GLA (black dot) and GFDL (white dot) initial datasets. Persistence errors starting from 1 January 1979 are presented by a solid line without symbols.

the GFDL analysis of the FGGE data to represent the observed real atmosphere for evaluating the prediction error in model simulations. Although there are other versions of the FGGE analysis, the use of other analysis data should not alter our major conclusions.

Figure 4 illustrates the error growth in eddy field ( $n = 1-15$ ) of the simulations starting from the initial data of 0000 GMT 1 January. For comparison, the persistence error is presented starting from the same date. The persistence error reaches its saturation level on day 4 in the baroclinic component ( $m = 1-10$ ), and on day 6 in the barotropic component ( $m = 0$ ). In contrast, the error energies of the simulations reach their saturation levels around days 8 to 10 in both the barotropic ( $m = 0$ ) and baroclinic ( $m \neq 0$ ) components. Dalcher and Kalnay (1987) proposed the theoretical limit of dynamical predictability as a function of two-dimensional total wavenumber based on the time at which the error energy reaches 95% of the saturated value. The error growth in the eddy field is slightly reduced in the high resolution model (solid line) compared to the coarse resolution model (dotted line). The error energy for the GLA initial data (black dot) on day 1 is about 2 for the baroclinic components and 1 for the barotropic components with units of  $10^5 \text{ J m}^{-2}$  because of the different initialization techniques by the GLA and the GFDL. Supposing that these are the estimates of unavoidable initial error, these initial errors account for more than 10% of the saturation error energy.

According to Dalcher and Kalnay's (1987) criterion of the dynamical predictability, the error energy of the GLA model reaches 95% of the saturated value on about day 7. The error energy spectra in the wavenumber domain on day 7 are illustrated in Figure 5 for the barotropic and baroclinic components. The errors are the largest in the planetary waves for  $n = 1-2$  in the baroclinic components, and in the synoptic waves of  $n = 4-5$  for the barotropic components. In interpreting the error energy spectrum, the work of Lorenz (1982) indicates that nonlinear interactions in the system are very effective in amplifying the prediction error and thereby degrading predictability. Yee and Shapiro (1981) and Straus (1988) suggested that the physical instability should play a key role in the growth of mid-latitude forecast error. Straus showed that the synoptic scale (i.e.,  $n = 4-5$ ) peak in the error energy spectrum is due to baroclinic instability, whereas the planetary wave peak is due entirely to nonlinear interactions which transfer error energy from the synoptic scale to the planetary scale. The distinct error energy spectra in the barotropic and baroclinic components in this study may be related partly to the dynamics of the unstable system combined with the

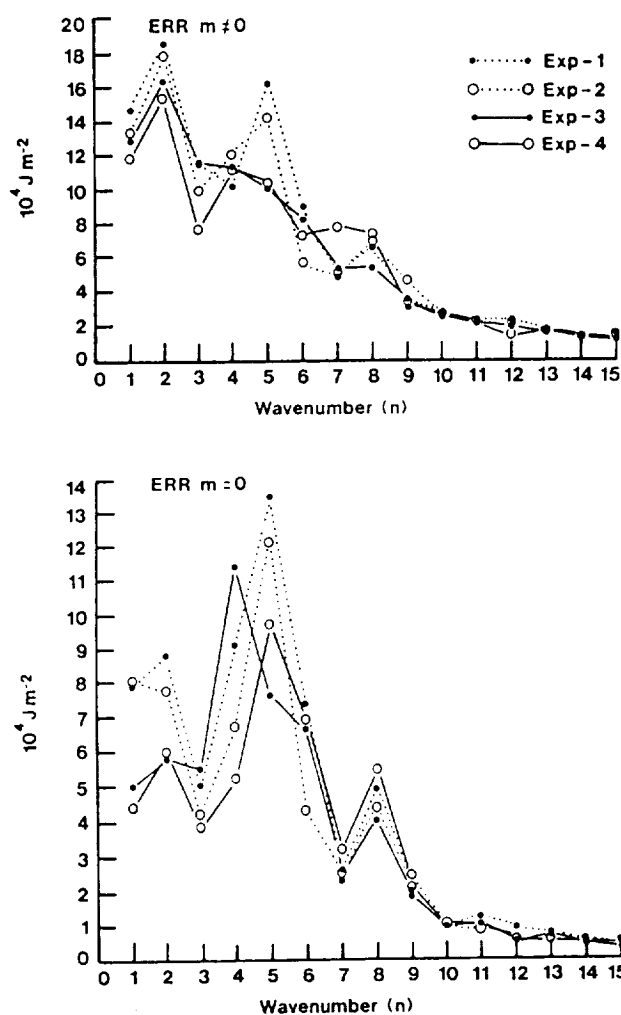


Figure 5 Error energy spectra of the four simulations on date 7:  $\text{ERR}_{m \neq 0}$  is baroclinic ( $m = 1-10$ ) components, and  $\text{ERR}_{m=0}$  barotropic ( $m = 0$ ) components.

nonlinear interaction. However, the separation of these two factors would be difficult. There is a clear difference in the error energy levels between the coarse and fine resolution models. Errors are significantly reduced by the increase of horizontal resolution in the planetary waves ( $n = 1$  and  $2$ ) for the barotropic components and in synoptic waves ( $n = 5$ ) for the baroclinic components.

Table 3 lists the error energy spectrum in the vertical index domain over  $n = 0-5$  for zonal wavenumbers  $n = 1-6$  and for the sum of eddies  $n = 1-15$  at day 7. The vertical error energy spectra for eddies  $n = 1-15$  show the largest values for the barotropic components ( $m = 0$ ) and the next largest in the baroclinic component ( $m = 3$ ). The magnitude of the error energy spectrum appears to be proportional to that of the

**Table 3** The error energy spectrum at day 7 in the vertical index domain  $m = 0-5$  for wavenumbers  $n = 1-6$  and the sum of the eddies  $n = 1-15$  in units of  $10^5 \text{ Jm}^{-2}$ 

m	n = 1	n = 2	n = 3	n = 4	n = 5	n = 6	n = 1-15
Exp-1							
0	0.79	0.88	0.50	0.91	1.35	0.74	6.54
1	0.34	0.22	0.22	0.13	0.18	0.07	1.49
2	0.22	0.31	0.30	0.13	0.31	0.17	1.81
3	0.31	0.64	0.34	0.35	0.62	0.33	3.29
4	0.22	0.35	0.17	0.16	0.23	0.14	1.60
5	0.11	0.14	0.07	0.07	0.08	0.05	0.72
Exp-2							
0	0.81	0.77	0.42	0.67	1.21	0.43	5.70
1	0.23	0.20	0.15	0.13	0.14	0.05	1.21
2	0.20	0.33	0.18	0.22	0.34	0.10	1.84
3	0.36	0.56	0.29	0.38	0.52	0.17	2.98
4	0.22	0.33	0.13	0.18	0.16	0.08	1.41
5	0.10	0.16	0.06	0.10	0.06	0.04	0.72
Exp-3							
0	0.50	0.58	0.55	1.14	0.76	0.66	5.48
1	0.32	0.22	0.23	0.14	0.15	0.04	1.35
2	0.23	0.24	0.17	0.22	0.21	0.18	1.76
3	0.25	0.57	0.41	0.39	0.35	0.31	2.96
4	0.17	0.31	0.18	0.18	0.14	0.12	1.38
5	0.09	0.12	0.05	0.08	0.05	0.05	0.61
Exp-4							
0	0.44	0.60	0.38	0.52	0.97	0.69	5.04
1	0.31	0.21	0.12	0.12	0.14	0.10	1.30
2	0.18	0.27	0.13	0.22	0.20	0.14	1.66
3	0.28	0.52	0.24	0.35	0.38	0.25	2.86
4	0.18	0.28	0.09	0.17	0.12	0.10	1.29
5	0.07	0.11	0.04	0.08	0.04	0.04	0.58

energy spectrum in the vertical index domain (see Figure 3). If the vertical spectrum in Figure 3 is a reflection of dominant baroclinic instability as mentioned before, the results suggest a possible connection between the error growth and the instability of the dynamical system, as discussed by Straus. We note that a finite amplitude initial error grows as fast as the fastest growing mode of the unstable dynamical system if the system is linear, although this is not the case in the real atmosphere. It is interesting to note that both baroclinic instability and error growth for numerical weather prediction have a comparable e-folding time of about 2 days. The bimodal error energy peaks are confirmed for all individual zonal waves  $n = 2-4$  in Table 3, except for  $n = 1$ . The first internal mode of  $m = 1$  at  $n = 1$  indicates larger error energy compared with that for  $m = 3$ , except for the Exp-2. The very large error energy for  $m = 1$  at  $n = 1$  apparently is different from other zonal waves, and will be examined.

## 6 Vertical Propagation of Wavenumber 1

The unrealistic behavior of the first internal mode  $m = 1$  of wavenumber  $n = 1$  in the GLA simulations

has been pointed out by Tanaka et al. (1986). According to our previous result, the simulated component of  $m = 1$  at  $n = 1$ , starting from an initial data at 16 December 1978, indicated the minimum amplitude throughout the period without being amplified, while the observed component underwent occasional amplifications corresponding to the vertical propagation of  $n = 1$ . Figure 6 shows the time series of total energy  $E = K + P$  of the component ( $n = 1, m = 1$ ) for the observations and simulations starting from the initial data of 1 January 1979. During the integration period, the observed energy is maintained at approximately the same level. In contrast, in all simulations the energy tends to increase during the earlier half of the period. This is a remarkable difference caused by the different initial data compared to our previous experiment. As shown in Table 3, the largest portion of the forecast error for  $n = 1$  in the baroclinic component comes from  $m = 1$ . It is noted that  $m = 1$  has an increasingly large amplitude near the top of the model (see Figure 1). This implies that the systematic bias of simulations occurs at the top of the model atmosphere. Figure 6 also demonstrates that there is no improvement by the increase of the model resolution and the use of different initial datasets of 1 January 1979.



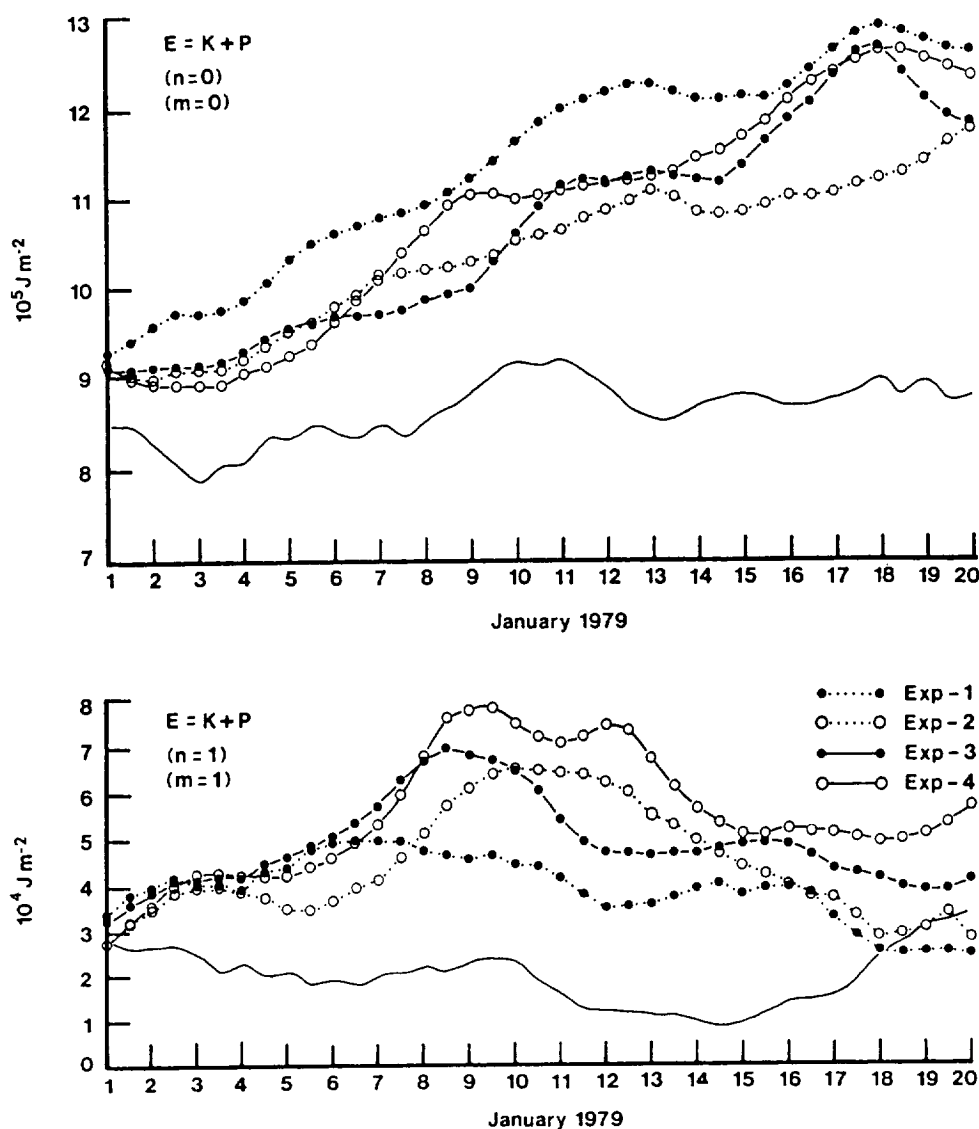
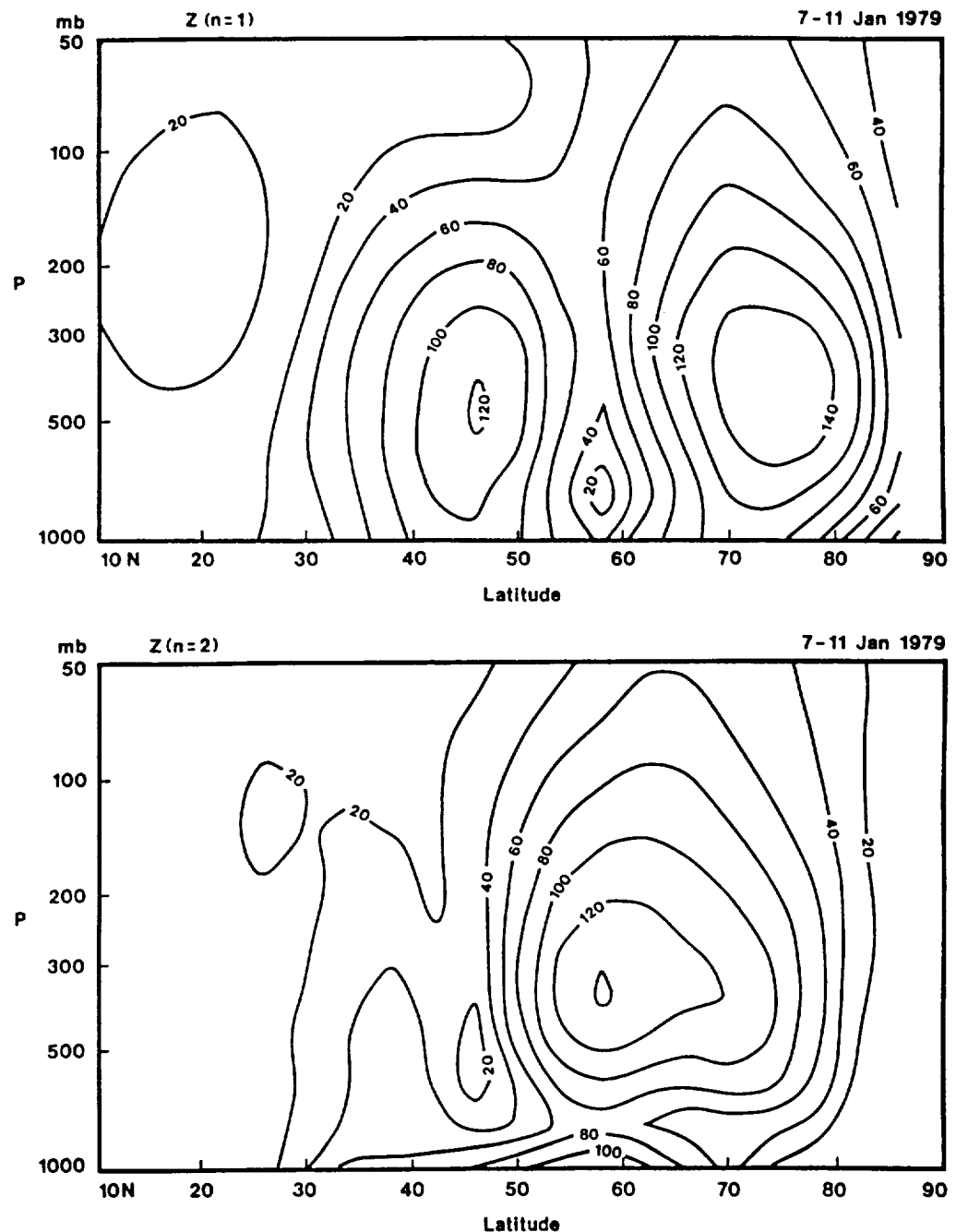


Figure 6 Time series of total energy  $E = K + P$  for the first internal modes of wavenumber 1 ( $n = 1, m = 1$ ). Observed time series of the same component is by a solid line without symbols.

The discrepancy in  $n = 1$  between the simulations and the observations can be traced to the misleading geopotential field near the top of the model atmosphere. Figure 7 shows the observed 5-day means of geopotential height amplitude of  $n = 1$  and 2 in the Northern Hemisphere during 7–11 January 1979. The same meridional-height cross sections in the simulations for  $n = 1$  are shown in Figure 8. Geopotential height in these figures is multiplied by a common dimensionless factor of  $(p/p_s)^{1/2}$  in order to remove the basic density stratification effect. In Figures 7 and 8 the discrepancies in geopotential height fields in the simulations are evident. During days 7–11 a large-

scale Pacific blocking with a high-low vortex pair reaches its mature stage (Kung and Baker, 1986b). Related to this Pacific blocking, a clear dipole structure of  $n = 1$  appears in the meridional cross section of Figure 7 indicating two amplitude maxima at  $45^\circ\text{N}$  and  $75^\circ\text{N}$ . The northern pole has its height ridge over Alaska, and the southern pole has its trough over the Pacific Ocean. The amplitude peaks appear at 500 mb. Such a clear dipole structure is not observed for  $n = 2$ . The basic structure of this Pacific blocking can be described by superimposing the dipole structure of  $n = 1$  on that of  $n = 2$ . On the other hand, in simulations, the dipole structure of  $n = 1$  is not well handled.



**Figure 7** Meridional-height cross sections of geopotential height amplitude  $Z$  in the Northern Hemisphere for wavenumbers  $n = 1$  and  $2$ . The values are observed 5-day means for 7–11 January 1979, and are weighted by  $(p/p_0)^{1/2}$  to remove the density stratification effect.

The northern part of the amplitude maximum propagates away into the stratosphere. This discrepancy of unrealistic vertical propagation in simulations may explain the systematic bias in the energy of the increasing first internal vertical mode of  $n = 1$  as shown in Figure 6.

## 7 Concluding Summary

Comparative energetics are presented for four one-month GLA GCM simulations for January 1979, integrated from initial conditions at 0000 GMT 1 January 1979. These four numerical experiments involve a combination of two different horizontal

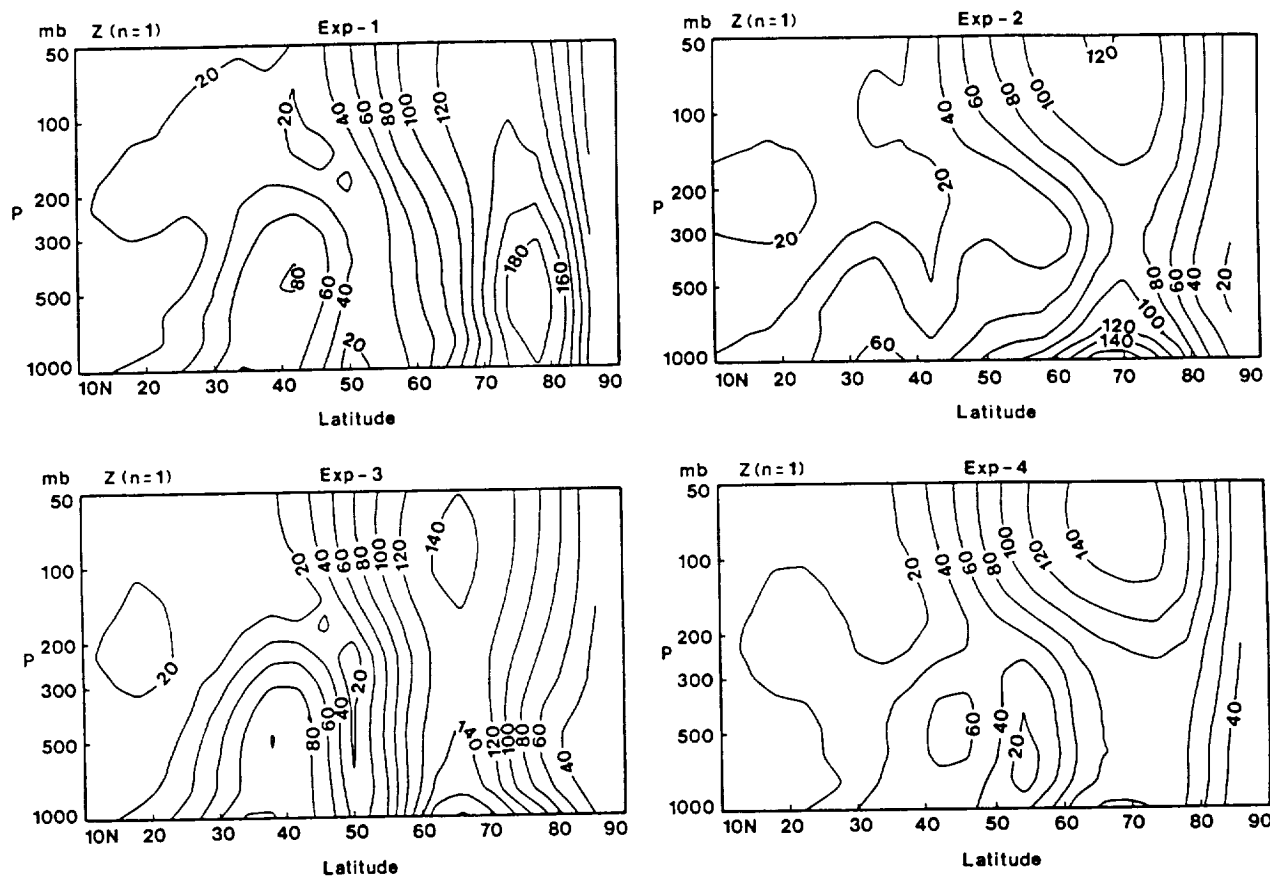


Figure 8 As in Figure 7, but for the four simulations during the same period.

grid resolutions and two sets of initial conditions prepared by the GLA and GFDL. The effect of increased horizontal resolution from the standard  $4^\circ \times 5^\circ$  latitude-longitude grid to the  $2^\circ \times 2.5^\circ$  grid, and the effect of the initial datasets upon the climatic drift of the model are examined using a recently developed normal mode energetics scheme.

For one-month averages of the time integrations, it is found that the gravity mode energy levels are significantly reduced in the higher wavenumbers and in the higher order internal vertical modes by the increase in horizontal model resolution. The strong zonal jet with the barotropic structure, and the intense wave-mean interaction of kinetic energy from eddy to zonal field in the simulations, as documented by Tanaka et al. (1986) and Kung and Baker (1986a), are not improved by the increase of model resolutions or different initial conditions.

In the method of the normal mode expansion the prediction errors of the model experiments may be measured by the error norm between the two spectral expansion coefficients of observed and simulated

atmosphere. It is found that the increase of the model resolution reduces the prediction error in planetary waves for  $n = 1$  and 2 of the barotropic component and in synoptic waves for  $n = 5$  of the baroclinic component. It is also apparent that the misleading vertical propagation of planetary waves into the model stratosphere results in a common bias of the prediction in the first internal vertical component ( $m = 1$ ) of wave-number 1. This bias is related to a misrepresentation of the Pacific blocking occurring at the predictability limit of the model atmosphere.

### Acknowledgements

The authors gratefully acknowledge the courtesy of Drs. K. Miyakoda and J. J. Plushay of the Geophysical Fluid Dynamics Laboratory in providing the GFDL initial data, and the assistance of Y. Brin and L. Takacs in the numerical experiments at the Goddard Space Flight Center. The authors are also thankful to S. Humphrey, V. Peters, G. Vickers and D. K. Williams for their Technical Assistance. This research was

performed at Eck Research Consulting Inc. under the National Aeronautics and Space Administration Contract NAS5-30128.

## References

- Boer, G. J., 1984: A spectral analysis of predictability and error in an operational forecast system. *Mon. Wea. Rev.*, **112**, 1183–1197.
- Charney, J. G., R. G. Fleagle, V. W. Lalley, H. Riehl and D. Q. Wark, 1966: The feasibility of a global observational and analysis experiment. *Bull. Amer. Meteor. Soc.*, **47**, 200–220.
- Dalcher, A. and U. Kalnay, 1987: Error growth and predictability in operational ECMWF forecast. *Tellus*, **39A**, 474–491.
- Daley, R., A. Hollingsworth, J. Ploshay, K. Miyakoda, W. Baker, E. Kalnay, D. Dey, T. Krishnamurti and E. Baker, 1985: Objective analysis and assimilation techniques used for the production of FGGE IIb analyses. *Bull. Amer. Meteor. Soc.*, **77**, 532–540.
- Kalnay, E., R. Balgovind, W. Chao, D. Edlmann, J. Phaendner, L. Takacs and K. Takano, 1983: Documentation of the GLAS fourth order general circulation model. NASA Tech. Memo, 86064, (NTIS N8424028).
- Kalnay-Rivas, E., A. Bayliss and J. Storch, 1977: The fourth order GISS model of the global atmosphere. *Beitr. Phys. Atmosph.*, **50**, 299–311.
- Kung, E. C. and W. E. Baker, 1986a: Comparative energetics of the observed and simulated global circulation during the special observing periods of FGGE. *Quart. J. R. Met. Soc.*, **112**, 593–611.
- Kung, E. C. and W. E. Baker, 1986b: Spectral energetics of the observed and simulated Northern Hemisphere general circulation during blocking episodes. *J. Atmosph. Sci.*, **43**, 2792–2812.
- Kung, E. C. and H. Tanaka, 1983: Energetics analysis of the global circulation during the special observation period of FGGE. *J. Atmos. Sci.*, **40**, 2575–2592.
- Lorenz, E. N., 1982: Atmospheric predictability experiments with a large numerical model. *Tellus*, **34**, 505–513.
- Manabe, S., J. Smagorinsky, J. L. Holloway, Jr. and H. M. Stone, 1970: Simulated climatology of a general circulation model with a hydrologic cycle. *Mon. Wea. Rev.*, **98**, 175–213.
- Miyakoda, K., R. F. Strickler, C. J. Nappo, P. L. Baker and G. D. Hembree, 1971: The effect of horizontal grid resolution in an atmospheric circulation model. *J. Atmos. Sci.*, **28**, 481–499.
- Miyakoda, K., J. Sirrutis and J. Ploshay, 1986: One-month forecast experiments without anomaly boundary forcing. *Mon. Wea. Rev.*, **114**, 2363–2401.
- Puri, K. and W. Bourke, 1974: Implications of horizontal resolution in spectral model integrations. *Mon. Wea. Rev.*, **102**, 333–347.
- Salzman, B., 1957: Equations governing the energetics of the larger scales of atmospheric turbulence in the domain of wave number. *J. Meteor.*, **14**, 513–523.
- Shapiro, R., 1970: Smoothing, filtering, and boundary effects. *Rev. Geophys. Space Phys.*, **8**, 359–387.
- Shukla, J., 1985: Predictability. *Issues in Atmospheric and Oceanic Modeling. Advance in Geophysics*, **28**, (ed., S. Manabe) Academic Press, 87–122.
- Smagorinsky, J., 1969: Problems and promises of deterministic extended range forecasting. *Bull. Amer. Meteor. Soc.*, **50**, 286–311.
- Straus, D. M., 1988: The dynamics of error growth in a quasi-geostrophic channel model. *Proc. The Eighth Conference on Numerical Weather Prediction, Americ. Meteor. Soc.*, 614–616.
- Takacs, L. L. and R. C. Balgovind, 1983: High-latitude filtering in global grid-point models. *Mon. Wea. Rev.*, **111**, 2005–2015.
- Tanaka, H., 1985: Global energetics analysis by expansion into three-dimensional normal mode functions during the FGGE winter. *J. Meteor. Soc. Japan*, **63**, 180–200.
- Tanaka, H. L. and E. C. Kung, 1988: Normal mode energetics of the general circulation during the FGGE year. *J. Atmos. Sci.*, **45**, 3723–3736.
- Tanaka, H. L. and E. C. Kung, 1989: A study of low-frequency unstable planetary waves in realistic zonal and zonally varying basic states. *Tellus*, **41**, (in press).
- Tanaka, H., E. C. Kung and W. E. Baker, 1986: Energetics analysis of the observed and simulated general circulation using three-dimensional normal mode expansions. *Tellus*, **38A**, 412–428.
- Welck, R. E., A. Kasahara, W. M. Washington and G. D. Santo, 1971: Effect of horizontal resolution in a finite-difference model of the general circulation. *Mon. Wea. Rev.*, **99**, 673–683.
- Williamson, D. L. and A. Kasahara, 1971: Adaption of meteorological variables forces by updating. *J. Atmos. Sci.*, **28**, 113–1324.
- Yee, S. Y. K. and P. Shapiro, 1981: The interaction of model dynamics and numerical errors in a nondivergent global barotropic model. *Mon. Wea. Rev.*, **109**, 687–700.

#### 4.3 Simulations of winter blocking episodes using observed sea surface temperatures

Ernest C. Kung, Carlos C. DaCamara, Wayman E. Baker,  
Joel Susskind and Chung-Kyu Park

## 1. INTRODUCTION

Due to the dominance of blocking events in the Northern Hemisphere winter, the ability of general circulation models (GCMs) to simulate blocking is a major concern in the medium-range forecast. In our preceding studies we compared energetics features under observed and simulated blocking situations. Kung and Baker (1986) identified an association of the blocking development with the nonlinear wave-wave transfer of kinetic energy from cyclone-scale to ultralong waves. Kung et al. (1989) noted the existence of considerable energetics differences between the simulations and the observations, and among simulations during blocking episodes. Enough energy source is available in the simulations at the synoptic-scale range, but the models tend to provide insufficient kinetic energy to ultralong waves through the wave-wave interaction. Their failure in simulating a realistic blocking can be attributed in part to inadequate grid resolution. The  $4^{\circ}\times 5^{\circ}$  longitude-latitude coarse resolution GCM results in a downscale energy cascade, preventing a proper up-scale input of kinetic energy. The  $2^{\circ}\times 2.5^{\circ}$  high resolution GCM generates a relatively strong blocking with a better wave-wave interaction for upscale input of kinetic energy, but there are obvious spatial and temporal phase errors. The energetics dipole structure of the observed blocking is also nearly absent in the simulations. An orderly transfer of energy from the zonal baroclinic component to the barotropic component of ultralong waves via synoptic-scale conversion with observed blocking episodes (Tanaka and Kung 1988) is either weak or unrecognizable in the simulations.

Aside from the importance of upscale kinetic energy input of wave-

wave interaction, the association of large-scale baroclinic conversion with blocking phenomena has been identified by Hansen and Chen (1982), Murakami and Tomatsu (1965), Paulin (1970) and others. In this paper an additional series of numerical simulations are examined to study the effects of a realistic heating field of the ocean surface on the development of blocking. Three numerical simulations of the global atmosphere for the same period of January 1979, as in our aforementioned preceding studies, were performed using the  $4^\circ \times 5^\circ$  and  $2^\circ \times 2.5^\circ$  versions of the Goddard Laboratory for Atmospheres (GLA) GCM, integrated from the GLA and Geophysical Fluid Dynamics Laboratory (GFDL) initial datasets for 0000 GMT 1 January 1979 (Table 1). In contrast to previous simulations which used the daily January climatology of the sea surface temperature (SST), those three simulations used daily updating of observed SST data for January 1979, which was developed by the fourth and fifth authors of this paper from *in situ* (ship and buoy) and satellite-retrieved data. A simulation reported in Kung et al. (1989) using the high resolution GCM with the GLA initial conditions and a January climatology SST is used in this study as the control run.

For each simulation examined in this study the development of blocking is identified, and its extent and pattern are analyzed. The improved skill in predicting blocking development is described and discussed in terms of the 500 mb anomaly correlation, mean-square error of geopotential height, error kinetic energy, and phase angle and amplitude of the geopotential height of ultralong waves.

## 2. SEA SURFACE TEMPERATURE ANALYSIS AND SIMULATION EXPERIMENTS

A global monthly SST analysis was performed at GLA based on *in situ*

- (ship and buoy) and satellite-retrieved data. In this analysis the *in situ* data were used to define "benchmark" temperature values in regions of frequent *in situ* observations, and the satellite data were used to define the SST pattern between these points. We used medians, rather than weighted means, from the Comprehensive Ocean-Atmosphere Data Set (COADS) of Slutz et al. (1985) to represent the *in situ* SST data in each  $2^{\circ} \times 2^{\circ}$  latitude-longitude grid box. Since the *in situ* data are subject to large sampling errors, these SST data were used only when there were more than 5 observations in each grid box and the standard deviation was less than  $3.5^{\circ}\text{C}$ .
- After eliminating questionable values, the COADS SSTs were transformed through area-weighted average to produce *in situ* SSTs in the  $4^{\circ} \times 5^{\circ}$  latitude-longitude grid. The SST data retrieved from satellite radiances were obtained by the multichannel technique of Susskind and Reuter (1985) using the high resolution infrared sounder (HIRS) and the microwave sounding unit (MSU) on Tiros-N. The approach at GLA is fundamentally different from the current operational approach at the National Environmental Satellite Data and Information Service (NESDIS) in that the surface and atmospheric conditions are determined from the radiative transfer equations with an iterative scheme. Soundings were done in the high spatial resolution mode as described in Reuter et al. (1988). The basic retrieval system and analysis technique are detailed in Susskind et al. (1984) and Susskind and Reuter (1985).

The monthly mean field of the COADS SST and HIRS/MSU SSTs were blended to the  $4^{\circ} \times 5^{\circ}$  grid by solving Poisson's equation, subject to appropriate internal and external boundary conditions (see Oort and Rasmusson, 1971). The technique is similar to the operational blend analysis used at the National Meteorological Center (NMC) (Reynolds, 1988). The COADS SST



data were used to define benchmark values in the region of sufficient (25 or more) *in situ* observations, and the blended SSTs are determined in the remaining regions by

$$\nabla^2(\text{SST}) = \delta.$$

The forcing term  $\delta$  is defined by the Laplacian of the HIRS/MSU SSTs in order to keep the shape of the field by satellite information in regions with little or no *in situ* observations. In the analysis the domain extends from 78°S to 78°N. The external boundary condition is specified by satellite data at the poleward limits and in regions outside the domain. In regions of sufficient *in situ* data the external boundary condition is set equal to the *in situ* analysis. The solution was obtained iteratively when the maximum absolute value of the individual grid point residuals was less than 0.01°C. With the initial guess field given by the satellite data, the convergence took less than 50 iterations. After the completion of the analysis, the blended SSTs were interpolated to produce a dataset on a 2°x 2.5° grid. No further spatial or temporal filtering was applied to the blended SSTs.

Figure 1 shows the anomaly pattern of the blended SST for January 1979. The NMC SST climatology (Reynolds, 1982) was used to compute the anomalies. The anomaly pattern is shown in the region between 60°S and 60°N, although the climatology may not be reliable in the region south of 40°S (Reynolds, 1983). The satellite data have little influence on the blended field in the Northern Hemisphere except in the tropical Pacific. In the Southern Hemisphere, however, the blended field is close to the satellite observations due to the small influence of *in situ* data.

We have compared the large-scale characteristics of the blended SST anomaly field with those two other fields: the SST from the NMC analysis,

which was based on *in situ* data alone (Reynolds and Gemmill, 1984), and the SST field derived using HIRS/MSU sounding alone. We used an empirical orthogonal function (EOF) analysis to filter out high frequency noise. The input data used in the EOF analysis are the normalized monthly SST anomalies in the  $4^{\circ}$  latitude by  $5^{\circ}$  longitude grid in the latitudinal belt between  $40^{\circ}\text{S}$  and  $60^{\circ}\text{N}$  for the period December 1978 to November 1979. The latitude-time sections of the SST anomalies for each of these fields in the eastern Pacific Ocean are shown in Fig. 2. Data used to represent these figures are composed of the first five EOFs averaged in the eastern Pacific (the dateline to the west coast of North America in the North Pacific and  $150^{\circ}\text{W}$  to  $70^{\circ}\text{W}$  in the South Pacific). The blended SST anomalies show smoother large-scale variations and clearer seasonal trends than the *in situ* or satellite SST data alone.

For the GCM experiments, daily gridded SST fields were obtained by linear interpolation of the monthly mean blended fields, assuming that the observed monthly means are located in the middle of each month. The assumption is valid because of the smallness of time variation in the SSTs during winter months. Three simulation experiments (Exps. A, B and C) were conducted for the period of 1-31 January 1979 with the coarse and high resolution versions of GCMs (see Table 1). The GLA and GFDL gridded analyses of the First GARP (Global Atmospheric Research Program) Global Experiment (FGGE) for 0000 GMT 1 January 1979 were used as the initial data (see Daley et al. 1985; Kung and Baker 1986). The coarse resolution GCM used in Exp A is the fourth-order global atmospheric model described by Kalnay-Rivas et al. (1977) and Kalnay et al. (1983). The high resolution version of the GCM used in Exps B and C is identical to the coarse resolution version with respect to physical parameterizations. Use of the GLA

GCM and a description of GLA and GFDL initial datasets are detailed in our preceding report (Kung et al. 1989) and not repeated here. One of four simulations in Kung et al. (1989), which gave the best blocking simulation with the January SST climatology is used as the control run to contrast the simulations with a realistic SST field in this study. The control was run using the high resolution GCM with the GLA initial data. The simulation field analyzed in this study include twice-daily values of the circulation.

### 3. BLOCKING EPISODES

Following the same procedures of our preceding study (Kung et al. 1989), a blocking is recognized when the following index  $I$  at longitude  $\lambda$  is greater than 50m along a longitudinal sector:

$$I(\lambda) = Z(\lambda, 66^\circ\text{N}) - Z(\lambda, 46^\circ\text{N})$$

where  $Z$  is the geopotential height at 500 mb. This criteria is based on the common characteristic of diffluent and meridional types of blocking, in both of which a quasi-meridional dipole is formed by a high pressure cell poleward and a low pressure area equatorward (see Lejenäs and Økland 1983). In the additional scan for the cases of tilted orientation of meridional dipole and cases of blocking which are partially out of the chosen latitudinal band,  $Z(\lambda \pm 5^\circ, 66^\circ\text{N})$  is substituted for  $Z(\lambda, 66^\circ\text{N})$  in the above equation. The blocking identified in this method is verified by manual inspection of the flow pattern.

Figures 3-6 are longitude-time diagrams of identified blockings in the three simulations and the control run. The horizontal segments in bold lines represent the longitudinal sectors in which blockings are recognized. The figures also contrast the simulated blockings with the observed block-

ings by Kung and Baker (1986) which are shown with dot-dashed lines. Table 1 lists the periods of identified blocking episodes in the Northern Hemisphere for the simulations and compares them with those of observed episodes. The control run (Fig. 6) is the only simulation in Kung et al. (1989) with the mean January SST climatology that produced a realistically strong Pacific blocking early in the month, and another blocking later, toward the end of the month. However, the second blocking was weak and the block was dislocated to the east of the observed block in the Atlantic. As seen in Figs. 3-5, the improvement in simulating blocking using the realistic SST field is obvious. All three experiments (A, B and C) produced a Pacific blocking early in the month, and an Atlantic blocking later in the month. In Exp A the Atlantic blocking is weak and short-lived. This apparently is the effect of the coarse resolution of GCM as noted in Kung et al. (1989). In Exps B and C (Figs. 4-5) with the high resolution GCM, the Atlantic blocking is much stronger than in Exp A and more enduring. Among the three simulations it appears that Exp B using the high resolution GCM with GLA initial data produced the most realistic simulation of the Pacific and Atlantic blockings, both in the period of occurrence and longitudinal extent.

Comparing the simulated 500 mb circulations with the observed circulation during a 5-day period of the developed Pacific blocking in Fig. 7, Exp B shows the closest blocking pattern to the observation both in the shape and the location of the block, which is consistent with the features observed in the longitude-time diagrams. The general pattern of the entire Northern Hemisphere circulation is also much better in Exps B and C than in Exp A. During a similar 5-day period of the Atlantic blocking, Exp B again shows a blocking pattern in closest agreement to the observation. However,

as indicated in Table 1 and Fig. 4, the development of the Atlantic blocking is delayed for several days in the simulation. Exp C produced a dipole structure. However, the blocking is dislocated to the east, the jet is more zonal, and the blocking period is shorter than in Exp B and in the observation (Table 1 and Fig. 5). Exp A, using the coarse resolution GCM, indicates the formation of the Atlantic blocking, but the occurrence is much delayed and the amplitude and longitudinal extent of the blocking are also limited (Table 1 and Fig. 3).

Examination of simulated blocking episodes apparently indicates that the simulation by a high resolution GCM, using a realistic SST field as a boundary condition, is capable of generating a second major blocking event. As clarified in Kung et al. (1989), the high resolution GCM is able to realistically produce the first (Pacific) blocking episode through the upscale kinetic energy input into the ultralong waves by the wave-wave interaction. Since the development of blocking immediately follows the initialization of the GCM, we may assume an existence of an adequate amount and spatial distribution of baroclinic energy (see Tanaka and Kung 1988) within the initial data. For the second (Atlantic) blocking event toward the end of the simulation period, however, the required source of baroclinic energy must be provided by some other means. This may suggest that the realistic ocean surface heating has provided an adequate baroclinic energy source during the simulation. Thus, the GCM is able to produce a realistic second blocking, even after the effects of initialization are presumably lost. However, we cannot determine if the improvement by the heating field results from using the realistic initial SSTs, updating of the SSTs during simulation, or their combined effects. This is a topic for further study.

#### 4. EFFECTS ON EXTENDED-RANGE FORECAST SKILL

This series of GCM simulations for a single month indicates a considerable predictability of the Northern Hemisphere winter blocking when a realistic SST field is prescribed. Bengtsson (1981) found an increased forecast skill in a blocking situation. Shukla (1981) and others (e.g., Holloway and West 1984) show that ultralong wave forecast possesses extended skill (up to 30-45 days) when compared to shorter waves. From this perspective it is not surprising that the improved 30-day GCM simulations in this study have been able to obtain two realistic blockings in succession over the Pacific and Atlantic. To examine the forecast skill of the simulations, the anomaly correlations of the 500 mb geopotential field in the North Pacific sector ( $30^{\circ}$ - $86^{\circ}$ N,  $120^{\circ}$ E- $120^{\circ}$ W) and the North Atlantic sector ( $30^{\circ}$ - $86^{\circ}$ N,  $100^{\circ}$ - $5^{\circ}$ W) are presented in Figs. 9 and 10 for Exps A and B and the control run. The anomaly correlation of Exp B can be seen to represent the group of high resolution simulations with Exps B and C.

Both Figs. 9 and 10 show that following the initial state there is high forecast skill for all three simulations in both the Pacific and Atlantic sectors. Although the skill scores drop in mid-January, toward the end of January the relatively high skill of Exp B becomes apparent with the development of a realistic Atlantic blocking. Exp A shows some insignificant skill at the end of January in association with a rather limited blocking with the coarse resolution GCM. Throughout the simulation period, Exp B exhibits a relatively high anomaly correlation, while the control run, without a realistic SST field, shows a marked deterioration toward the end of the month.

As discussed in our preceding reports (Kung and Baker 1986; Kung et al. 1989), during the major Northern Hemisphere winter blockings, the local

characteristics of the circulation, in and around the blocked region are manifestations of wavenumbers 1 and 2. Since the anomaly correlations shown in Figs. 9 and 10 are for the summation of all zonal wavenumbers, the high skill scores later in the month is obtained only when the ultralong waves dominate the Northern Hemisphere circulation during the Atlantic blocking.

The forecast skill of ultralong waves may be examined by separating zonal wavenumbers  $n=1$  and 2 from other wavenumbers in the error growth of geopotential height and error kinetic energy during the simulation period. The former is expressed in terms of a root-mean square error in the 500 mb geopotential height field in Fig. 11, and the latter in terms of a mean-square error in the 500 mb wind field in Fig. 12. Both are taken in the  $38^{\circ}$ - $70^{\circ}$ N latitudinal band. Figures 11 and 12 indicate that the ultralong waves ( $n=1-2$ ) in all of the simulations show high skill relative to the persistence up to 17-18 days. Beyond that, Exps B and C, using the high resolution GCM, still show good skill toward the end of the month. However, for shorter waves of  $n=3-10$ , the forecast skill is only recognizable for the initial 7-10 days of the simulation. Examination of the forecast skill of the simulations clearly suggests that the improved blocking simulation with the realistic SST field, particularly the generation of the second blocking event in the Atlantic toward the end of the one-month period, is due to the improved prediction of the ultralong waves.

Figure 13 illustrates the  $n=1-2$  trough-ridge diagram during January 1979 with the 500 mb geopotential field, in which both the amplitude and phase angle of the wave are inferred through the period. During the development stage of the Pacific blocking both  $n=1$  and 2 of simulations come in phase with the observations, indicating a reasonable blocking

development in all three simulations. It is noted, however, that only in the observations does the  $n=2$  amplitude reach a sharp peak which is more than twice that of  $n=1$ . All three of the simulations show a much smaller  $n=2$  amplitude than the observations before the maturing stage of the Pacific blocking. It is also noteworthy that, despite a realistic Pacific blocking simulated in all three experiments, the  $n=1$  amplitude in Exp B is much larger than that of the observations and of Exps A and C. There is a considerable deviation of the  $n=2$  phase angle and amplitude during the Atlantic blocking in all simulations from the observations. The  $n=1$  simulations are much better in this respect during the Atlantic blocking. However, the amplitudes of  $n=1$  simulations are smaller than the observations. This is consistent with the fact that the successful simulations of the Atlantic blocking in Exps B and C still lack the observed strength (see Fig. 8). It is apparent that the improved simulation of the Atlantic blocking episode is due to the more realistic behavior of  $n=1$  in the later period. Regardless, this study indicates that further improvement is needed, as shown by the smaller amplitude of  $n=1$  than in the observations.

## 5. CONCLUDING REMARKS

Simulation experiments using the high resolution GLA GCM with a realistic ocean surface heating field are capable of generating two successive major blocking events in the Pacific and Atlantic during January 1979. In connection with the development of the second blocking episode in the Atlantic toward the end of the month, this study suggests that the realistic heating field has provided an adequate baroclinic energy source, which in turn, was transferred into the ultralong waves through upscale wave-wave interaction of kinetic energy.



The success in simulating the blocking formation, as shown in this study, is due to the improved forecast skill of the ultralong waves. The improved simulation of the  $n=1$  phase angle in particular contributes in this regard. It should be recognized, however, that the individual wave-numbers  $n=1$  and 2 still have recognizable deviations from those of the observations.

Although the improved blocking simulation has resulted from the use of a realistic heating field, we cannot determine in this study if it is due to the improved initial field of SSTs, their realistic time variations during the simulation, or their combined effect. This may be studied through a detailed analysis of the internal energy flow, and preferably in an additional series of simulations with various initial times. It is important to note that only one initial state (1 January 1979) is involved in this series of simulations. As such, the results can not be generalized. On the other hand, they are encouraging enough to suggest that additional experiments be run. The Dynamical Extended Range Forecasting at NMC clearly establishes the dependency of forecast on the initial regime of flow (Tracton et al. 1989), but blocking episodes were not well simulated. Such an experiment also seems an ideal testbed for future study.

If the results of future blocking simulations indicate the importance of updating SSTs during the model integration, then one possible conclusion would be that a coupled ocean-atmosphere model is critical for significantly improving extended-range forecast skill. Another view would be that what is being tested is the upper limit of what would be possible with a coupled ocean-atmosphere model, since updating the observed SSTs during the atmospheric model integration may imply a correct ocean model SST prediction.

**ACKNOWLEDGMENT**

The authors are indebted to Mr. L. Takacs for his assistance in executing the numerical experiments at the Goddard Space Flight Center, and to Drs. Miyakoda and J. J. Ploshay of the Geophysical Fluid Dynamics Laboratory in providing the GFDL initial data, and to Dr. R. W. Reynolds and Ms. D. C. Marsico of the National Meteorological Center in providing the NMC sea surface temperature data. They are also thankful to D. Williams and G. Vickers for their technical assistance. This research was performed at ECK Research Consulting, Inc. under the National Aeronautics and Space Administration Contract NAS5-30128.

## REFERENCES

- Bengtsson, L., 1981: Numerical prediction of atmospheric blocking--a case study. *Tellus*, 33, 19-42.
- Daley, R., Hollingworth, A., Ploshay, J., Miyakoda, K., Baker, W., Kalnay, E., Dey, D., Krishnamurti, T. and Barker, E., 1985: Objective analysis and assimilation techniques used for the production of FGGE IIb analysis. *Bull. Amer. Meteor. Soc.*, 77, 532-540.
- Hansen, A.R. and Chen, T.C., 1982: A spectral energetics analysis of atmospheric blocking. *Mon. Wea. Rev.*, 108, 1146-1165.
- Hollaway, B. and West, B.J., Eds. 1984: *Predictability of Fluid Motions*. American Institute of Physics. 612 pp.
- Kalnay, E., Balgovind, R., Chao, W., Edelman, D., Phaendtnr, J., Takacs, L. and Takano, K., 1983: Documentation of the GLAS fourth order general circulation model. NASA Tech. Memo 86064. [NTIS N8424028.]
- Kalnay-Rivas, E., Bayliss, A. and Storch, J., 1977: The fourth order GISS model of the global atmosphere. *Beitr. Phys. Atmos.* 50, 299-311.
- Kung, E.C. and Baker, W.E., 1986: Spectral energetics of the observed and simulated Northern Hemisphere general circulation during blocking periods. *J. Atmos. Sci.*, 43, 2792-2812.
- Kung, E.C., Tanaka, H.L. and Baker, W.E., 1989: Energetics examination of winter blocking simulations in the Northern Hemisphere. *Mon. Wea. Rev.*, 117, No. 8. (In press).
- Lejenäs, H. and Økland, H., 1983: Characteristics of Northern Hemisphere blocking as determined from a long time series of observational data. *Tellus*, 35A, 350-362.
- Murakami, T. and Tomatsu, K., 1965: Energy cycle in the lower atmosphere.

- J. Meteor. Soc. Japan*, 43, 73-89.
- Oort, A.H. and Rasmusson, E.M., 1971: Atmospheric circulation statistics. NOAA Professional Paper No. 5, 323 pp. [Available from US Government Printing Office, Washington, D.C., 20402, Stock No. 0317-0045.]
- Paulin, G., 1970: A study of the energetics of January 1959. *Mon. Wea. Rev.*, 98, 795-809.
- Reuter, D., J. Susskind and A. Pirsch, 1988: First-guess dependence of physically based set of temperature-humidity retrievals from HIRS2/MSU data. *J. Atm. Ocean. Tech.*, 5, 70-83.
- Reynolds, R.W., 1982: A monthly averaged climatology of sea surface temperatures. NOAA Tech. Report NWS 31, [Available from NOAA, National Meteorological Center, Washington D.C.], 33 pp.
- Reynolds, R.W., 1983: A comparison of sea surface temperature climatologies. *J. Climate and Appl. Meteor.*, 22, 447-459.
- Reynolds, R.W., 1988: A real-time global sea surface temperature analysis. *J. Climate*, 1, 75-86.
- Reynolds, R.W. and W.H. Gemmill, 1984: An objective global monthly mean seasurface temperature analysis. *Tropical Ocean-Atmosphere Newsletter*, No. 23, 4-5.
- Shukla, J., 1981: Dynamical predictability of monthly means. *J. Atmos. Sci.*, 38, 2547-2572.
- Slutz, R.J., Lubker, S.J., Hiscox, J.D., Woodruff, S.D., Jenne, R.L., Joseph, D.H., Steurer, P.M. and Elms, J.D., 1985: COADS, Comprehensive Ocean-Atmosphere Data Set. Release 1, 262 pp. [Available from NOAA Climate Research Program, Environmental Research Laboratories, Boulder, CO 80303.]

- Susskind, J. and Reuter, D., 1985: Retrieval of sea surface temperature from HIRS/MSU. *J. Geophys. Res.*, 90, 11602-11608.
- Susskind, J., Rosenfield, J., Reuter, D. and Chahine, M.T., 1984: Remote sensing of weather and climate parameters from HIRS/MSU on TIROS-N, *J. Geophys. Res.*, 89, 4677-4697.
- Tanaka, H.L. and Kung, E.C., 1988: Normal mode energetic of the general circulation during the FGGE year. *J. Atmos. Sci.*, 45, 3723-3736.
- Tracton, M.S., Mo, K., Chen, W., Kalnay, E., Kistler, R. and White, G., 1989: Dynamical Extended Range Forecasting (DERF) at the National Meteorological Center. *Mon. Wea. Rev.* 117, 1604-1635.

TABLE 1. Three simulation experiments and the control run of the January 1979 global atmosphere with GLA GCM, and blocking episodes identified in the observed and simulated Northern Hemisphere circulation.

Run	GCM grid (latitude x longitude)	1/1/79 0000 GMT initial data	Blocking period (day/mo/yr)
Observation	—	—	3/1-14/1/79 12/1-29/1/79
Exp A	4°x5°	GLA	3/1-16/1/79 27/1-30/1/79
Exp B	2°x2.5°	GLA	3/1-16/1/79 18/1-31/1/79
Exp C	2°x2.5°	GFDL	7/1-14/1/79 16/1-25/1/79
Control	2°x2.5°	GLA	3/1-12/1/79 21/1-25/1/79 28/1-30/1/79

## FIGURES

Figure 1. January 1979 patterns of blended SST anomaly. Contour interval is  $0.5^{\circ}\text{C}$ . Positive anomalies are shaded.

Figure 2. Latitude-time sections of SST anomaly in the eastern Pacific Ocean for (a) NMC analysis SST based on *in situ* measurements only, (b) HIRS/MSU SST and (c) GLA blended SST. Contour interval is  $0.2^{\circ}\text{C}$ . Positive anomalies are shaded.

Figure 3. Longitude-time diagram of blocking in Exp A (bold lines) as identified in the daily 0000 GMT 500 mb charts. Dot-dashed lines are for the observed blocking after Kung and Baker (1986).

Figure 4. As in Figure 3, but for Exp B.

Figure 5. As in Figure 3, but for Exp C.

Figure 6. As in Figure 3, but for the control run.

Figure 7. Observed and simulated 500 mb circulation during a 5-day period of the developed Pacific blocking.

Figure 8. As in Figure 7, but for the Atlantic blocking.

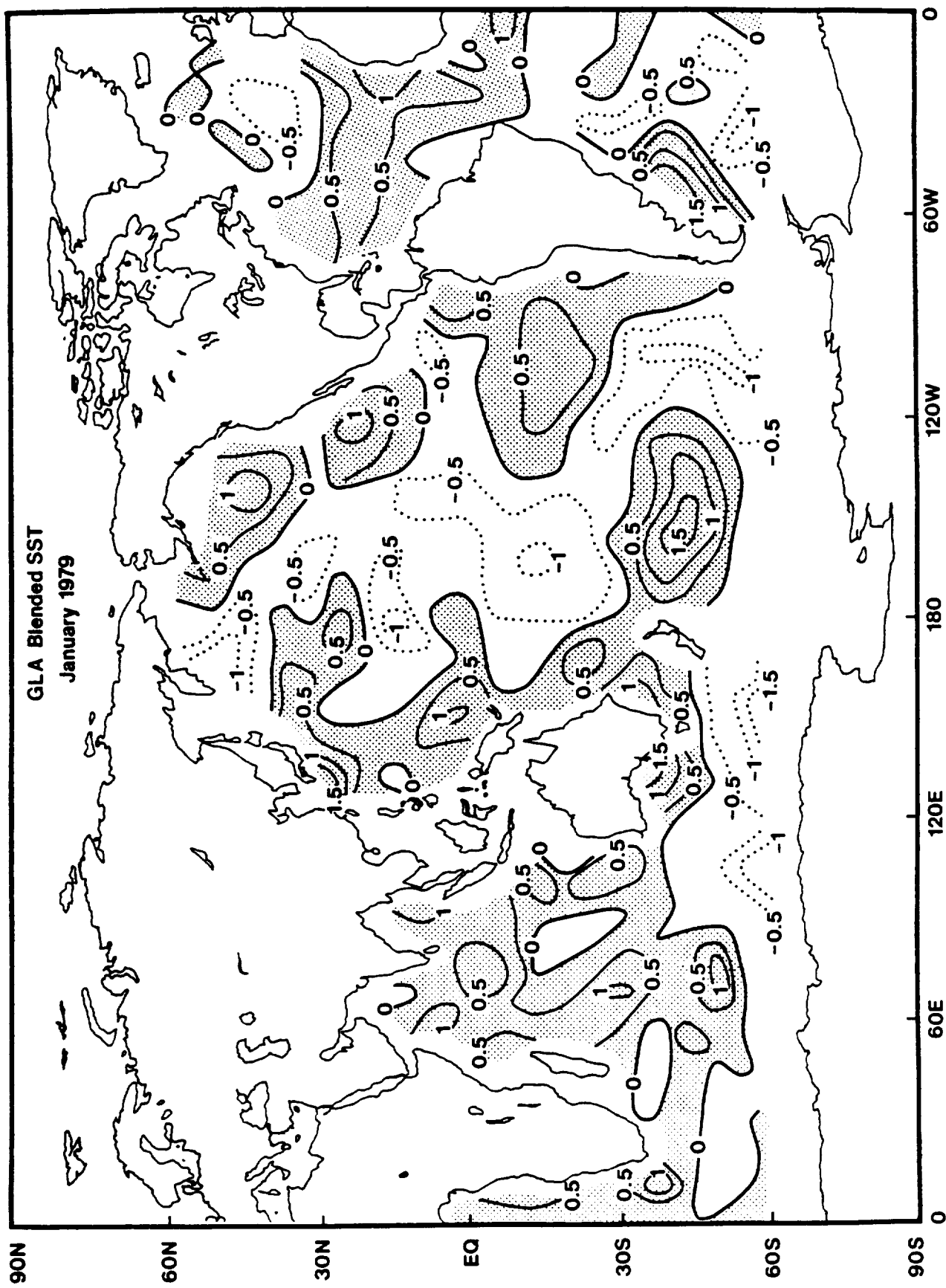
Figure 9. Anomaly correlations of the 500 mb geopotential field in the North Pacific sector.

Figure 10. As in Figure 9, but for the North Atlantic sector.

Figure 11. Root-mean square error of 500 mb geopotential height for ultra-long ( $n=1-2$ ) and synoptic-scale ( $n=3-10$ ) waves in the  $38^{\circ}-70^{\circ}$  latitudinal band.

Figure 12. As in Figure 11, but for the 500 mb error kinetic energy (mean-square error of the wind).

Figure 13. Trough-ridge diagram of  $n=1$  and 2 with 500 mb geopotential height during January 1979 in the  $54-70^{\circ}\text{N}$  band. The contour spacing is 50m and negative contour lines are dashed.





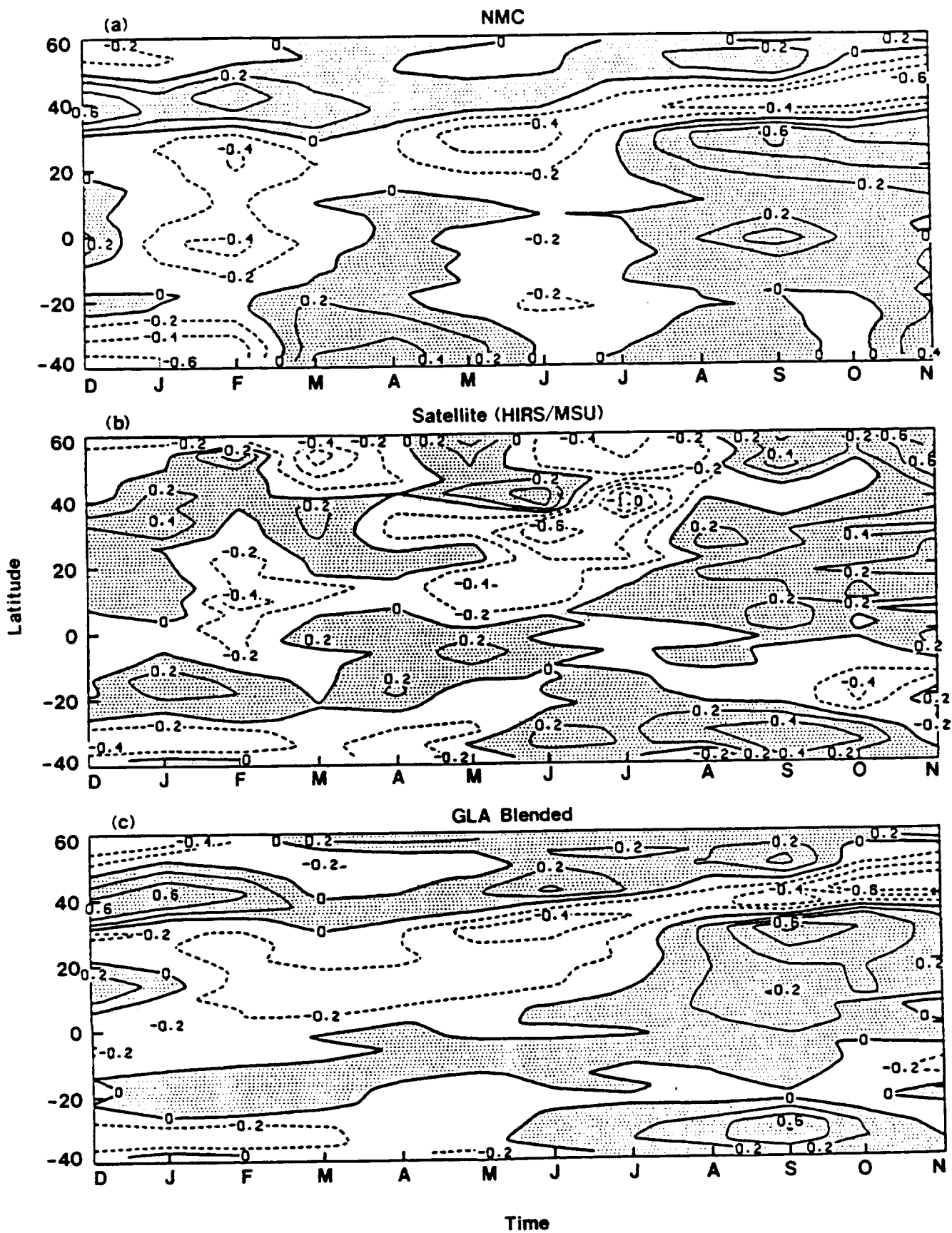


Figure 2

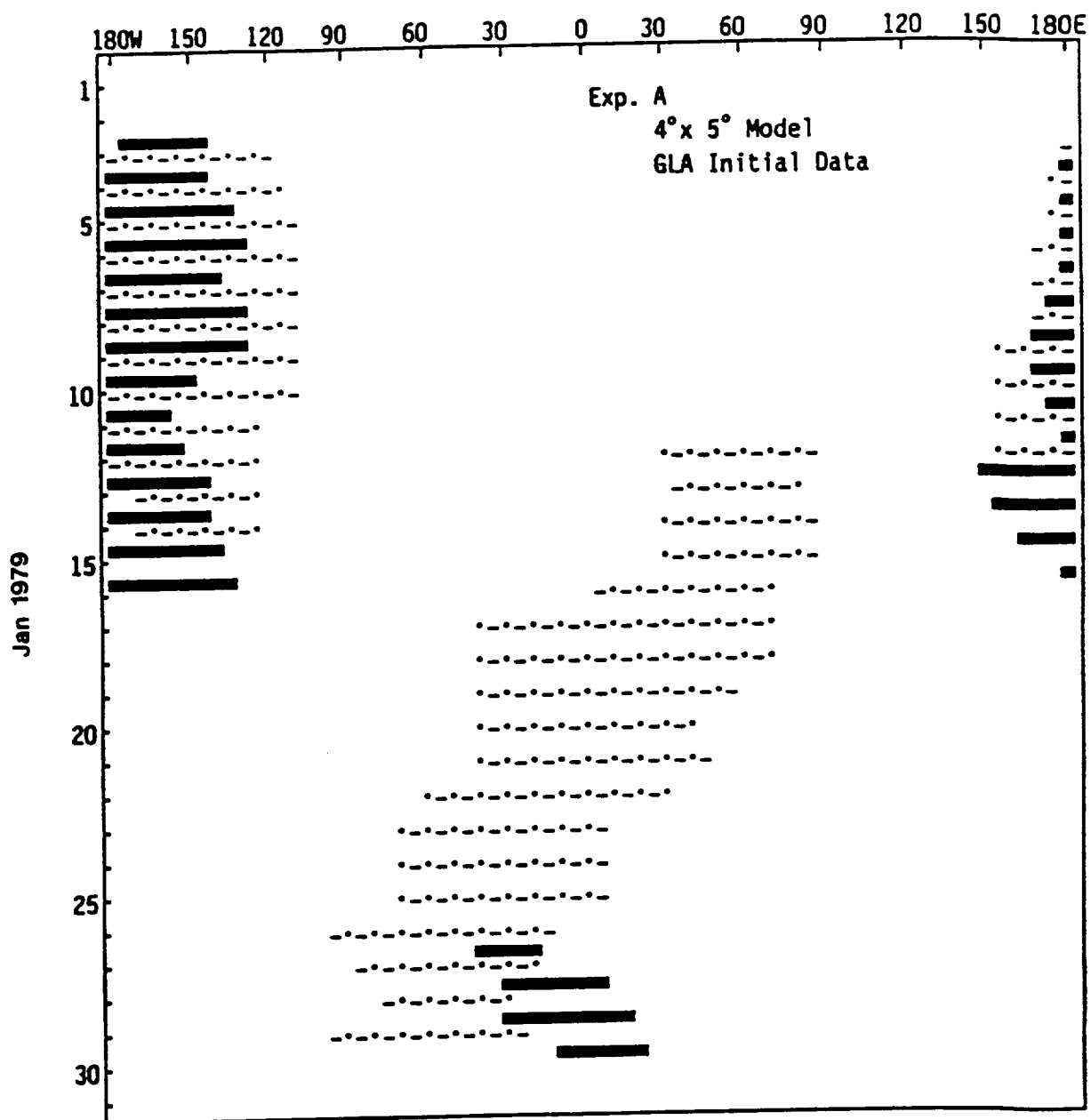


Figure 3

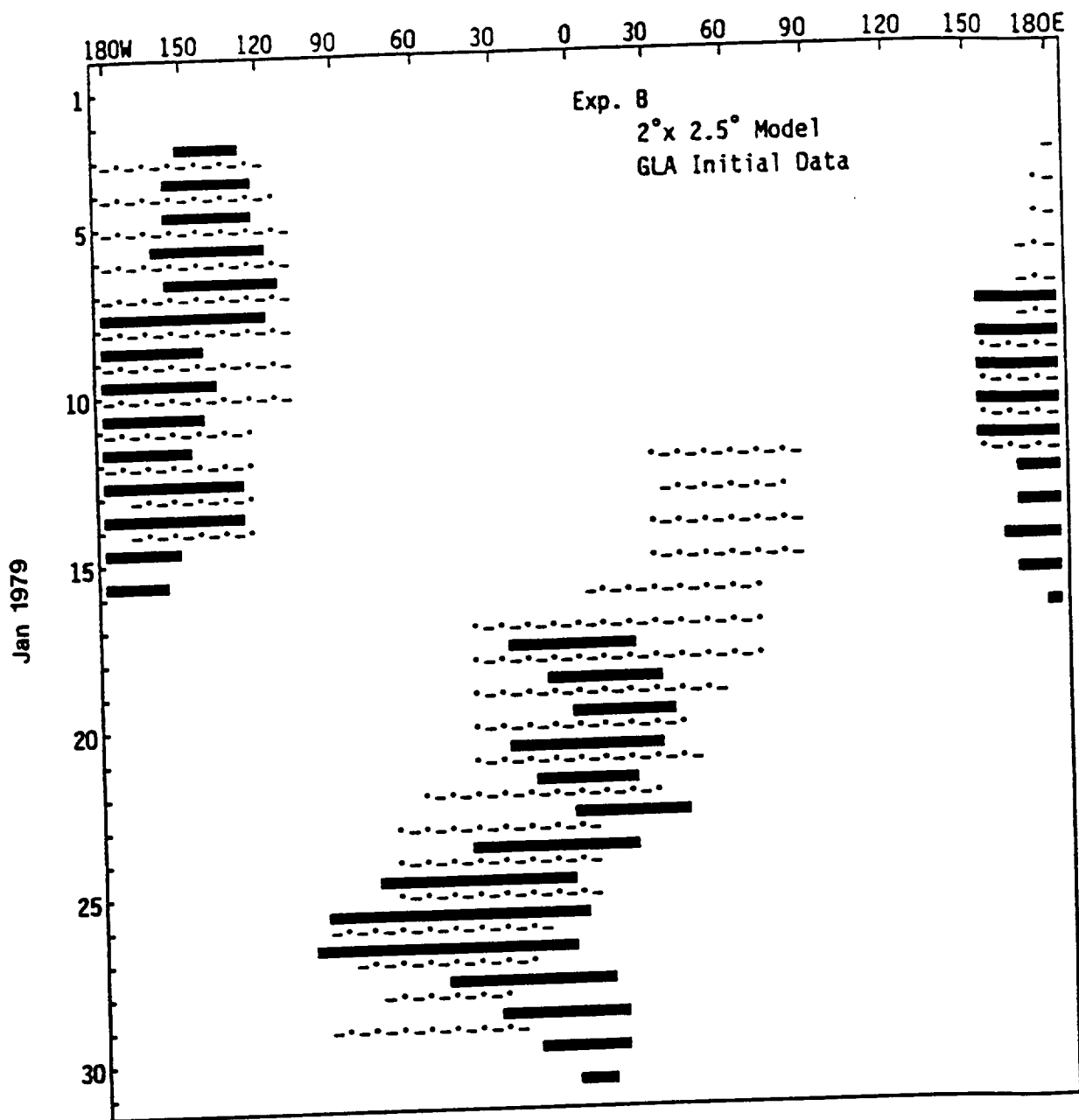


Figure 4

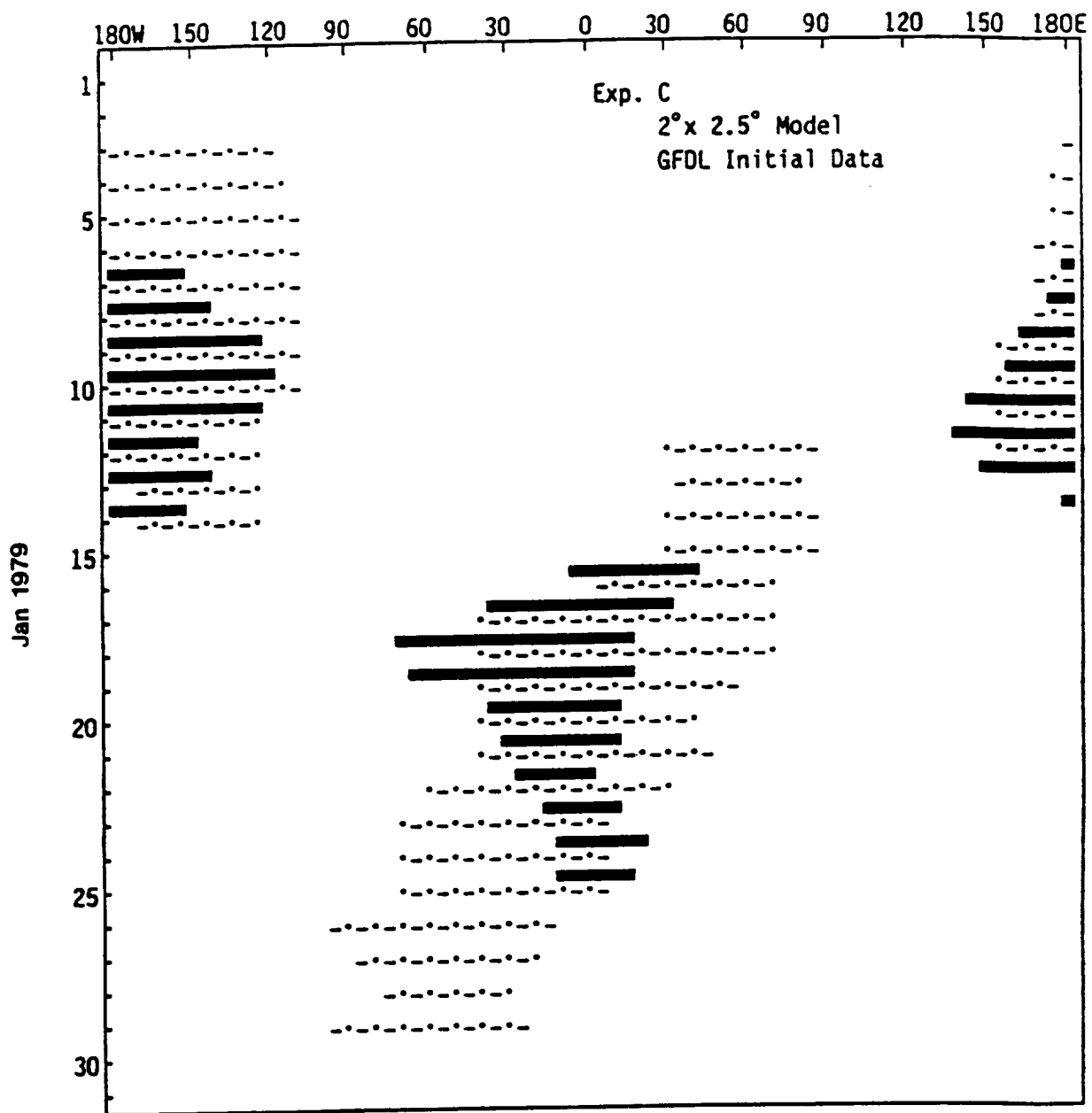


Figure 5

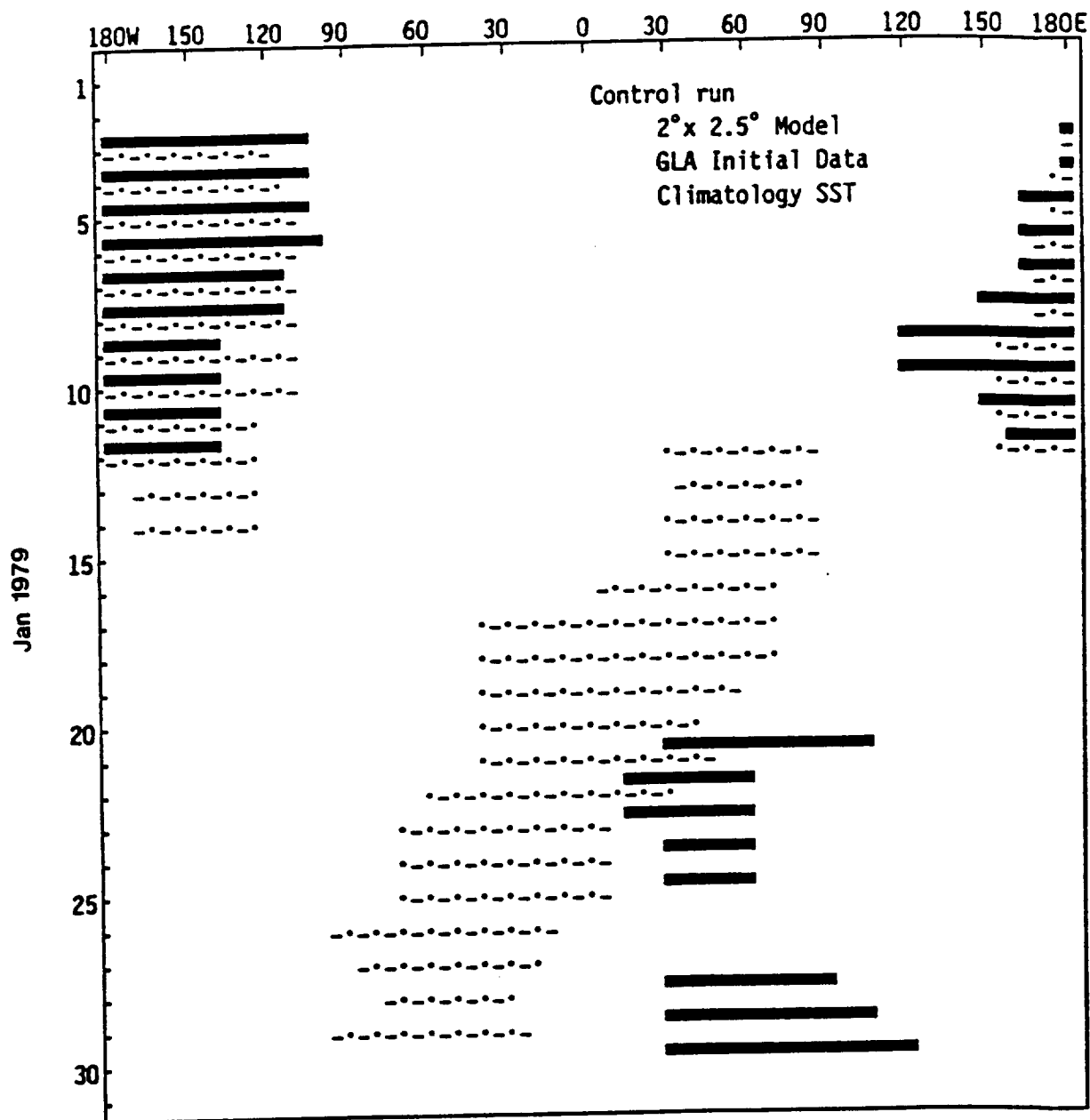


Figure 6

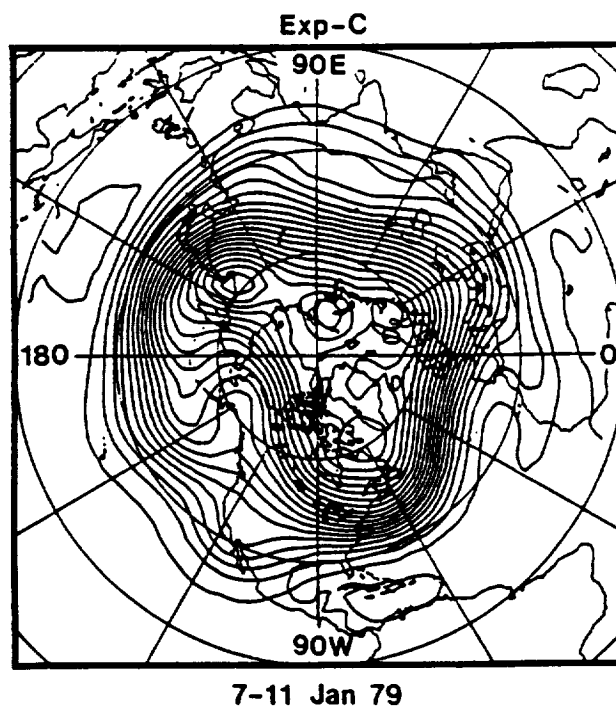
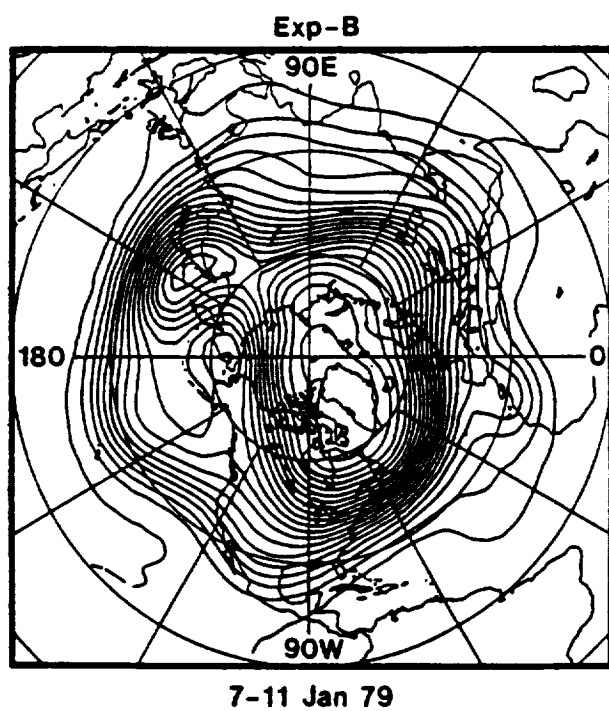
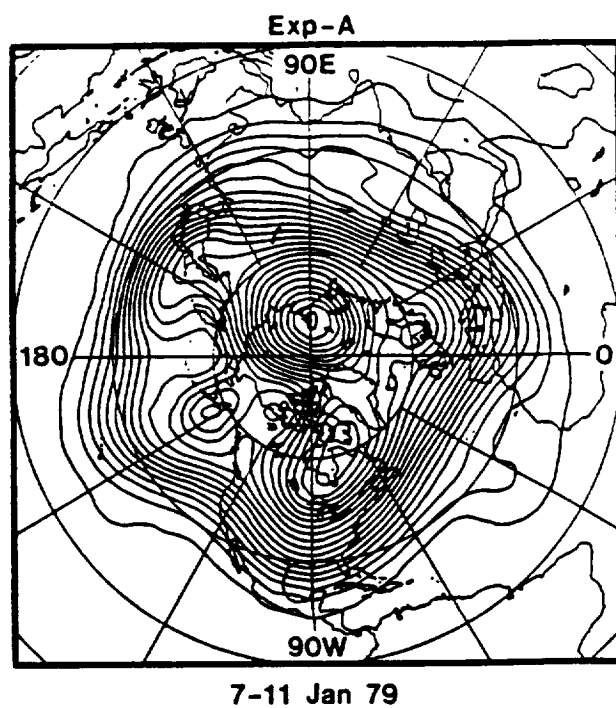
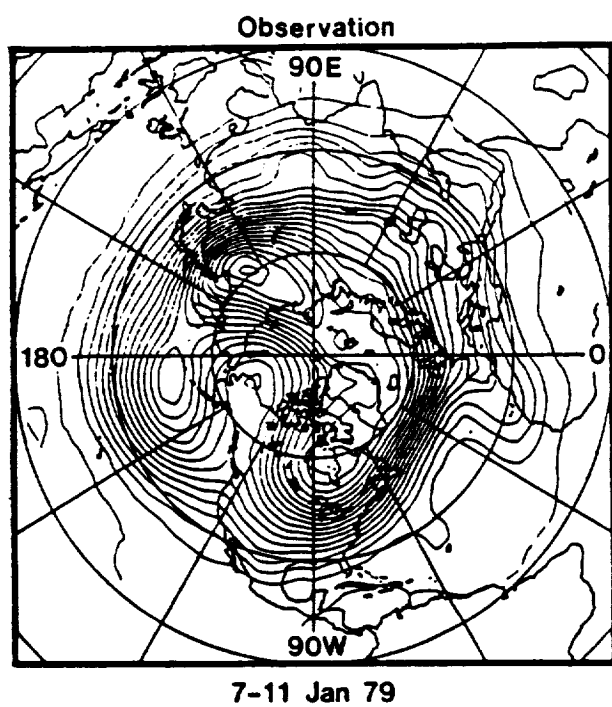
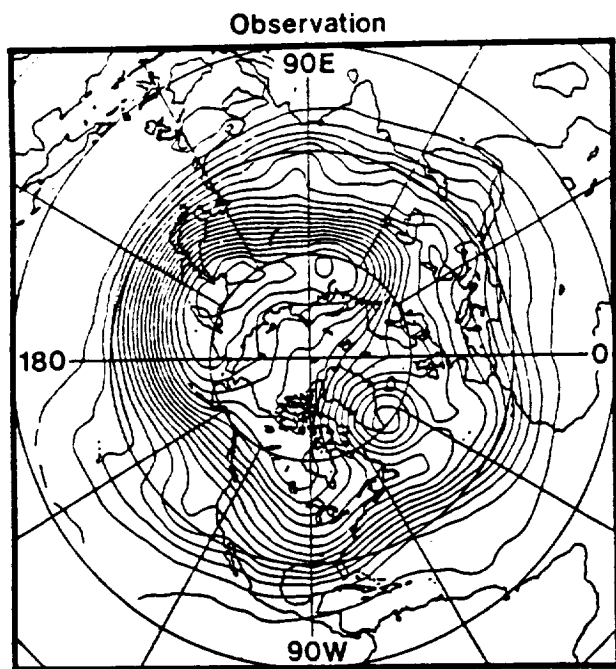
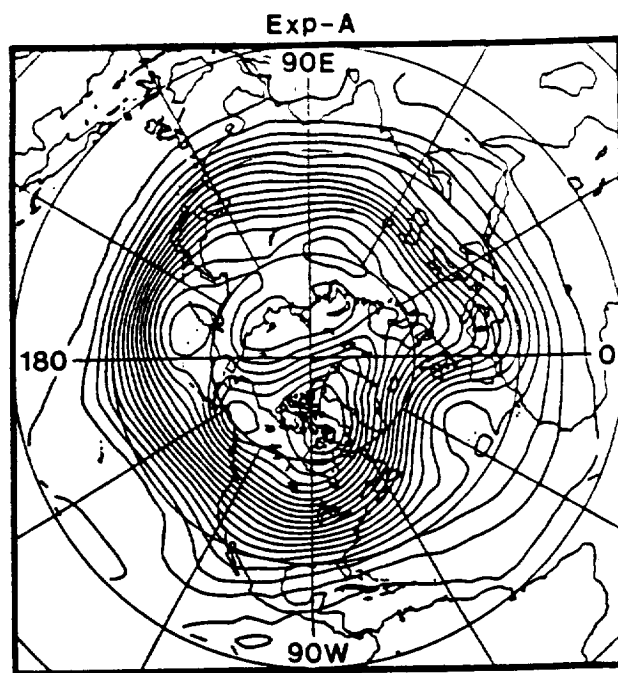


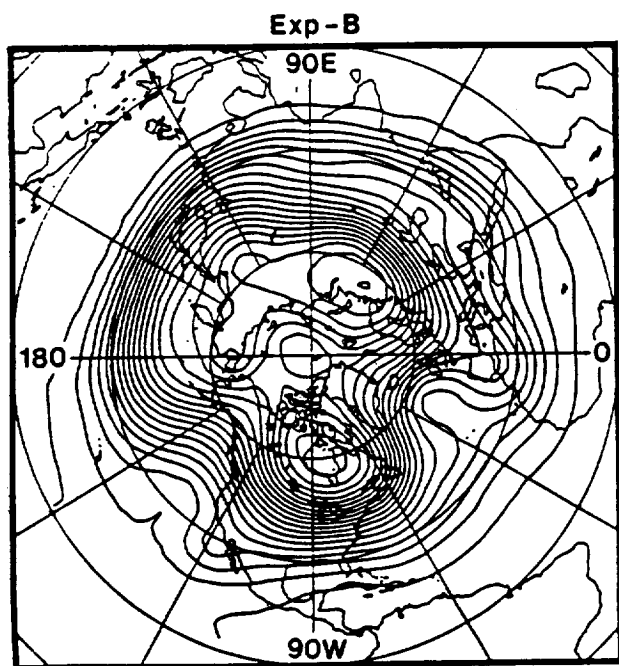
Figure 7



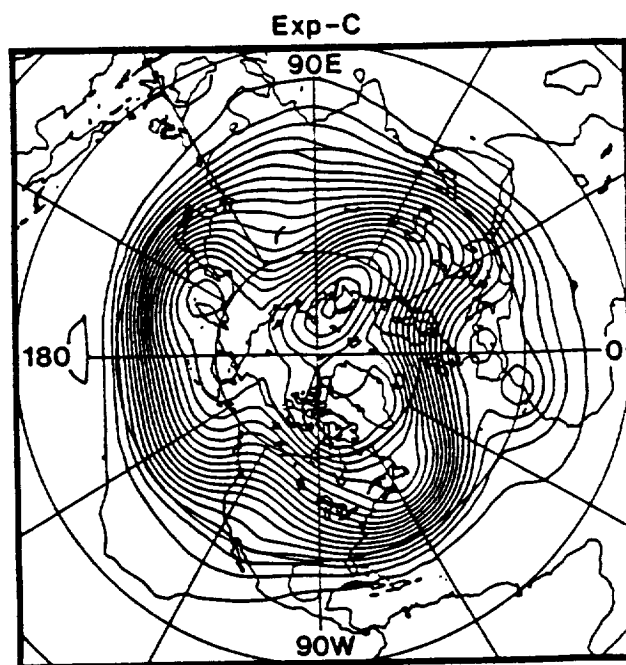
21 - 25 Jan 79



26 - 30 Jan 79



24 - 28 Jan 79



21 - 25 Jan 79

Figure 8

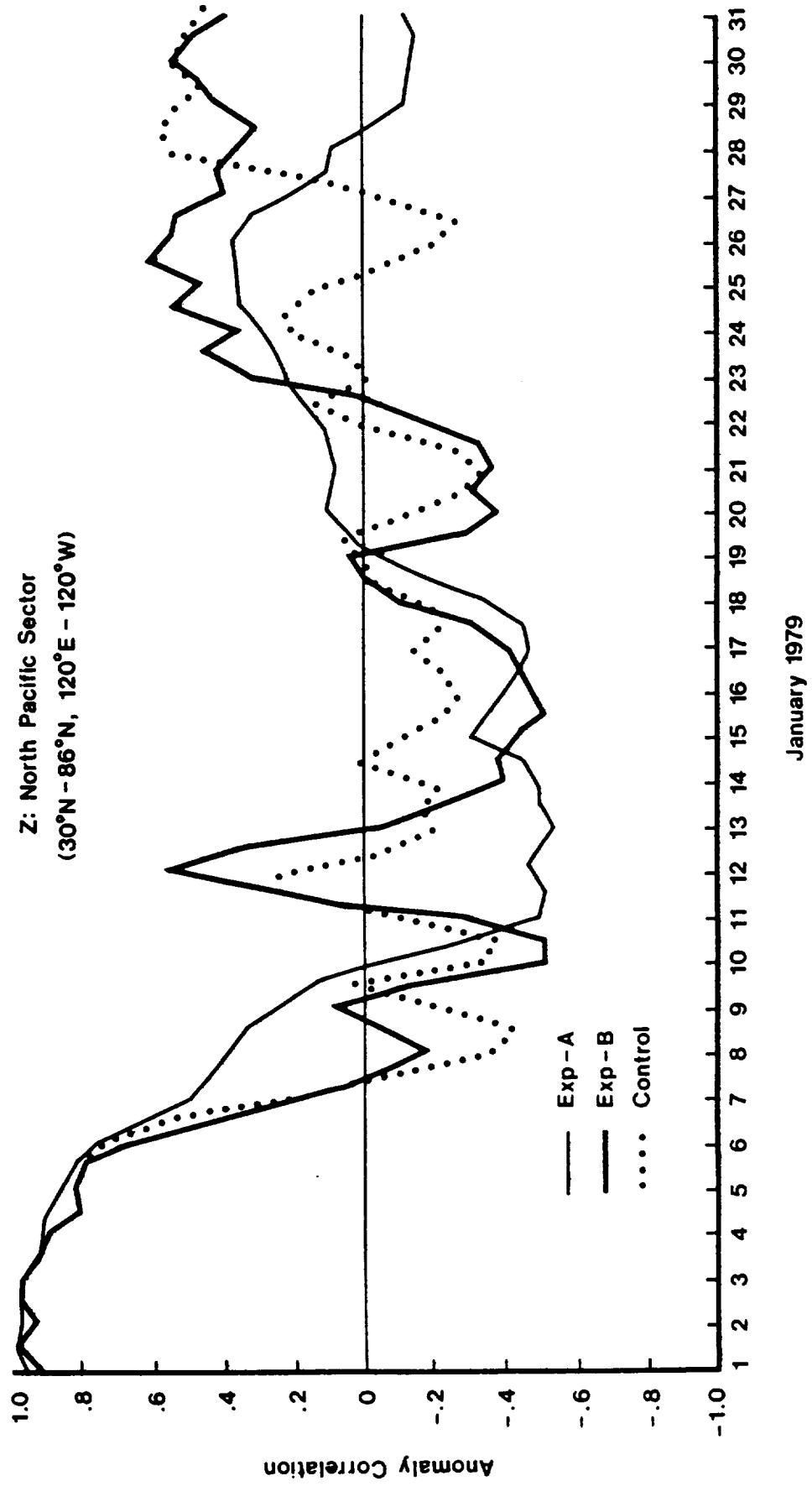


Figure 9



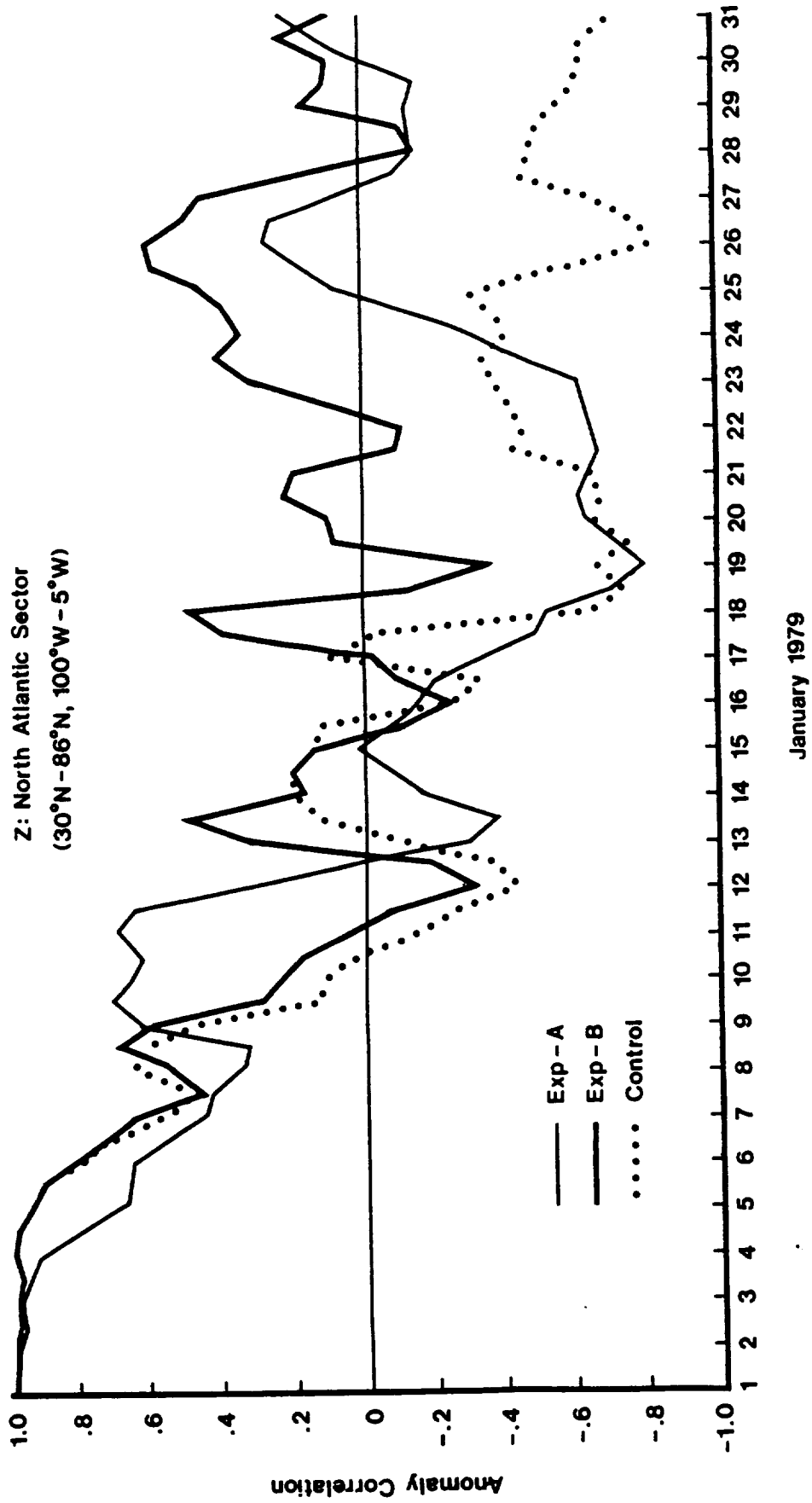


Figure 10

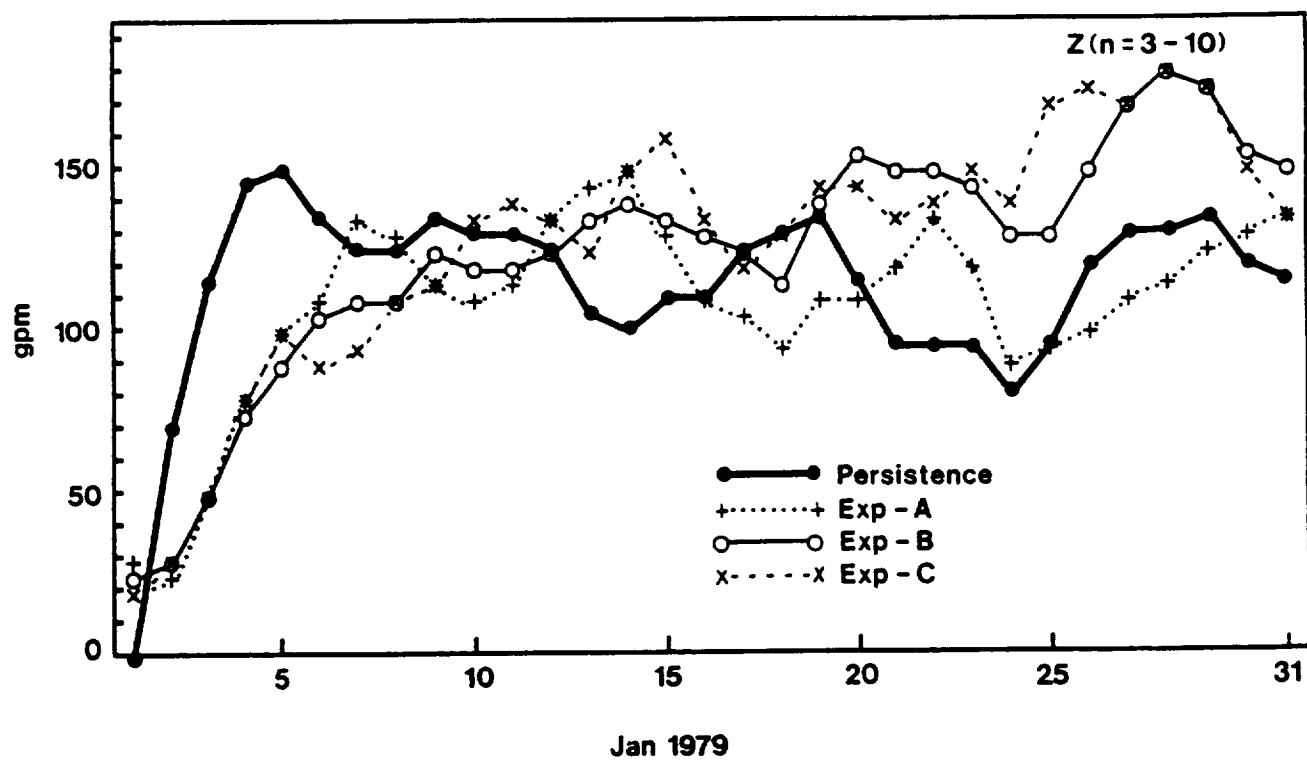
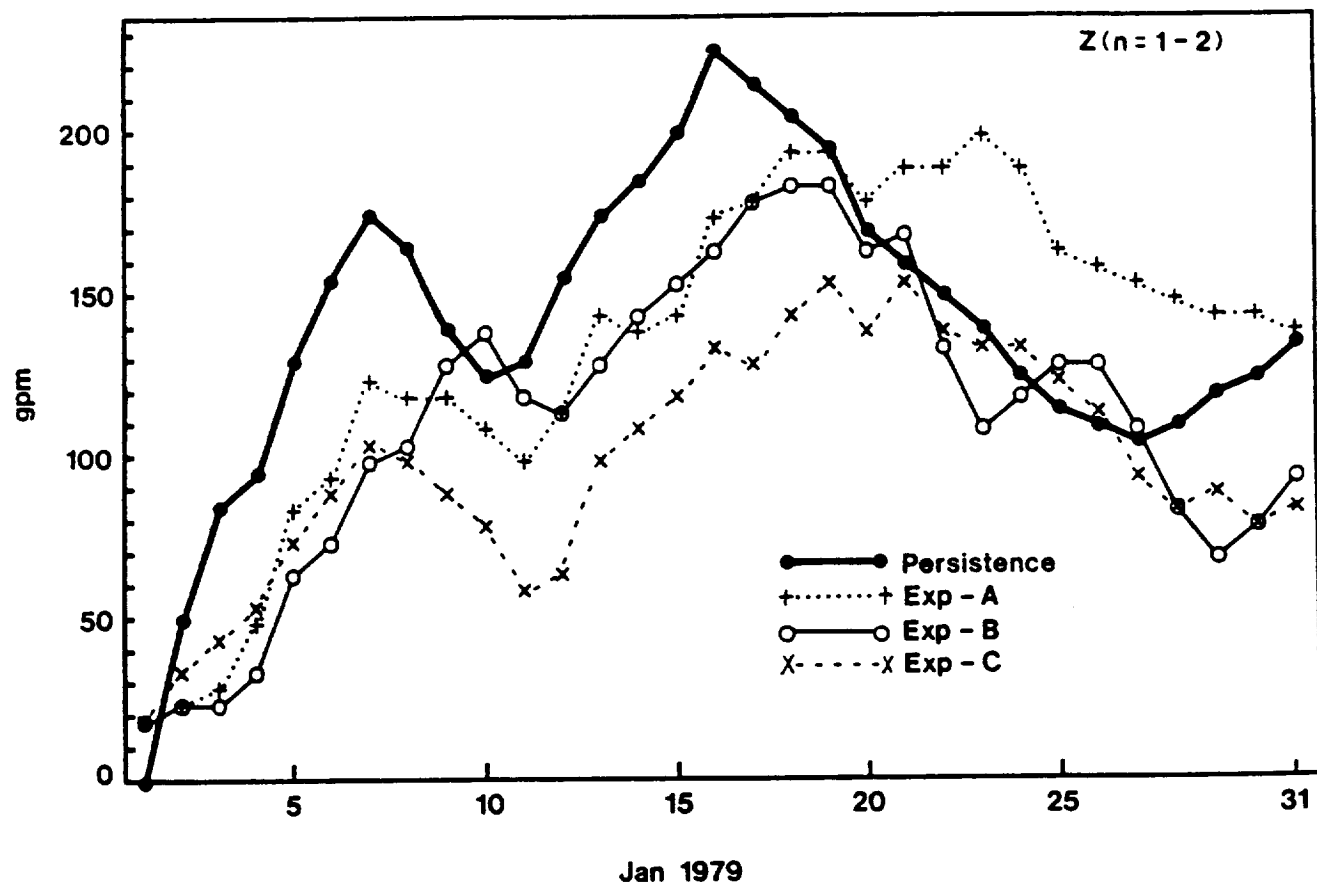


Figure 11

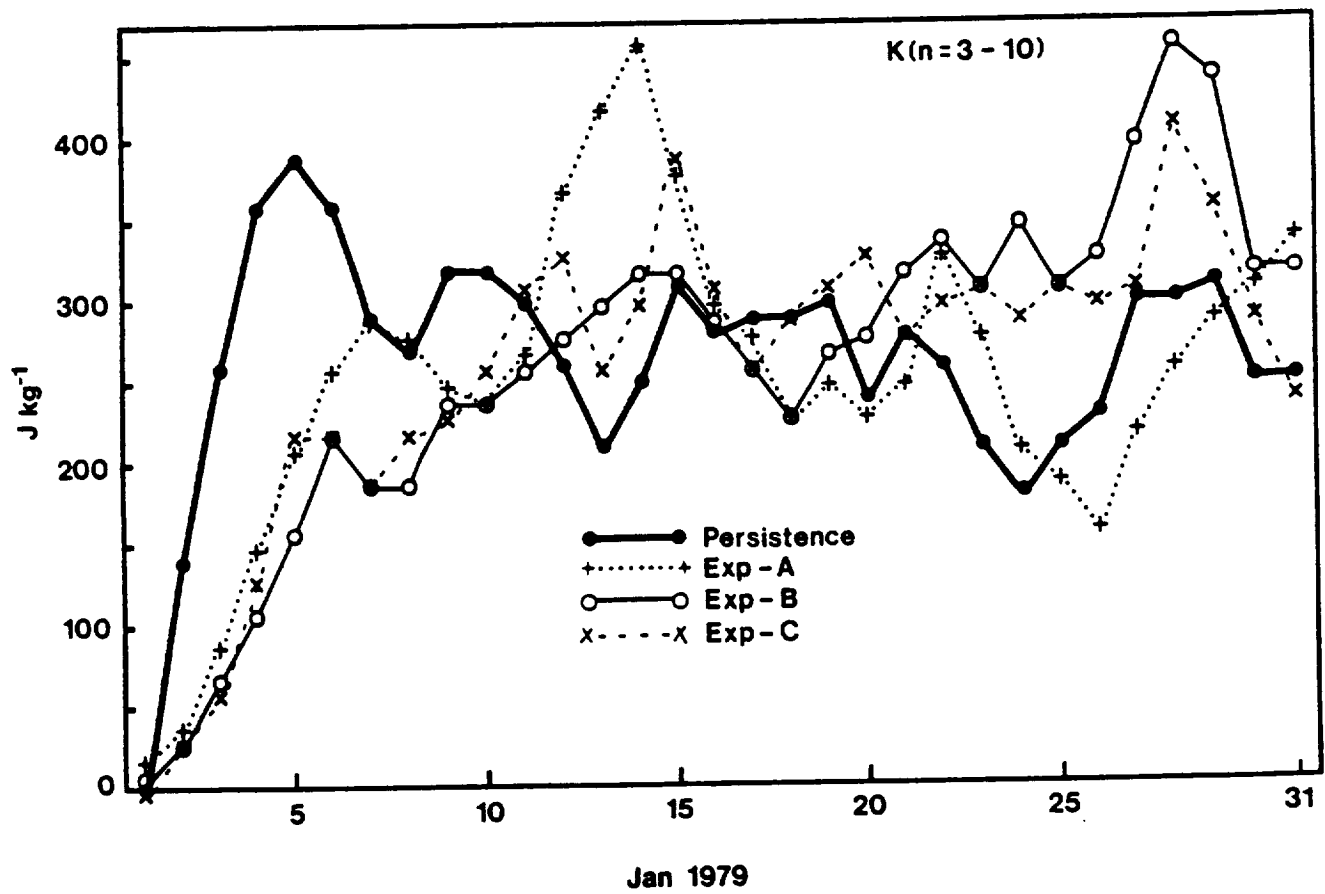
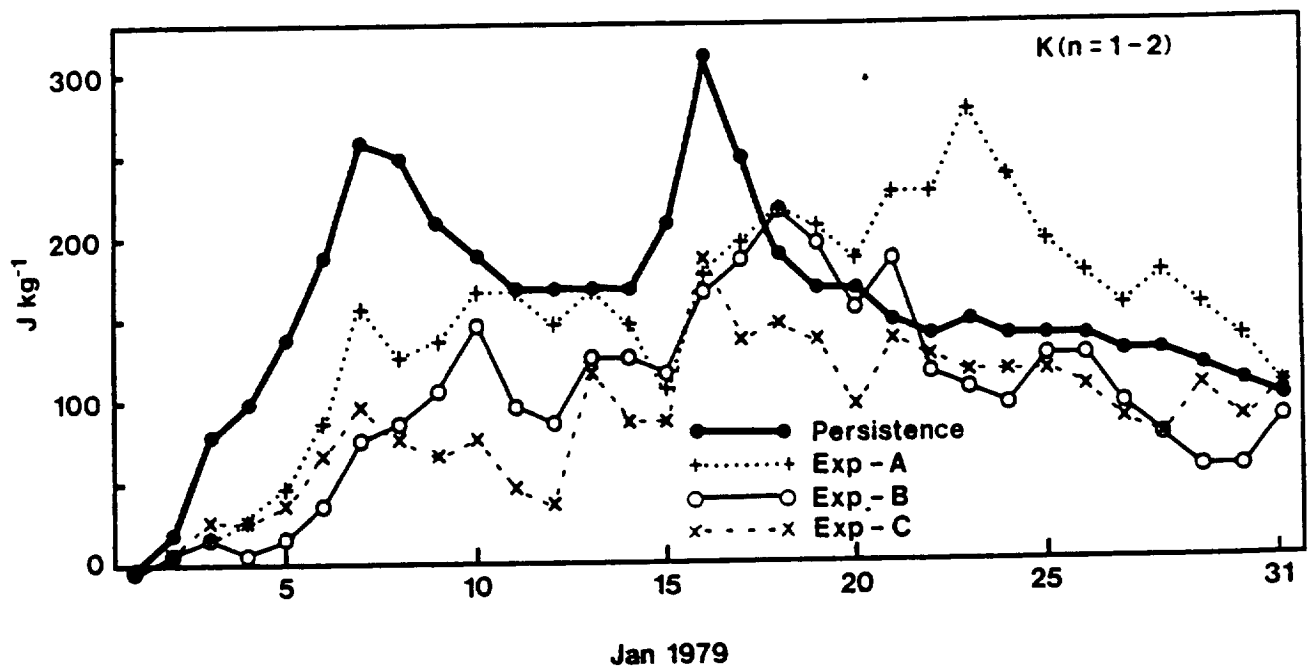


Figure 12

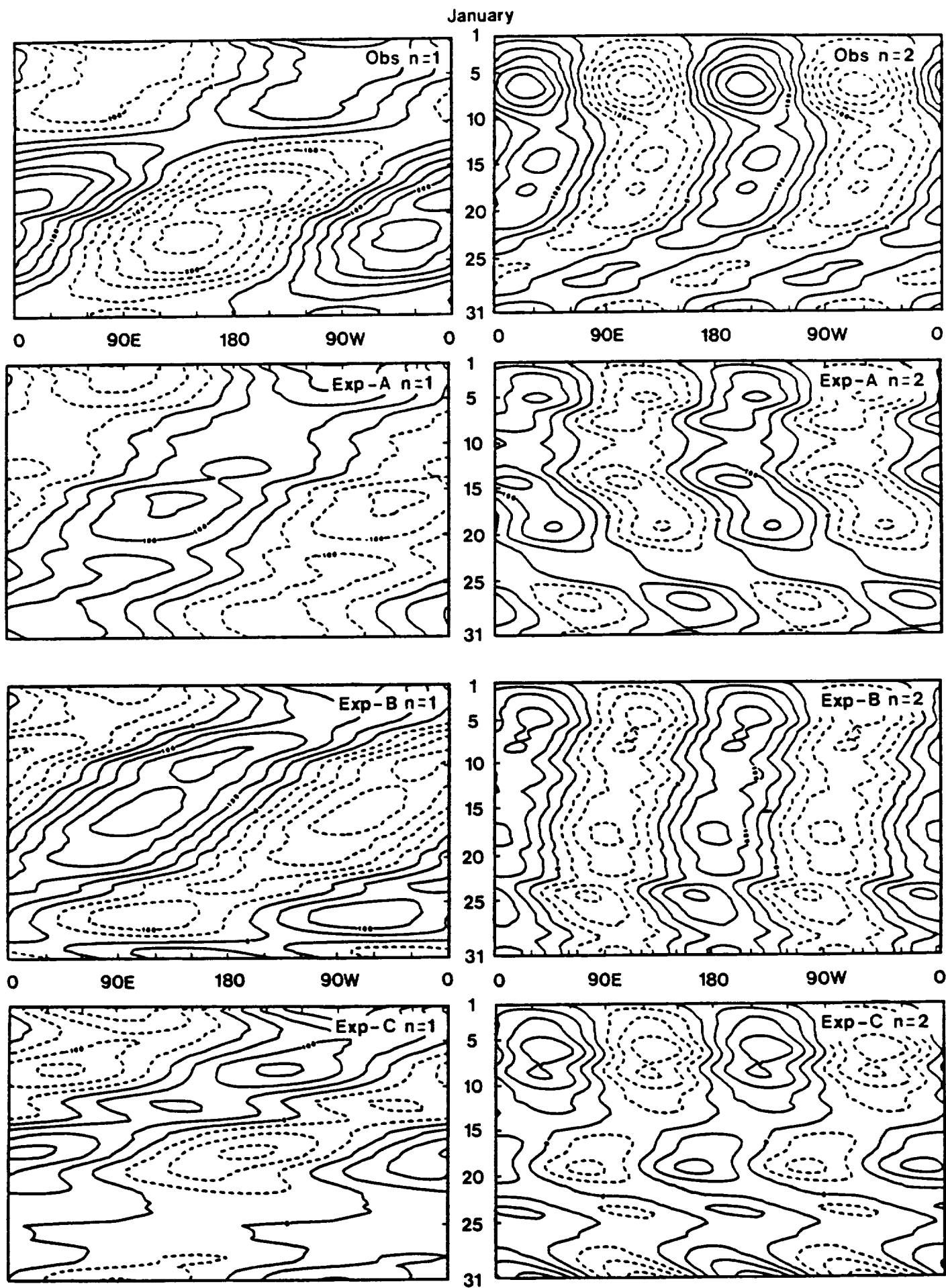


Figure 13



